The Evolution of Subhalo Orbits in Galaxy Clusters

by

Jedri de Luna

A thesis
presented to the University of Waterloo
in fulfillment of the
thesis requirement for the degree of
Masters of Science
in
Physics

Waterloo, Ontario, Canada, 2023

Author's Declaration

I hereby declare that I am the sole author of this thesis. This is a true copy of the thesis, including any required final revisions, as accepted by my examiners.

I understand that my thesis may be made electronically available to the public.

Abstract

Galaxies and their dark matter structures are commonly found within larger-scale structures called galaxy clusters. These clusters exhibit unique conditions to their constituent galaxies, as they have an elevated density compared to the background Universe. Cluster galaxy motion and evolution are tied very heavily to the properties of the cluster. This is seen observationally through the large fraction of galaxies no longer forming stars found within clusters. The dark matter structures galaxies reside in are also expected to undergo stripping and deformation as they move through the highly dense cluster environment. Models for the cessation of star formation in galaxies and galaxy survival times often use the pericenter as a benchmark for the timing of these processes. Also, galaxy orbits are used to probe the properties of the cluster itself. However, to model this accurately, the exact orbit of these galaxies must be well understood, as the density of the host system does not exactly follow the commonly assumed density profiles. The matter distribution of the hosts is often triaxial and is frequently changed through mergers with other systems. Mergers with other similarly sized clusters are especially likely to change the matter distribution of the host system violently. This should change the orbital path of constituent galaxies and thus change the predictions for galaxy quenching and evolution.

In this work, I aim to probe the validity of a semi-analytical model for the evolution of orbits using only the basic properties of the host system. This is done using dark-matter-only, high-resolution simulations. First, I examine the relationship between the orbital properties at the time of merging to properties of the host system. It is found that the distribution of infall parameters is only reasonably independent of mass ratio and that there is clear evidence that the host's state can significantly influence infall parameters. I then show that predictions about the pericentric passage (radius and timing) using infall orbital parameters are within 25% of their predicted values. However, it is found that many orbits are kicked away from their predicted orbit, often up to 70% of the orbits that merge at a given time. Also, orbits are often pushed deeper into the host, taking longer to reach the pericenter than predicted. Lastly, I attempt to model the evolution of surviving orbits using the host system's mass assembly history (MAH). It is found that this is not

feasible, as the effects of major mergers require more information to model correctly. Thus, a detailed model for the evolution of orbital properties requires more information than the general properties of the host.

Acknowledgements

I would like to thank my advisor, James Taylor, for his advice and patience throughout my degree.

Table of Contents

List of Figures

Chapter 1

Introduction

1.1 Motivation

Galaxies are important astronomical objects that harbor many unique and complex processes, such as stars' birth, life, and death. The population of stars within a galaxy and the rate at which they form, known as the star formation rate, are vital probes into the conditions of the Universe at a given time and location (Madau & Dickinson 2014a). However, we need a complete and detailed understanding of how these processes operate on a galactic scale. The current understanding of the evolution of galaxies starts with high-dense regions in the early Universe. As these regions evolve, they grow in mass partly by smoothly accreting matter. A key component of this accreted matter is gas, which can cool and clump together into high-dense regions within the galaxy. Regions with sufficiently high pressure and temperature can then form stars. Thus, the rate at which stars are formed is tied to the availability of gas and the prevailing physical conditions of the galaxy and universe (Madau & Dickinson 2014b). Similarly, the life cycles of stars, especially supernova explosions, contribute to the enrichment of the interstellar medium (Woosley & Weaver 1995) and can introduce enough energy into the galaxy to stop star formation (see Somerville et al. (2008)), further influencing the formation of new stars.

The total mass of stars within a galaxy is thus the cumulative effect of the birth and death of stars across the history of a galaxy. Examining the distribution of the stellar mass across a population of galaxies can provide insight into the relevant processes contributing to the population of stars in the broader context of the Universe. Galaxies will also interact with their environment through mergers with other galaxies and with the density of their surroundings. This can drastically change their morphology, eject material (including stars), and change the dynamics relevant to the evolution of their inner regions (Lotz et al. 2008; Kauffmann et al. 2004). Thus, studying the processes relevant within a galaxy can also describe the conditions of the Universe as a whole.

It is common to test various models of galaxy evolution by simulating a population of galaxies using said model and then comparing the output of these simulations to astronomical observations. However, the star formation within galaxies is in an interesting position in that it has a significant effect on the population of stars found within a galaxy but is sensitive to small-scale events, such as supernovae or feedback from supermassive black holes (Lacey et al. 2016). This means direct simulations of star formation through gas dynamics on scales relevant to cosmology are unfeasible, as the resolution required necessitates a large amount of computational power unavailable to researchers. Semi-analytical models (SAMs) can be used to address this. SAMs use dark-matter-only simulations, which do not directly include the complex processes predicted to be relevant to star formation and only directly simulate the motion of particles under the influence of gravity. Instead, these models use mathematical descriptions to attribute star formation to the distribution of matter, removing the need to model the dynamics relevant to star formation directly. Models of these kinds are beneficial because they reduce the computational power required and allow researchers to simulate populations of galaxies quickly.

1.1.1 Quenching and Galactic Orbits

An essential aspect of these models is the ability to generate the observed bimodality in the galaxy population, such as the bimodality in galaxy color. This bimodality has profound implications on the mechanisms at play when dealing with the star formation rate in galaxies and its subsequent cessation. Observationally, there is a separation between red and blue galaxies. Figure 1.1 shows the two distinct populations of galaxies at different colors. Since galaxies include a collection of stars gravitationally bound together, their color indicates the population of stars present within the galaxy. Stars can be cataloged in a Hertzsprung-Russell (HR) diagram, indicating the relationship between the luminosity and temperature of a star. The high-temperature surface of stars emits blackbody radiation. The equation for the spectral radiance at a given frequency and temperature, $B(f, T)$, emitted by a blackbody is:

$$B_f(f, T) = \frac{2hf^3}{c^2} \frac{1}{e^{\frac{hf}{kT}} - 1} \tag{1.1}$$

where h, f, T, c, and k are the Plank constant, frequency of light emitted, object temperature, speed of light, and the Boltzmann constant, respectively. At higher temperatures, equation 1.1 peaks at a high frequency, and thus the star will be bluer in color.

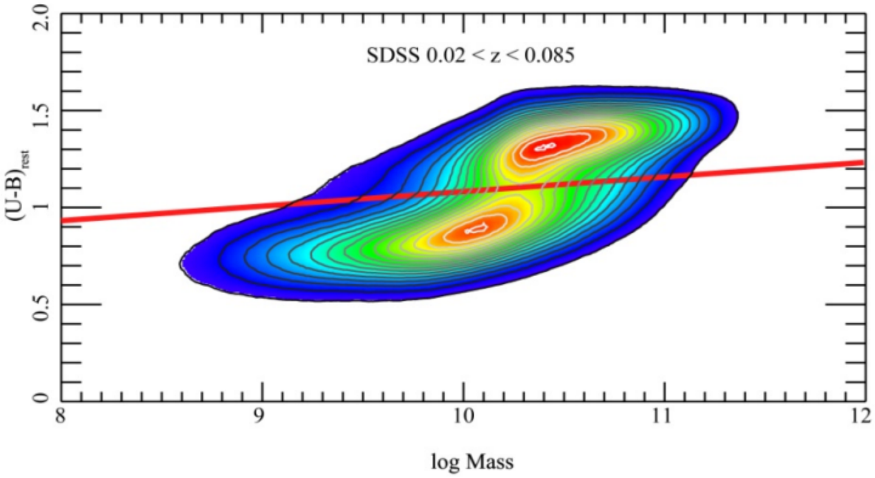

Figure 1.1: Bimodality of galaxy colour from Peng et al. (2010). This plot is generated from a collection of galaxies from the Sloan Digital Sky Survey (Abazajian et al. 2009), of low redshift galaxies. The vertical axis shows the difference in magnitude of the galaxies in two different colors in the rest frame of the galaxy. A higher U-B value indicates a red color. The horizontal axis shows the stellar mass of the galaxy. There are two clear peaks in the distribution of color, highlighting the color bimodality.

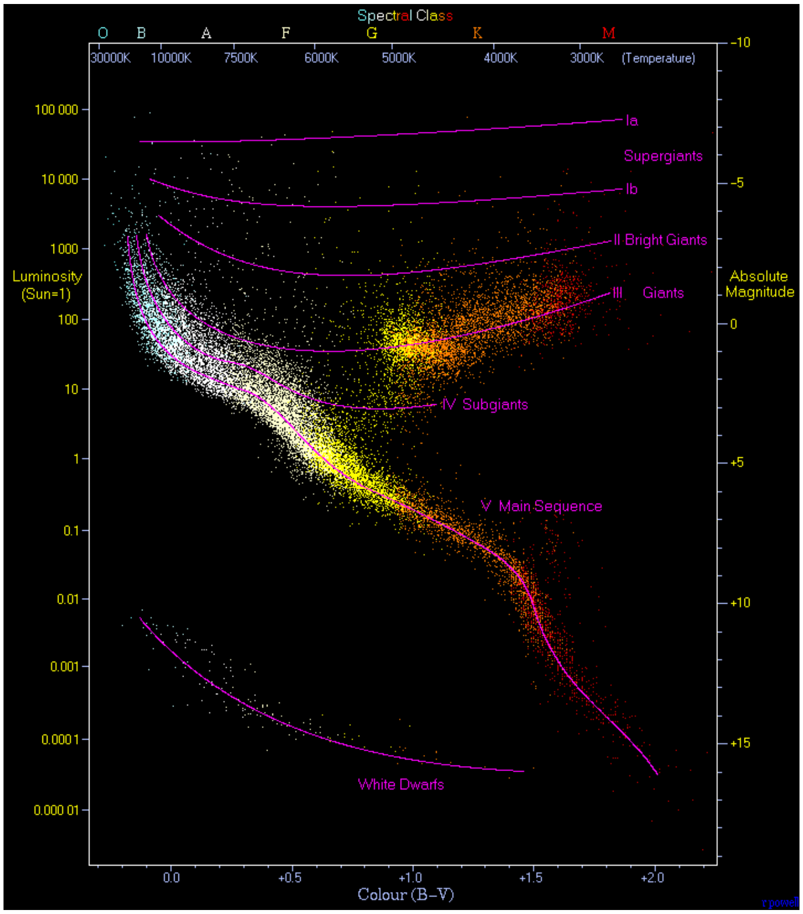

Figure 1.2: HR diagram from Powell (2006), generated from a collection of 22000 stars from the Hipparcos Catalogue and 1000 low-luminosity stars from the Gliese Catalogue of Nearby Stars. Plotted on the y-axis is the luminosity and, equivalently, the absolute magnitude of stars. The x-axis shows the color and equivalently temperature. The color of each data point also indicates the color of the star. Labeled in purple are different populations of stars. Notice that the main sequence of stars extends from the upper left to the bottom right, indicating that blue main sequence stars are significantly brighter than red ones. There is also a population of giants and supergiants in the upper right-hand of the plot. These non-main-sequence stars are very luminous and red. Main sequence stars can transition to this population in the late stages of their life cycle.

Stars start their life cycle in a population known as the main sequence. When plotted in an HR diagram, main sequence stars populate a region indicating bluer stars have a higher luminosity, shown in Figure 1.2. Thus, if the population of main sequence stars is maintained, a galaxy will appear blue. However, as these stars age, they will often evolve into different phases of their life or die. Blue stars are hotter than red ones and thus expend their fuel quickly, giving them a shorter lifetime than redder stars. Thus, as a population of stars ages without new stars forming to fill in the missing main sequence stars, the population will tend to have more red stars. Similarly, as stars leave the main sequence, they enter a phase indicative of a high luminosity and red color, known as red giants. These are shown as the population in the giants and supergiants region, shown in the upper right portion in Figure 1.2. All of this leads to the understanding that an aging population of stars in a galaxy without active star formation will be redder than a younger population.

The availability of cold gas drives the level of star formation within a galaxy. As this gas clumps together, the density and pressure within are enough to ignite the gas in thermonuclear reactions, giving birth to a star. Thus, as long as a galaxy has a reserve of regions of sufficiently dense cold gas to support star formation, new stars will continue to be born, giving rise to a continually replenished population of main-sequence stars. This causes the galaxy to appear blue. Once star formation stops, known as the quenching of the galaxy, the population of blue stars quickly diminishes, and the galaxy appears red. Because of the clear bimodality of galaxy color, there is a very small population of transient galaxies between these two populations, indicating that the quenching mechanism occurs quickly on a cosmic timescale.

In a study conducted by Peng et al. (2010), galaxy mass and environment are shown to separately describe this quenching by examining a collection of galaxies found in the seventh release of the Sloan Digital Sky Survey (SDSS) (Abazajian et al. 2009). Figure 1.3 shows galaxy mass on the horizontal axis and the density of the environment on the vertical axis. The color indicates the fraction of red, non-star-forming galaxies in a particular bin. There is a clear trend for higher-density regions to have a higher fraction of quenched galaxies at fixed low stellar mass. Similarly, the red fraction increases with stellar mass at a fixed low density. They argue that this indicates two general categories of quenching mechanisms: environmental and mass quenching. Mass quenching has been linked to internal processes of the galaxy, such as interactions with their active galactic nuclei (AGN) or black holes (see Somerville et al. (2008) for their SAM incorporating these effects). Environmental quenching is quenching caused by interactions with a galaxy's environment, such as ram-pressure stripping (Lotz et al. 2019). This separation is justified since the red fraction increases solely with overdensity at low stellar mass, where we expect little mass quenching. Similarly, the red fraction increases with stellar mass in regions of low density.

The nature of environmental quenching is also related to another key bimodality of galaxies: central and satellite galaxies. Central galaxies are formed at the center of a high-density region known as a dark matter halo. Since central galaxies are at the center of these regions, they accumulate matter as other galaxies and matter fall to the region's center. On the other hand, satellite galaxies form in the outskirts of these halos and often fall inward toward a central galaxy. This means satellite galaxies are lower mass than centrals and are more susceptible to environmental quenching. Similarly, central galaxies will accumulate more mass; mass quenching mechanisms will be the main factor stopping star formation in a central galaxy. Generally, galaxies start as centrals and then transition to satellites as they fall into the region around a larger central galaxy.

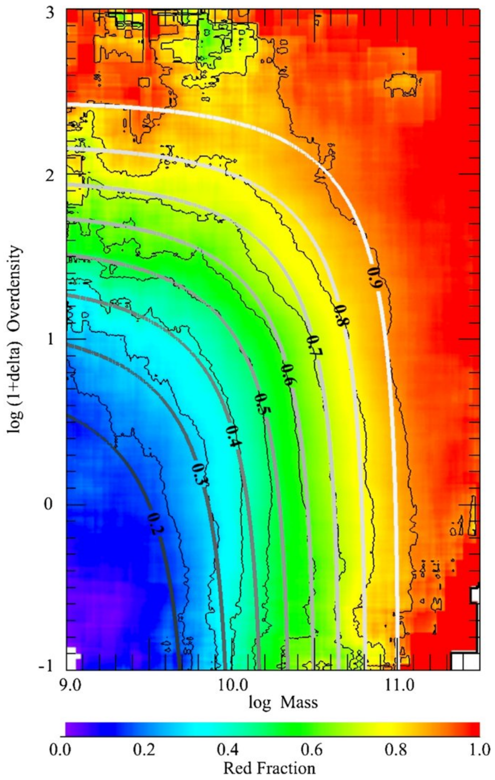

Figure 1.3: From Peng et al. (2012), this plot shows that the quenched fraction of galaxies is separable into mass and environmental quenching. There is a clear increase in the quenched fraction at high overdensity or galaxy stellar mass. This plot was generated using 238 474 galaxies in a redshift range of $0.02 < z < 0.085$ from SDSS data.

The exact mechanism that governs environmental quenching is an active area of research. It is generally attributed to a galaxy's gas reservoirs being stripped away through interactions with its high-dense surroundings. Ram-pressure stripping is the effect that occurs as a satellite galaxy moves through the highly dense environment on infall toward the nearby central galaxy. As satellite galaxies quickly move through their dense environment during their infall, their reservoirs of cold gas are stripped away. Tidal stripping, on the other hand, occurs due to the tidal field present within the high-density environment. As the galaxy falls toward the center of the matter distribution, the difference between the forces on its different sides is large enough to cause a portion of its gas, stars, and dark matter to be stripped away from the galaxy.

It is also known that the orbital path of subhalos has a strong effect on their subsequent evolution. Smith et al. (2022) find that pericentric location, and thus the tidal stripping, is heavily dependant on the tangential velocity at infall. This supports the view that structure outside the confines of the host system, which is responsible for the tangential component of velocity, plays a key role in the evolution of subhalos. van den Bosch (2017) find that tidal forces for ejected subhalos are large enough to modify orbits. Again, these objects' type of orbital path plays a crucial role in their evolution. Similarly, Ogiya et al. (2022) find that pericentric radii very close to the cluster can result in 98% loss in subhalo mass. van den Bosch et al. (2018) also shows that tidal effects from the host are the dominant factor in mass loss for subhalos. Thus, even without directly tracking halo orbits, infall parameters, particularly those that predict pericentre, can predict the future lifetime of subhalos and galaxies.

The motion of satellite galaxies as they fall to the center of their cluster is an important aspect of galaxy quenching models. Specifically, when and where the pericenter occurs can help quantify the level of quenching without the need for direct simulation of gas dynamics. A model for the environmental quenching of galaxies within clusters would ideally populate the cluster with orbits and predict quenching from these values. For simplicity, this cluster should be defined by its growth in mass, known as its mass assembly history (MAH). This SAM would remove the need to model the cluster other than a set of mass values in time. The model would introduce orbits with a distribution of infall parameters, as discussed in section 2.2, and use these to predict when and where the pericenter occurs. The first goal of this project is to determine if such a model is feasible. Can the infall parameters accurately predict when and where the pericenter will occur? Are the infall parameters themselves well described? The latter is addressed in section 2.2, while I address the former in 2.3.

1.1.2 Distribution of Galaxy Orbits

The distribution of orbits is also very relevant to modern astronomical studies. These orbits act as a tracer of the underlying distribution of dark matter and thus provide insight into its nature. Historically, this has been a large contribution to the discovery of dark matter, as the orbital motion of galaxies did not match the distribution of baryonic matter (). More recently, this has been used to determine the mass of galaxy clusters and other large-scale structures (Abdullah et al. 2018). This is very relevant for cosmology, as it tests the number density of high-mass objects.

One technique used to probe the matter distribution of disk galaxies is through rotation curves. The rotational velocity of an object, ν_r, scales with the radial distance away from the host center, R, and the mass enclosed, M(R).

$$\nu_r \propto \sqrt{\frac{M(R)}{R}} \tag{1.2}$$

Thus, the mass profile of a cluster can be inferred through measurements of the rotational velocities of member objects. Figure 1.4 shows an example of this for the galaxy NGC3198. The flat curve indicates $\sqrt{M(R)/R}$ remains constant at large radii, indicating the mass enclosed increases with radius. However, the direct measurements of the mass of the detectable matter at these regions show a clear drop in the density at higher radii. This suggests a distribution of undetectable matter at the system's outer edges, later called dark matter.

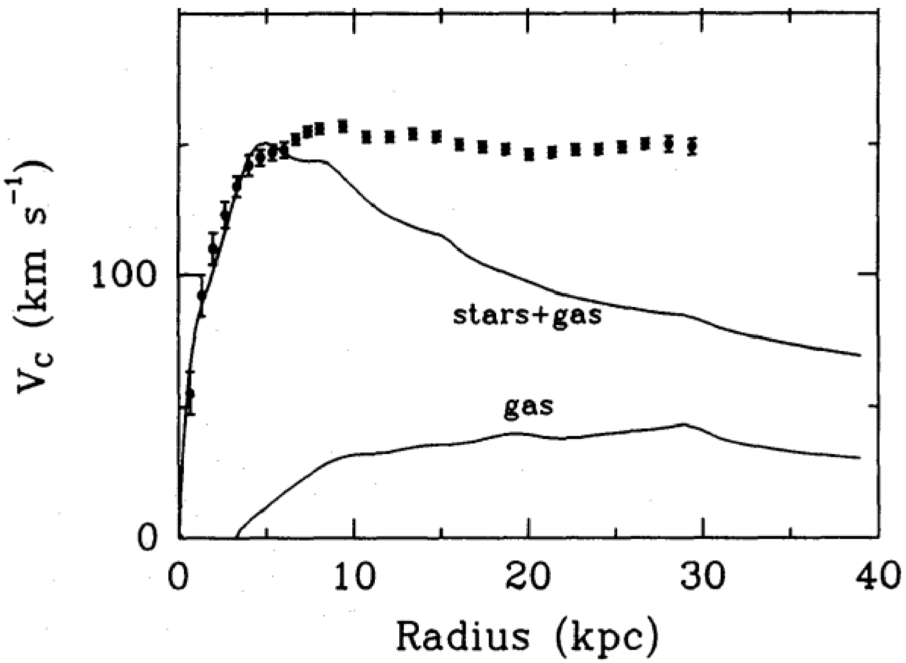

Figure 1.4: Taken from Begeman (1989), the rotational velocities for NGC3198 at various radii is shown. The points are the rotational velocities from measurements of HI regions. The solid lines show the predicted rotational curve from stars and gas and gas alone. The flat curve at increasing radii suggests an extended distribution of matter is present. This matter does not consist of stars or gas and is attributed to dark matter.

Similarly, the Caustic technique uses the distribution of galaxies to estimate cluster masses (Diaferio & Geller 1997; Diaferio 1999). This technique relies on the observation that there is a clear separation between the line of sight velocity of galaxies that are members of a cluster and those that are not. This comes from member objects having left the Hubble flow and are infalling to the halo. From the amplitude, A, of allowed velocities, the mass profile can be estimated with the following relation:

$$M(<r) \propto \int_0^r A^2(R)dR \tag{1.3}$$

An example of this technique from Pizzardo et al. (2023) is shown in Figure 1.5. The blue curve indicates the amplitude of the distribution of velocities.

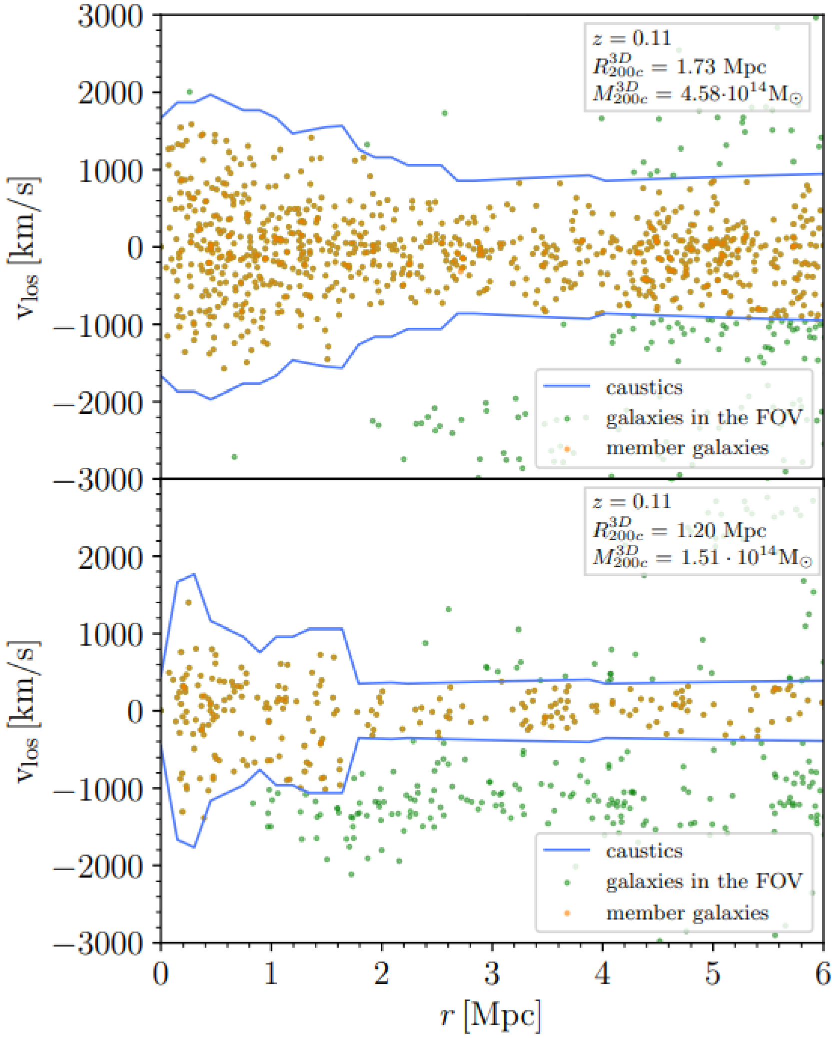

Figure 1.5: Demonstration of the caustic technique, from Pizzardo et al. (2023) The points in yellow represent member galaxies of a host halo. The blue curve shows the system's amplitude, or caustic, at a given projected radius. The trumpet shape shows a clear difference between the inner and outer portions of the host halo. These are simulated results so that galaxy membership can be directly determined.

Lastly, the orbital properties of member galaxies can provide insight into the history of the host system. As the host builds up mass and increases in radii, the allowed velocities and radii of member galaxies increase. This can lead to a stratification of orbits, where recently merged objects lie closer to the host edge, while long-lasting orbits lie closer to the center.

These indicate that the orbital properties of galaxies can be used as probes of their cluster. However, these orbits change throughout the evolution of the host. The cluster itself is a dynamic and complex distribution of matter and can interact with other large objects, which can cause the motion of subhalos to change. Similarly, galaxies themselves can interact with each other. The second goal of this project is to see if these effects are required to model the evolution of orbits within galaxy clusters properly. Ideally, this model would use only the cluster's MAH to introduce and heat the distribution of orbits. In Section 2.4, I discuss the evolution of orbital properties throughout an object's orbit and test the feasibility of modeling its evolution.

1.2 Halos

1.2.1 Halo Origin and Evolution

In the currently accepted cosmological model, ΛCDM, the energy content of the Universe consists of two main components: Λ, which describes the acceleration of the expansion of the Universe, and cold dark matter (CDM), describing the main component of matter which only acts gravitationally. Within the expanding Universe, gravity causes matter to clump together (Alves et al. 2020). The overall expansion of the Universe is called the Hubble flow. This picture of the Universe separates matter into two categories: baryonic matter and dark matter. Baryonic matter refers to ordinary matter, such as that which makes up planets, stars, and galaxies. Dark matter is the distribution of matter that only acts gravitationally. The total matter distribution of the Universe is dominated by dark matter, which accounts for nearly 80% of the matter distribution. On the scales relevant to galaxies and galaxy clusters, gravity is the dominant force dictating their evolution over long periods. Thus, the distribution of dark matter is the main consideration for structure evolution.

Note that due to the initial hot, dense conditions of the early Universe, its components continue to expand away from each other as the Universe evolves. The expansion rate is accelerating at later times, driven by dark energy. This explains the observed effect that objects appear to be moving further away from each other with time. This can be described by the Universe's scale factor, a, at a given time. This scale factor is set to 1 at present and decreases at earlier epochs of the Universe. For example, if the scale factor at a particular time is 0.5, by the time the Universe evolves to the present day, distances between objects - assuming they are not moving with respect to the overall expansion - will increase by a factor of 2.

The scale factor is often instead described by a redshift, as it is easier to measure observationally. Redshift (z) refers to the relative change in the wavelength of light due to this effect.

$$z = \frac{\lambda_{\text{obsv}} - \lambda_{\text{emit}}}{\lambda_{\text{emit}}} \tag{1.4}$$

$$a = \frac{1}{1+z} \tag{1.5}$$

At present, z=0, which increases at earlier epochs of the Universe. Redshift is used as a cosmic clock, where the redshift is related to the cosmological epoch. It is common to transform distances between objects into comoving units to remove the varying distances between objects due to this expansion.

$$\vec{r}_{\text{comoving}} = \frac{\vec{r}_{\text{physical}}}{a} \tag{1.6}$$

Understanding how to identify and classify large structures in the Universe is also essential. Gravitationally bound structures in the Universe reside within regions with a density high enough to prevent bound objects from expanding with the Universe, causing them to fall inward eventually. These regions are called halos and are described by their elevated density compared to the average density of the Universe:

$$\delta(\vec{r}) = \frac{\rho(\vec{r}) - \bar{\rho}}{\bar{\rho}} \tag{1.7}$$

where $\rho(\vec{r})$ is the density of the halo at a position $\vec{r}$, and $\bar{\rho}$ is the average density of the Universe. Typically, a halo is defined as a region such that its over-density is 200 times the critical density of the Universe.

Galaxy clusters indicate a halo large enough and high enough in density to have many galaxies gravitationally bound to it. These galaxy clusters are the largest bound structures observed in the Universe, containing up to thousands of galaxies and reaching ∼1 Mpc in size. To keep that in perspective, the Milky Way has a radius of about 290 kpc (Deason et al. 2020). These galaxy clusters are of particular interest, as they have a considerable influence on the evolution of their galaxies (Kauffmann et al. 2004, 2003; Baldry et al. 2006).

The spherical collapse model aims to describe the evolution of halos, starting from the early Universe. It is an idealized model that starts with the density field in the early Universe. Observations of the cosmic microwave background (CMB) have shown that the early Universe is described by an almost entirely homogeneous and isotropic density field of matter (Planck Collaboration et al. 2016). In spherical collapse, the assumption is that within this density field, there are spherical regions that are higher density than the average density of the Universe, $\bar{\rho}$. As noted above, the matter component is dominated by dark matter, meaning this generally refers to a region with a high density of dark matter. These overdense regions are described by their relative overdensity with respect to the background Universe, using equation 1.7. Starting from the initial seed, overdense regions in the early Universe, the overall gravitational field is expected to be pointed inward, causing the region to collapse. As the system evolves, this effect and matter in surrounding regions falling inward toward the halo increases the region's density.

The slow collapse of these regions leads to an essential aspect of spherical collapse: the idea that overdense regions will gradually increase in overdensity and eventually cause surrounding objects to leave the Hubble flow and fall back inwards. A result of this definition is that it gives a logical boundary of the halo. To define a bound structure, we can use the virial equation, which describes the global properties of a gravitationally bound system. For an isolated system, this equation is:

$$2 < K > + < U > = -\frac{1}{2}\frac{d^2 I}{dt^2}$$

where $< K >$ and $< U >$ are the average kinetic and potential energy of the system respectively. The right-hand side describes the second derivative of the momentum of inertia, I. This is very small for slowly changing systems, as is assumed for halos. Thus it is common for this equation to be written as:

$$2 < K > + < U > = 0$$

We can thus say that if objects on average follow this relation, they are bound to the halo and are part of the system.

In spherical collapse, shells of matter initially expand away from an overdense region. They eventually reach a maximum radius away and fall back inward toward the halo. This radius is called the turnaround radius. At this point, the shell will be still, and thus $< K >= 0$. The shell will satisfy the virial equation at half this radius and be considered part of the host halo. This location is called the virial radius, $R_{\rm vir}$ with the mass interior to it called the virial mass, $M_{\rm vir}$.

There are two regimes in the evolution of halos: the linear and non-linear. The linear regime occurs when $\delta < 1$, thus early in the evolution of a halo. The overdensity scales linearly at this point, as linear perturbation theory describes. Once the density becomes of order unity, linear perturbation theory no longer accurately describes the evolution of the overdensity. The structure then collapses into a self-bound structure, where complex interactions between the distribution of matter become relevant. N-body simulations are required to study and fully understand halos in the non-linear regime.

Hierarchical structure formation is also an important aspect of the evolution of halos (White & Rees 1978; Davis et al. 1985). This idea states that halos' evolution is dominated not only by the slow growth from spherical collapse but also by interactions with other halos. A schematic of this process is shown in figure 1.6, showing that large structures are formed through the complex combination of individual, smaller halos. These smaller halos can still exist as gravitationally bound objects and can exist within their host for an extended period. These substructures are known as subhalos. Cluster galaxies themselves exist within a subhalo in the host halo that is the cluster. This view of structure formation states that cluster galaxies, which exist within subhalos of the larger galaxy cluster, form separately in the outer regions of another larger halo and eventually merge with their host.

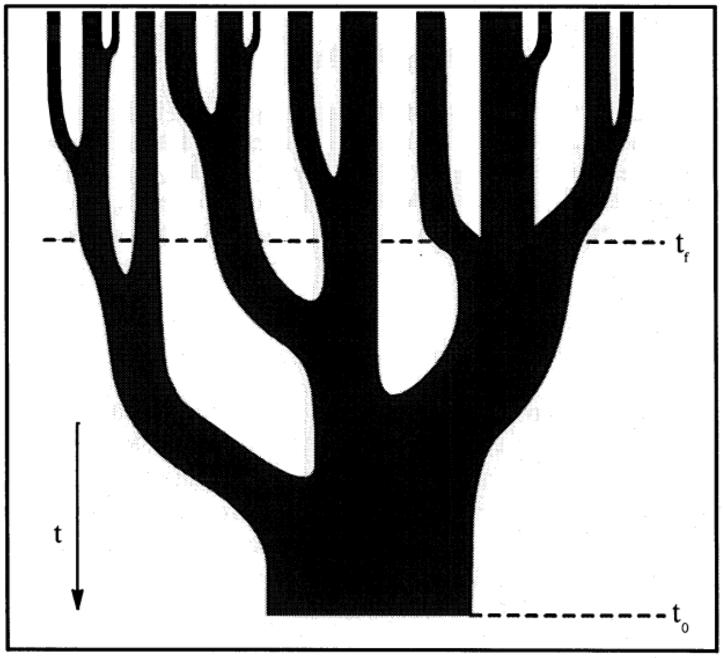

Figure 1.6: From Lacey & Cole (1993), indicating the evolution of a merger tree. Halos grow through mergers of smaller halos. Each branch indicates a different halo, with the width indicating its mass. At the bottom of the figure is the halo at the present day, indicated by t_0. t_f indicates a moment in the history of the halo. The merging branches indicate that the history of large structures at the present day are formed through smaller halos merging to form larger ones.

These ideas leave the following picture for halo evolution. According to linear perturbation theory, initial, spherical, overdense regions in the Universe collapse inward linearly. As the density of these regions increases to the regime of $\delta \sim 1$, the system enters a non-linear regime, where simulations are required to model the complex interactions relevant to the distribution of matter. Finally, neighboring halos can fall inward toward each other and merge. Major mergers between two similarly sized objects can cause large, sudden changes to the matter distribution. Minor mergers between a larger host halo and a smaller subhalo will instead introduce a substructure to the system. The latter is the origin of the collection of galaxies bound to galaxy clusters.

1.2.2 Properties of Halos

Numerous studies have examined the properties of these halos in the non-linear regime. The commonly used density profile used to describe halos is the NFW density profile (Navarro et al. 1997). Analyzing many cosmological simulations including hierarchical structure formation, has garnered the name of the universal density profile, as it was determined to be consistent across all scales, epochs, and cosmologies. The density profile and corresponding potential are as follows.

$$\rho_{\mathrm{NFW}}(r) = \frac{\rho_s}{r\left(1+\frac{r}{R_s}\right)^2} \tag{1.8}$$

$$\Phi_{\mathrm{NFW}}(r) = -\frac{4\pi G\rho_s R_s^3}{r}\ln\left(1+\frac{r}{Rs}\right) \tag{1.9}$$

where G is the gravitational constant, R_s is the scale radius, and ρ_s is the scale density of the halo. R_s is the radius where the slope of the density profile in the log scale has a sharp decrease. This is shown in Figure 1.7. ρ_s is the density such that the total mass, M, of the halo follows $M \propto \rho_s R_s^3$. Given a radius of the halo, R, we can also define the concentration parameter, c, such that:

$$c = \frac{R}{R_s} \tag{1.10}$$

The Einasto profile (Einasto 1965) is also often used, as it better matches the inner structure of a host's density. This profile uses the same parameters for the scale radius and scale density and introduces the free parameter α, which dictates the logarithmic inner slope of the density profile.

$$\rho_e(r) = \rho_s \exp\left(-\frac{2}{\alpha}\left[\left(\frac{r}{R_s}\right)^{\alpha} - 1\right]\right) \tag{1.11}$$

In this work, I will use the NFW density profile, but as this profile mainly differs on the innermost regions of the halo, it is expected that using this fit would remain the same. It is also not preferred as it requires an extra fitting term α.

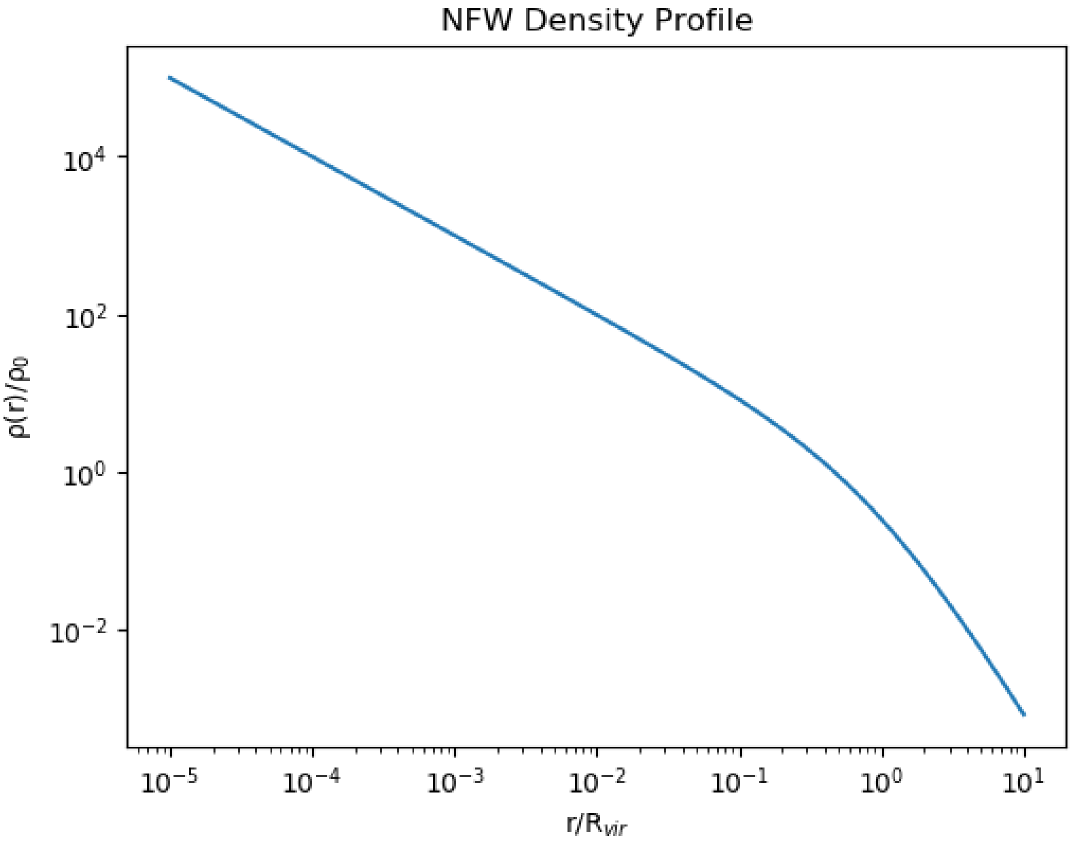

Figure 1.7: NFW Density Profile Navarro et al. (1997), showing the density plotted against the radius, scaled to R_{vir}. In this case, the concentration parameter is chosen to be 6. As noted by definition, there is a clear change in the slope at R_{vir}/c.

Another key property of halos is the rate at which they form and grow in the Universe. The halo mass function indicates the number density of halos of a given mass in the Universe at a given epoch (Press & Schechter 1974; Lacey & Cole 1993). The shape of this function relies heavily on the model of structure growth and the cosmology of the Universe. A Universe with expansion will actively prevent structure growth, decreasing the number density at all scales. Similarly, a Universe with a matter component or a different initial density field will change this distribution.

Following Press-Schechter formalism (Press & Schechter 1974), the number of objects, dN, between a mass M and $M + dM$ is modeled by the following.

$$dN = \sqrt{\frac{2}{\pi}} \frac{\bar{\rho}\delta_c}{M\sigma^2} \frac{d\sigma}{dM} \exp\left[-\frac{\delta_c^2}{2\sigma^2}\right] \tag{1.12}$$

Here, δ_c is the critical density of the Universe, σ is the standard deviation of the power spectrum of the early Universe, and $\bar{\rho}$ is the average matter density of the Universe. The key feature of the mass function is an exponential decay in the number of halos at high masses. The shape of this function is also expected to vary as the Universe evolves. At lower redshifts, the structure has had more time to accrete mass. This will cause the density of higher-mass halos to increase and the total number of halos to increase. Figure 1.8 shows this for two different cosmologies at differing redshifts.

The halo mass function can also be used to describe the bimodality between starforming and non-starforming galaxies. Galaxies themselves exist within a sufficiently large halo, so it is expected that the stellar mass function (SMF), which is the same as the HMF but for stellar mass, should follow a similar trend as the HMF. However, shown in Davidzon et al. (2017), there is an apparent drop-off in the SMF at high masses. Figure 1.9 shows an example of this. This supports the idea that mass quenching prevents high-mass galaxies from forming stars.

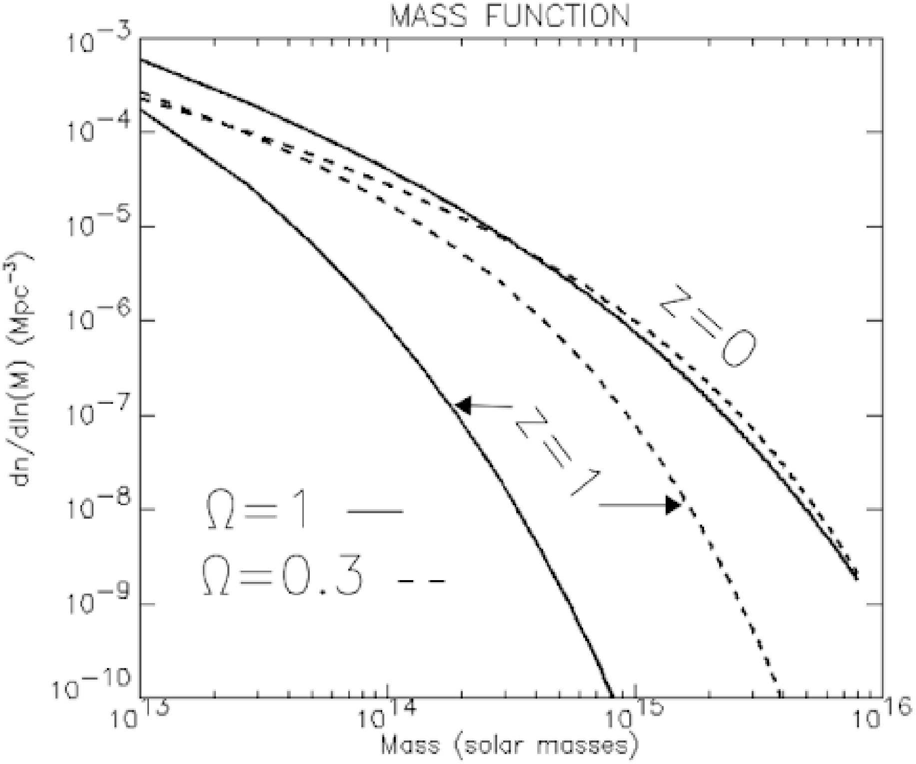

Figure 1.8: The Press-Schechter halo mass function at z=0 and z=1 for a matter only cosmology (solid) and $\Omega_m = 0.3$ (dashed), taken from Bartlett (1997). At lower redshifts, the number density of halos at all scales increases, and there are more high-mass halos.

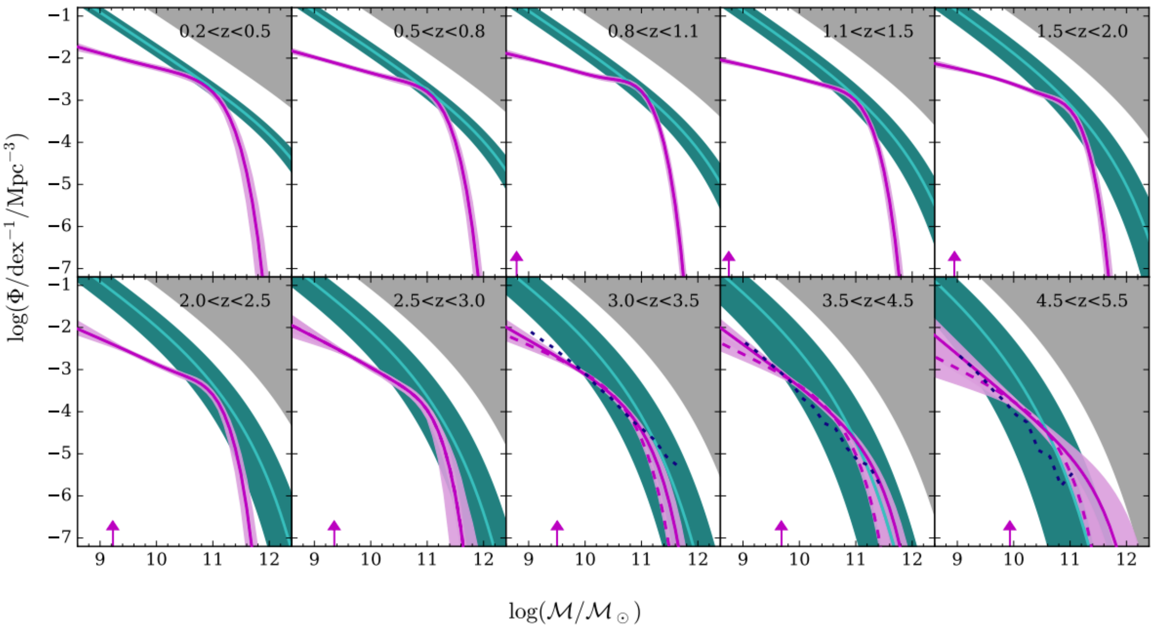

Figure 1.9: Below: The stellar mass function (magenta) plotted alongside the halo mass function at various redshifts from Davidzon et al. (2017). The solid magenta line is from their work, while the dashed magenta is a Press-Schechter stellar mass function. The shaded regions show the uncertainties. The sharp drop-off in the SMF compared to the HMF indicates a mechanism preventing high-mass galaxies from forming (mass quenching). Their work uses a collection of data taken from the COSMOS2015 catalog (Laigle et al. 2016).

1.2.3 Subhalo Orbits

Understanding the expected orbital path a subhalo will undergo and the properties that go into this prediction is vital. The influence of gravity dominates the motion of these objects, as other forces do not significantly affect the scales relevant to the orbit. According to Poisson's equation, we can determine the force of gravity acting on an object with the density field of the system:

$$\nabla^2\Phi = 4\pi G\rho \tag{1.13}$$

$$\vec{g} = -\nabla\Phi \tag{1.14}$$

$\vec{g}$ is the acceleration due to gravity, Φ is the potential field, and ρ is the density. Thus, given a density field, the acceleration can be determined for each object within it.

As noted above, an important aspect of the NFW profiles used to describe the density and potential of a halo is that they are spherically symmetric. Consequently, the orbital energy, E, and angular momentum $\vec{L}$ are conserved throughout an orbit. These are defined as:

$$E = K + U \tag{1.15}$$

$$\vec{L} = m_{\rm sat}\vec{r} \times \vec{v} \tag{1.16}$$

where $K = \frac{1}{2}m_{\rm sat}|\vec{v}|^2$ and U here are the kinetic and potential energy associated with an orbit. This means its energy and angular momentum can uniquely describe the orbit. It is common to define an orbit by its circularity, ϵ. It is defined as the ratio between the angular momentum of an orbit, L, and that of a circular orbit with the same energy, $L_{\rm circ}(E)$. $\epsilon = 1$ corresponds to a completely circular orbit, while $\epsilon < 1$ results in a more radial orbit. It is also necessary to define a characteristic length of time for these orbits. This is often given as $T_{\rm circ}$, the orbital period of a circular orbit at the virial radius of the halo.

$$\epsilon = \frac{L}{L_{\rm circ}(E)} \tag{1.17}$$

$$T_{\rm circ} = \sqrt{\frac{GM_{\rm vir}}{R_{\rm vir}}} \tag{1.18}$$

where $M_{\rm vir}$ and $R_{\rm vir}$ correspond to the virial mass and radius, considered the mass and radius defining a halo. Figure 1.10 plots the radius of an object in orbit in an NFW potential against time. It shows that orbits with lower circularity fall into the system faster and eventually reach smaller radii.

As noted previously, there is particular interest in the apsis of a subhalos orbit. The apsis is the location in an orbit where the object is either farthest (apocenter) or nearest (pericenter) to the center of the system. In the case of a static spherical potential, this can be determined by solving the following equation from Binney & Tremaine (2008):

$$\left(\frac{1}{r}\right)^2 + \frac{2[\phi(r) - E]}{L^2} = 0, \tag{1.19}$$

Where r is the radial position of the object.

It is also worth noting that non-circular orbits will also precess in their orbit. This means the angular location of the pericentre will change with each subsequent orbit. The amount of angular precession is given by equation 3.18b in Binney & Tremaine (2008):

$$\Delta\phi = 2L \int_{r_a}^{r_a} dr \frac{1}{r^2\sqrt{2[E - \Phi(r)] - L^2/r^2}} \tag{1.20}$$

where r_a and r_a are the pericentric and apocentrc radii.

For quenching models especially, it is also important to understand the time it takes to reach the pericentre, $T_{\rm peri}$, from the moment a subhalo merges with its host, $T_{\rm merge}$. This will be referred to as infall time:

$$T_{\rm infall} = T_{\rm peri} - T_{\rm merge} \tag{1.21}$$

As with all properties of an orbit in a static spherical potential, this will depend on the energy and angular momentum of the orbit. This can be seen in Figure 1.10, as the time it takes to reach the pericenter decreases as ϵ decreases.

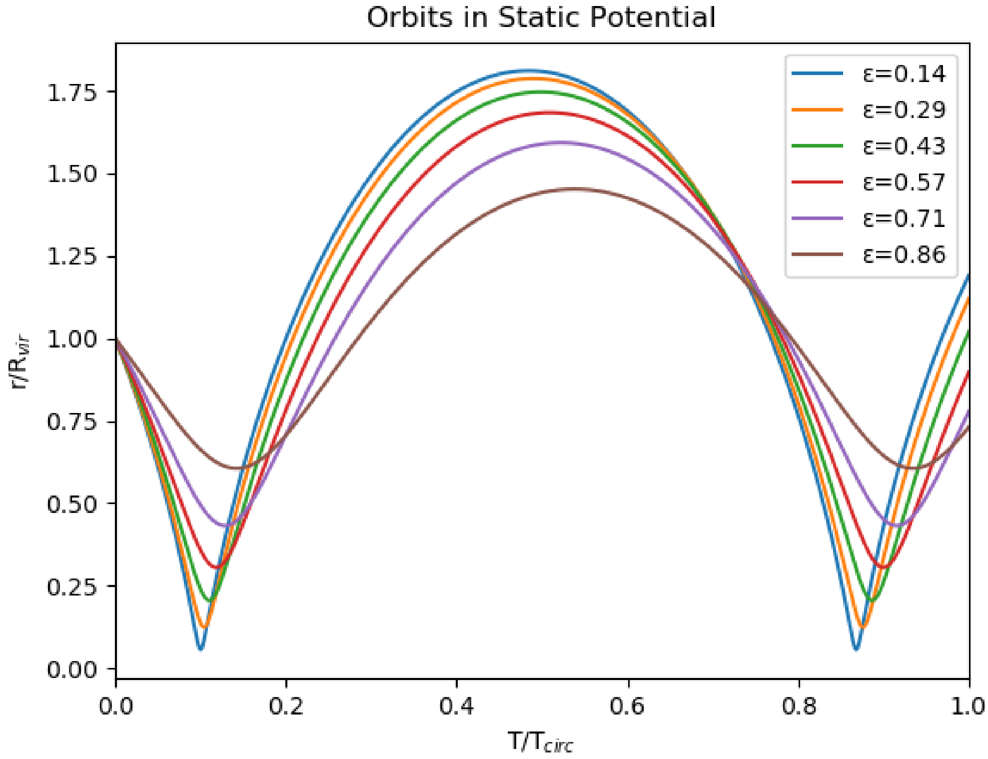

Figure 1.10: The different paths for an orbit with varying circularity. Here $R_{\rm vir}$ is the boundary of the host halo, and $T_{\rm circ}$ is the orbital period of a circular orbit at the $R_{\rm vir}$. These are generated by integrating an orbit forward starting in the same NFW potential with the same initial energy.

The problem with these descriptions of halo orbits is that they assume a static, spherical potential. However, these are only approximately true for a subset of real systems. As mentioned previously, halos form hierarchically. A consequence of this is that the density of the host halo changes in complex ways as halos merge. The radius, mass, and concentration parameters all change as a reflection of the dynamic history of the host, thus changing the potential (Taylor 2011). Also, these systems are not truly spherical and may be triaxial. This will cause orbits to naturally evolve as energy and angular momentum are not conserved. For reference, in A.1 I show various methods for defining and determining the density or potential in a triaxial NFW system.

Also, across the normal evolution of a host system, the host is expected to undergo periods with a violent change in its potential and more relaxed epochs where this change occurs smoothly. Hosts continually undergo minor mergers and accrete matter from the surrounding region. This can contribute a large portion of the total mass accreted, upwards of 40% (Genel et al. 2010). This slow accumulation of matter should not introduce significant amounts of heating to subhalo orbits but nonetheless will change the overall potential of the system. According to hierarchical halo formation, another portion of matter is expected to be accreted through minor mergers of smaller subhalos. This also should not drastically change the orbits of constituent objects but can introduce close interactions between neighboring subhalos.

However, during major mergers, the potential and mass distribution of the host halo will be heavily disrupted. During this time, orbits are expected to be heated due to the sudden influx of mass and energy. This can lead to individual orbital paths being modified and changed. Any structure to the distribution of orbits, such as objects closer to the center having merged earlier (Oman et al. 2013), may be changed during these events. Thus, major mergers can act to remove any information about the accretion history of the host left in subhalo orbits or the parameters of the host.

To best compare orbits in systems with differing host properties, energy, angular momentum, and velocity values are often scaled by a value consistent between all systems. For energy, (1.22), this is commonly the Keplarian potential energy associated with the host mass at the virial radius of the host. Angular momentum, (1.23), is scaled similarly by the angular momentum of a circular orbit at the same radius. A standard scale for velocity is the velocity of a circular orbit at the virial radius of the halo. These all scale with the mass and radius of the host and thus can be used to compare different systems. Since both energy and angular momentum scale linearly with the subhalo mass, the dependence on subhalo mass is removed by dealing with the specific energy and angular momentum, that is, the energy and angular momentum per unit mass of the subhalo.

$$E_{\mathrm{vir}} = \frac{GM_{\mathrm{vir}}}{R_{\mathrm{vir}}} \tag{1.22}$$

$$L_{\mathrm{vir}} = \sqrt{GM_{\mathrm{vir}}R_{\mathrm{vir}}} \tag{1.23}$$

$$V_{\mathrm{vir}} = \sqrt{\frac{GM_{\mathrm{vir}}}{R_{\mathrm{vir}}}} \tag{1.24}$$

1.3 N-Body Codes

N-body cosmological simulations provide a method to probe structure evolution through direct analysis of the motion and distribution of particles, which is essential to understanding the non-linear regime of halo evolution. The purpose of these simulations is to accurately model the motion of matter starting from initial conditions, mimicking that of the early Universe. The general components of these simulations involve including many particles, each with a set mass. These masses generate a potential field that can be used to determine their subsequent motion. These simulations often require a large cosmological volume to accurately include the interactions between other halos integral to structure formation.

The simplest approach to generating the potential Φ is to sum over the contributions of each particle of the simulation. Obviously, this is a large computation that can set limits on the simulation specifications. However, many techniques are used to address this, which are discussed below. Even with these techniques, there is a trade-off between the size of the simulation and the number of particles. In order to maintain the same overall density of the Universe, decreasing the number of particles equates to increasing their overall mass. Accurate structure identification requires a minimum number of particles, often on the order of 20. Thus, the mass resolution limits the sizes of subhalos a simulation can probe.

These simulations also include the evolution over significant cosmological times. This, as well as the required volumes, necessitates the inclusion of the expansion of the Universe. Including this will change the equations of motion, as the expansion acts to counter the effect of gravity. These simulations use comoving distances rather than changing distances and positions within the simulation at each time step. This ensures that the size of the simulation and coordinate positions are consistent throughout the simulation. This has the effect of changing the equations of motion to include the expansion of the Universe.

$$\ddot{r} + 2\frac{\dot{a}}{a}\dot{r} = -\frac{1}{a^2}\nabla\Phi \tag{1.25}$$

$$\nabla^2\Phi = 4\pi G\bar{\rho}a^2\delta \tag{1.26}$$

Careful consideration is required to model the boundary of these simulations accurately. The boundary itself is a nonphysical result of simulations, as it would introduce a region of zero density. This would generally cause all objects to condense at the center of the simulation. To account for this, periodic boundary conditions are used in most cosmological simulations. Periodic boundary conditions, in essence, include the effect of a copy of the simulation volume at the edge of the volume.

1.3.1 Calculating Potential

As noted in equations 1.25 and 1.26, the motion of particles can be calculated from the potential field Φ. This, in turn, can be generated from the region's density. In early simulations, this was done by summing over the contribution from each particle. This is known as the particle-particle (PP) method. This was sufficient for early simulations, but since the resolution of these simulations has increased, this has become unachievable. Several techniques have been employed to accurately include the effect of all particles while being computationally feasible.

One standard method is to make use of meshes. In this method, the simulation is separated into a set grid. The density of each grid is then determined from the position of each particle. This grid is used as a sample of the density field at set intervals in simulation. Sampling the density field in this way allows for a quick calculation of the potential, as it can use a fast Fourier transform (FFT). This is preferred as equation 1.26 in Fourier space can be described as:

$$-k^2\Phi(k) \propto \rho(k) \tag{1.27}$$

Thus, Fourier transforming the density values from the mesh can drastically speed up calculations. These methods can be combined with PP interactions by calculating the contribution from nearby particles but including the contribution from the mesh for particles farther away. Calculating meshes is also helpful in incorporating periodic boundary conditions.

Another common method is to use the fact that the resolution between particles further away is not necessary to accurately determine a particle's motion. Since gravity is a $1/r^2$ force, objects further away will inevitably contribute less overall force than objects nearby. Similarly, the angular change between different positions further away diminishes. This leads to the Hierarchical Tree method. The simulation volume is again split into different cubic regions in these codes. The particles within each region determine its density. These regions are generated at several resolutions at each time step, say 1/8 and 1/64 of the size of the box. Then, for each particle, the contribution from higher resolution regions is used for locations nearby. Contributions from regions further away then use lower resolutions. This significantly cuts down computational times. If needed, fluid properties such as pressure, density, and pressure can be incorporated into the simulations using smooth particle hydrodynamics (SPH).

1.3.2 Initial conditions

It is also key for these simulations to accurately generate initial conditions that match the expected properties of the early Universe. Any changes in the distribution of matter can drastically affect structure formation. In the early Universe, perturbations are small and are described by a Gaussian random field. As Gaussian random fields are completely described by their power spectrum, the chosen cosmology for a simulation can be used to generate initial conditions.

The issue with the initial density field is that simulations need to convert this into a distribution of particle positions and velocities. The initial conditions for the particles must match the initial density field. This is commonly done using the Zel'dovich approximation (Zel'dovich 1970), which relates the density at a specific location to the velocity of a particle within it.

The common method of generating initial conditions starts with a uniform pre-initial distribution of particles. A density field is also constructed by taking a white noise field, defined as a distribution with a constant power spectrum, and multiplying it in Fourier space by the desired power spectrum, defined by the cosmology of the simulation. The power spectrum used is generally taken to be that obtained from the CMB. This modified white noise distribution is sampled at specific frequencies, and inverse Fourier is transformed to real space. The pre-initial field is perturbed by the density distribution through the Zel'dovich approximation, and each particle is then assigned a velocity. This generates a particle distribution consistent with the desired power spectrum.

1.3.3 Zoom-in simulations

Zoom-in simulations aim to reconcile the issue of requiring both the large volume a halo will interact with throughout its evolution and the high resolution needed to model smaller-scale subhalos accurately. Particular interest to this project is using simulations capable of resolving both small-scale subhalos and their much larger host halo. This requires both the cosmological volume needed to simulate the evolution of the host system and the high mass resolution to identify subhalos. As noted above, this is unfeasible with modern technology, as the number of particles would exceed current computational limits. Zoom-in simulations combine these extremes.

To do this, we must start with a low-resolution simulation of a cosmological volume. This should have a resolution high enough to model the evolution of the large-scale structure of interest accurately. This initial simulation identifies a structure of interest, including all of its particles. The simulation is then rerun, where each constituent particle is split into smaller particles. Similarly, each particle within a region surrounding the dynamical volume traversed by the structure is split into several smaller particles. This gives an increased resolution for the structure of interest without rerunning the entire simulation at a high resolution. This process is then repeated several times until the desired resolution is reached. Taken from one of the zoom simulations used in this project, Figure 1.11 shows the radial position of particles of differing masses with respect to the center of the halo of interest. It shows clearly that the smallest mass particle occupies the regions closest to the host center, with the highest mass particles located in regions further away.

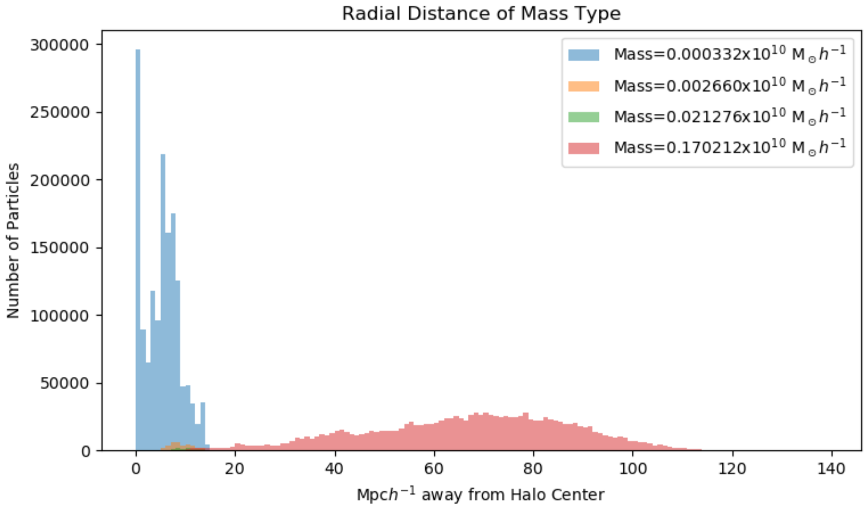

Figure 1.11: Histogram of particle positions colored by mass for a zoom-in simulation used in this work. The x-axis shows the distance in Mpc away from the center of the host halo. After several iterations of zooming in, the region closest to the halo center contains mostly low-mass particles (blue), while regions further away contain only higher-mass particles (red). Note that there are very few mid-sized particles (orange and greed), as they lie within the dynamical region of the host. This means the majority of them are converted to higher-resolution particles.

1.3.4 Simulation Outputs

The standard output files for these simulations are called snapshot files, which describe the position and velocity of each particle, as well as the specifications of the simulation at that time. These can include the Universe's redshift, critical density, and scale factor at the time of the output. These outputs must be output at a cadence sufficient for meaningful analysis. Deciding the cadence in terms of redshift or scale factor is common, as these track structure evolution in the linear regime. Depending on the size of the simulation, these snapshot files can be $\sim$ 10Gb. It is then necessary to carefully manage the number of snapshots to minimize space and maximize available information.

1.3.5 Halo Finders and Merger Trees

The output of simulations does not include any information about the halos that make up large-scale structures, just the position and velocity of each particle within it. A separate program is required to analyze these outputs to extract information about the halos present in each file. These programs are known as halo finders. The two common methods halo finders use are friends-of-friends (FoF) and spherical overdensities (SO). A linking length must be chosen in FoF, usually some factor of the average particle spacing. It then links neighboring particles if they are within this linking length. If a collection of linked particles contains sufficient particles, it is considered a halo. Then, properties such as mass, radius, and shape are determined using the particles that define the halo. One issue with this method can arise as two halos approach each other during merging events. In this case, the two separate halos can be flagged as one large structure. Thus, the linking lengths chosen in these analyses can heavily affect these results.

SO is a different approach that often avoids the issue of choosing a linking length. Starting from a low resolution, SO halo finders instead find regions of high density. They then find the contours of isodense regions around these particles. Particles are then flagged as part of a given halo if they are within an isodense region larger than $200\rho_c$ (or some other definition of density) and are bound to the halo center. These regions are then iteratively examined with higher resolution until all constituent particles are identified.

Each of these approaches identifies halos in a given snapshot. Given that each simulation may have hundreds of outputs, it is necessary to accurately link halos between snapshots to analyze the evolution of halos. This necessitates using programs that generate merger trees containing information about a halo as it evolves throughout the simulation. The common way this is done is to examine a given halo's constituent particles and compare them to halos found in a neighboring snapshot. If a sufficient fraction of particles overlap between snapshots, one is labeled as the progenitor of the previous one. Note that these halos can have substructure, meaning multiple halos will have overlapping particles between snapshots. Generally, the halo that contains the largest fraction of particles in a previous snapshot is chosen as the progenitor. This process will lead to a merger tree, with a main branch following the most massive progenitors and many minor branches indicating mergers between halos.

Chapter 2

Modeling Subhalo Orbits

2.1 Data

This work uses a set of three zoom-in simulations for a detailed analysis of subhalo formation. The original, low-resolution simulation was carried out using GADGET2 (Springel 2005), starting from z=200 to z=0. This simulation had a box size of $140h^{-1}$, a mass resolution of $1.7 \times 10^9 M \odot h^{-1}$, and a softening length of 5.469 kpc h^{-1}. The initial conditions were generated using the package MUSIC (Hahn & Abel 2011), with displacements generated by the CAMB package (Lewis et al. 2000). The cosmology used is a variation of the Plank cosmology, using $\Omega_{m,0} = 0.3$, $\Omega_{\Lambda,0} = 0.7$, $H_0 = 68$ km/s/Mpc, σ_8=0.82 and n=0.96. Three host halos were chosen after running a FoF halo finding algorithm (Kim & Park 2006). Following Oñorbe et al. (2013), the simulation was rerun to increase the resolution of these host halos. The final resolution of simulations included particle mass $m_p = 3.32 \times 10^6 M_{\odot} h^{-1}$ and a softening length of 0.683 kpc h^{-1}. The output of these re-simulations included 120 snapshots ranging from redshift z=9 to z=0.

To generate the halo catalogs from these simulations, Amiga Halo Finder (AHF) (Knollmann & Knebe 2009) was then run on each snapshot in the set to both identify host and subhalos and generate the halo trees of each subhalo of the hosts. AHF works by reading through the particle positions and velocities from a simulation. The volume is first separated into a coarse grid called the domain grid. The domain grid is set to contain 128 cells. If a cell has more than a set number of particles, it is chosen for refinement. This work uses a refinement criteria of 4 particles per cell for all refinement levels. The maximum number of cells is set to 2^{30}. Once no cell requires refinement or the maximum number of cells is reached, the tree of nested grids is complete.

Next, starting from the finest grid, isolated regions are marked as possible regions containing halos. This is done for subsequent coarser grids, where fine grids that are subsets of coarser grids are linked as the same structure. Substructure is determined by different isolated regions in a finer grid being linked to the same coarse grid. Each particle within a collection of grids defined as a single halo is initially defined as bound to the halo. If the velocity of a particle is greater than a set velocity, in this case $1.5\nu_{\rm esc}$, it is considered unbound. This process is iteratively done until there are no longer any unbound particles.

Finally, the halo properties are determined using a halo's identified particles. The halo center is defined as the location of the center of mass of the collection of particles. The halo radius, $R_{\rm vir}$, is chosen to be the maximum radius at which its density is equal to $200\rho_{\rm c}$. From the distribution of particles, various other halo properties can be calculated. Merger trees are also generated using the same code package. The progenitor halo is chosen from halos in the previous snapshot if it contains the largest number of particles in common. Thus, for each host and subhalo, its complete history is available.

2.1.1 Energy and Angular Momentum of Subhalos

The energy and angular momentum of a subhalo are calculated in the frame of the host system. For each snapshot, AHF outputs the velocity and position of each identified halo. Thus, the velocity and radius of each subhalo are defined as:

$$\vec{r}_{\text{subhalo,rel}} = \vec{r}_{\text{host}} - \vec{r}_{\text{subhalo}} \tag{2.1}$$

$$\vec{v}_{\text{subhalo,rel}} = \vec{r}_{\text{host}} - \vec{v}_{\text{subhalo}} \tag{2.2}$$

AHF also outputs the mass, radius, and concentration parameter of each halo identified in each snapshot. Using this, the NFW potential, $\Phi_{\text{nfw}}(r)$, can be calculated for each host in each snapshot. Thus, the specific energy is calculated for each subhalo as follows:

$$E = \frac{1}{2}|\vec{v}_{\text{subhalo,rel}}|^2 + \Phi_{\text{nfw}}(\vec{r}_{\text{subhalo,rel}}) \tag{2.3}$$

Similarly, the specific angular momentum is defined as:

$$\vec{L} = \vec{r}_{\text{subhalo,rel}} \times \vec{v}_{\text{subhalo,rel}} \tag{2.4}$$

2.1.2 Timing of Subhalo Mergers

To investigate the properties at infall, it is necessary to have a precise definition of when subhalos first infall into their host. If the entirety of the simulation were available for analysis, it would be ideal to use the results of a halo finder to pinpoint when a subhalo merges with its host. However, this becomes more complicated due to the finite cadence of the simulation output. The method used to generate this catalog of infall parameters starts with using the output of AHF on each of the simulation outputs. As described above, this generates the merger tree for each halo identified in the simulation. Each eventual subhalo of a host is then flagged, and its position is tracked across the entire snapshot. At the same time, the relevant properties of the host are also tracked at each snapshot.

The merger time is identified when a subhalo first crosses the virial radius. To determine when this occurs, the radial position with respect to the host center is determined in each snapshot. Starting from the highest redshift snapshot, the radial position of a subhalo in pairs of subsequent snapshots is checked until $R_n > R_{vir,n}$ and $R_{n+1} > R_{vir,n+1}$, where n and m are the higher and lower redshift snapshot respectively. Between these two outputs, the subhalo must have crossed the virial radius. The radial position of the subhalos with respect to the host center is then found in the surrounding five snapshots. Using this, a third-degree spline is generated in redshift and solved for the redshift z_{infall} such that

$$r_{subhalo,rel}(z) - r_{\text{vir, host}}(z) = 0.$$

Following this, a similar third-degree polynomial function of redshift is fit for other parameters, such as mass and the components of its velocity. Each function is then evaluated at z_{infall}, resulting in the interpolated properties of the host at the time of infall. With both the host and subhalo properties at z_{infall}, the radial and tangential velocities and the host mass and virial radius are found. As noted above, these are used to scale the velocity of the infalling subhalo. For the three simulations, there is a total of 46000 infall subhalos.

A commonly used parameterization of infalling properties is the velocity vector at the time of infall. The total velocity can be used as a metric for the total energy, while the tangential velocity describes the angular momentum. By definition, these values are determined at the virial radius. Assuming a spherically symmetric potential field, such as a Keplarian potential, the potential energy should always be given by equation (1.22) at the time of merging. This means the varying component of the total specific energy between subhalos is its specific kinetic energy, which depends solely on its velocity. Similarly, since objects merge at the same radius, the angular momentum only depends on the tangential or radial component of the velocity.

This can also be scaled to account for varying host properties. This is often chosen to be the velocity of a circular orbit at the virial radius, with the radial component scaled to the total velocity:

$$V_{\text{tot}} = \frac{\nu}{V_{\text{vir}}} \tag{2.5}$$

$$V_r = \frac{\nu_r}{\nu} \tag{2.6}$$

where ν and ν_r are the subhalo's total and radial physical velocities at the time of the merger.

2.1.3 Pericentric Passage

To determine the changes in the distribution of pericentric passage, as in Section 2.3, we follow a similar process as above. We generate a catalog of pericentric passages by first determining the relative positions and velocities of subhalos with respect to that of the host system at each simulation output. Finding the orbital radii for each snapshot, we find the snapshot at which it reaches a minimum. Keep in mind there are times when the position may jump artificially, indicated by three subsequent snapshots indicating the object is at an extremum of its orbit. In these cases, I disregard the middle snapshot and continue with the process.

Although the snapshot corresponding to the pericentric passage is identified, this will be of low temporal resolution, as the location of the pericentre may be between snapshots. To address this, I create a third-degree fit in redshift using the surrounding five snapshots. Note that creating fits in cosmic time does not change these results significantly. From these fits, I find the redshift and the radius of the pericentric passage. Using the catalog of infall parameters, the time between the moment of infall and pericentric passage is calculated. The final catalog includes the time between infall and pericentric passage t_{Infall}, and the pericentric radii R_{peri}. This was calculated for each object that reached its pericentre. Between all hosts, this corresponds to a total of $\sim$18000 orbits. Infall time is scaled by T_{circ} and the pericentric radii by R_{vir} at the time of the merger.

2.2 Orbital Properties at Infall

The properties of a subhalo's orbit at the time of infall are of significant interest, as they should dictate the subsequent motion of the merging subhalo. To understand the distribution of these parameters, it is important to understand the evolution of subhalos before they cross the virial radius. In the early Universe, the host halo starts as a small overdense perturbation in an otherwise homogeneous density field. In the simplest case, surrounding subhalos initially expand away from the host center and are unbound to the host. The higher-density region of the host attracts surrounding subhalos that eventually move against the Hubble flow and fall back toward the host system at the turnaround radius. At this point, the subhalo's orbital energy will be purely potential, given by $GM_{\rm vir}/R_{turn}$. The potential energy will be converted to kinetic energy as it falls back toward the host. When the subhalo crosses the virial radius, the velocity equals that of the virial velocity (1.24). Thus, in this simple picture, the velocity at the time of the merger should be exactly the virial velocity, regardless of host properties.

The issue with this picture is that subhalos do not evolve in isolation. During the time prior to the crossing of the virial radius, subhalos will experience forces from other surrounding objects. The surrounding objects will not have symmetry and thus will apply a tidal force on the subhalo. This can have the effect of introducing or increasing the tangential velocity of the object, in turn increasing the object's total velocity. This should also decrease the component of an object's total velocity in the radial component at the time of infall. Shown in figure 2.1 is the distribution of infall velocities from the simulations in this work. It shows that the distribution peaks at a value slightly above the virial velocity and that more radial orbits are more common than tangential orbits.

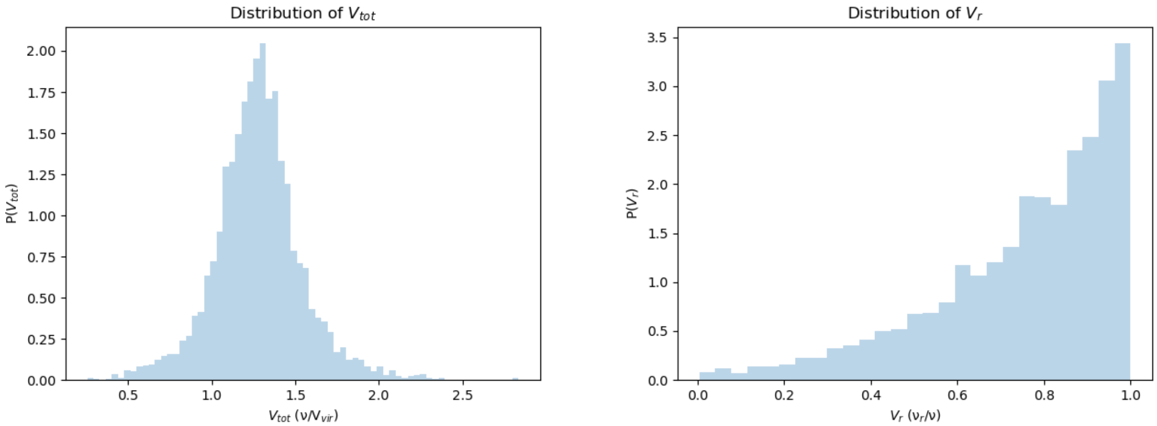

Figure 2.1: On the left is the total velocity of each subhalo that infalls into each of the three host systems, scaled by the virial velocity at the time of the merger. Similarly, to the right is the infall radial velocity, scaled by the total velocity of a given object when it merges with its host.

Without any assumptions about the stability of host potentials, many studies support the conclusion that the parameters at infall relate to their subsequent motion. Tormen (1997) find correlations between circularity at the time a subhalo merges with its host and pericentric location. Khochfar & Burkert (2006) find that for merging galaxies, there is a slight correlation between the predicted pericentric radii and eccentricity at the time of the merger. Overall, it is found that the dominant predictor of pericentric radii is tangential velocity at infall. Thus, if the potential of these systems is stable enough for the expected orbital properties to hold, with some scatter.

This leads to the following interpretation of subhalos' evolution before and after they merge with their host. Subhalos initially follow the predictions of spherical collapse and then gain tangential velocity, spin, and angular momentum through interactions with other halos before merging. At the time of the merger, depending on their infall parameters, they follow a path that leads to pericentre. The specific pericentric location dictates the level of tidal stripping and galaxy quenching. Similarly, interactions with other subhalos can significantly change their structure. Thus, infall parameters that can predict pericenter are necessary to predict the evolution of galaxies and subhalos.

Tracking and understanding the complex evolution of a subhalo is not feasible for all substructures. Thus there has been a large amount of work done to identify the relationship between infall properties of substructure, and properties of host systems.(Tormen 1997; Wetzel 2011; Benson 2005; Jiang et al. 2015; Vitvitska et al. 2002). Jiang et al. (2015) find relations between the infall velocity and host mass, and mass ratio. Wetzel (2011) examines the relation of infall parameters to host mass, redshift, and satellite mass. Similarly, Benson (2005) looks into mass and redshift dependence, and although they do not discuss a physical reason, argue that their results suggest there is a redshift dependence but cannot disentangle it from the inherent mass dependence. Tormen (1997) finds that circularity peaks at around 0.5 and that more massive satellites have smaller pericentres and a larger radial velocity, leading to a more eccentric orbit. Similarly, Wang et al. (2005) finds that they lie primarily along the major axis. In this section, I examine the validity of some of these relations and determine if they should hold across the evolution of a host system.

2.2.1 Mass Ratio

The host-subhalo mass ratio, M_s/M_h, can predict the conditions a subhalo will experience before and during its infall onto a host. When dealing with galaxy clusters, the hosts are generally high mass and thus exist on the tail end of the halo mass function. This means they are relatively rare since the low number density (see Figure 1.8). Thus, for the infalling subhalos, the host should be among the few structures of similar sizes relevant to its history. This would mean, especially for higher mass objects, there are expected to be very few objects other than the host capable of introducing a significant tangential velocity. However, as the mass ratio between the satellite and host decreases, the satellite in question will be smaller in mass. This means the number of larger subhalos capable of influencing its motion will be increased. Thus, objects with a low mass ratio are expected to have a more significant component of angular momentum, causing an increase in the total velocity and a decrease in its radial component.

In the region surrounding the host system, the heating of a subhalo's motion is expected to be caused by the contribution of other halos in the immediate vicinity of the eventual host. Lower mass subhalos are expected to be more susceptible to this heating since the same force will cause smaller subhalos to accelerate more toward these other halos. Similarly, at lower masses, there are expected to be more higher-mass objects in the field that can contribute to this heating. In this picture, objects with a lower mass ratio with their host should gain tangential velocity prior to their merger, thus increasing $V_{\rm tot}$ and decreasing V_r. At the higher ratio end, the heating is expected to be less effective, so both $V_{\rm tot}$ and V_r should tend toward 1.

Figure 2.2 shows the average $V_{\rm tot}$ and V_r for different bins of $\log_{10}(M_s/M_h)$ for all merging subhalos in our simulations. To isolate the effect of mass ratio, I restrict the host mass to $10^{13-14} M_\odot h^{-1}$. I find that at lower mass ratios, the V_r approaches about 0.75 in the lowest bin, and $V_{\rm tot} > 1.2$. At high ratio bins $V_{\rm tot}$ and V_r approaches 1. This supports the picture above, as high mass ratios tend toward lower values. This general result is also found by Jiang et al. (2015), who find infall velocities increase for lower mass ratios for all host masses.

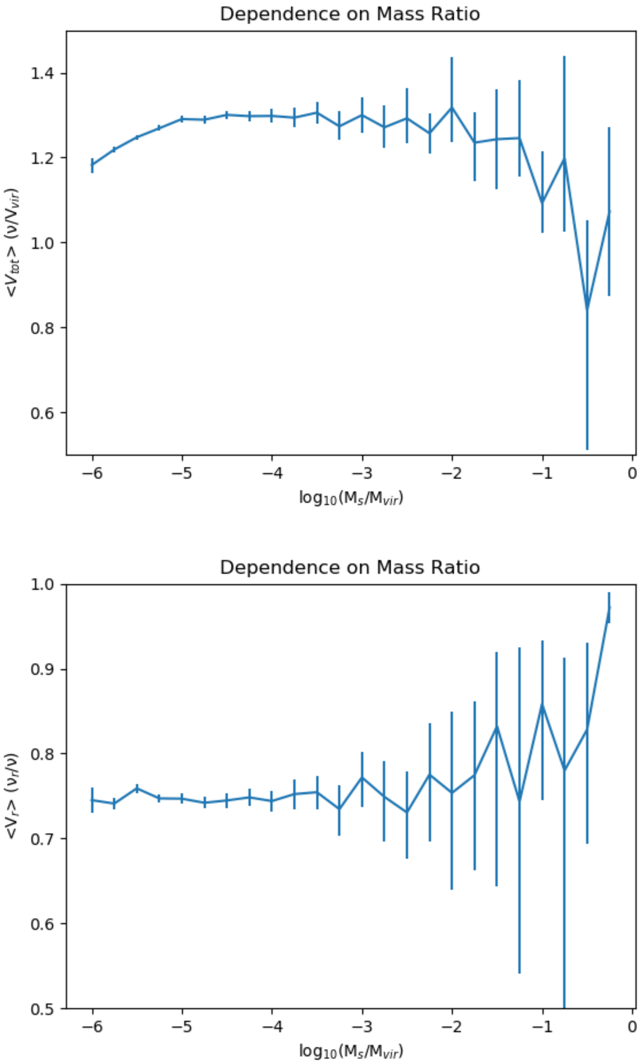

Figure 2.2: Above is plotted the average V_{tot} against the mass ratio of the subhalo at infall. The error bars are generated through a bootstrap method, with a confidence level of 0.98. Below is the same, but for the average V_r. From left to right are the different hosts. As the mass ratio increases, the total velocity approaches V_{vir}. At the same time, the V_r approaches 1.

2.2.2 Host Mass

The total host mass can also be linked to the environmental conditions experienced by a merging subhalo. In the picture of subhalo evolution, higher masses will dominate the local field. Since increasing the host mass corresponds to a more significant virial velocity, as shown in equation 1.24, the merging subhalo must gain an increasingly large velocity before merging to see a change in the distribution. Given that it is rare for merging subhalos to have another nearby large halo, and considering that these hosts are on the high end of the HMF, this heating should be increasingly infrequent at higher host masses. The radial component of the velocity can also be explained from this picture. Since higher mass hosts are expected to dominate the potential field, the radial velocity of infalling subhalos should be a larger component of its total velocity. This particular relation is also interesting, as host mass is a commonly measured property defining host systems. Incorporating any dependencies on this value can thus be useful for SAMs.

Since the mass of the host is tied heavily to the evolutionary history of the host, it is important to separate the results for each of the three host systems. This can indicate whether the results are consistent with an overall trend in host mass or if it is difficult to disentangle these results from that of the specific dynamical state of the host. According to Jiang et al. (2015), separating the population into mass ratio bins, the effect of increasing host mass is very slightly in the opposite direction; increasing host mass leads to an increase in infalling velocity.

From Figure 2.3, the expected relation to host mass is not shown. Errors are calculated through bootstrap re-sampling with a confidence level of 0.98. Since the errors are small, our results show a significant weak trend across host mass. This suggests that, although possible if averaged across many halos (Wetzel 2011), the infall parameters for individual halos do not follow the expected relation to host mass. There are also portions of the plot where the relation seems to deviate from a smooth relation, such as when the total velocity of the first host is a mass of about $10^{13} M_{\odot} h^{-1}$. This suggests the infall velocity can depend closely on the specific conditions of the host system.

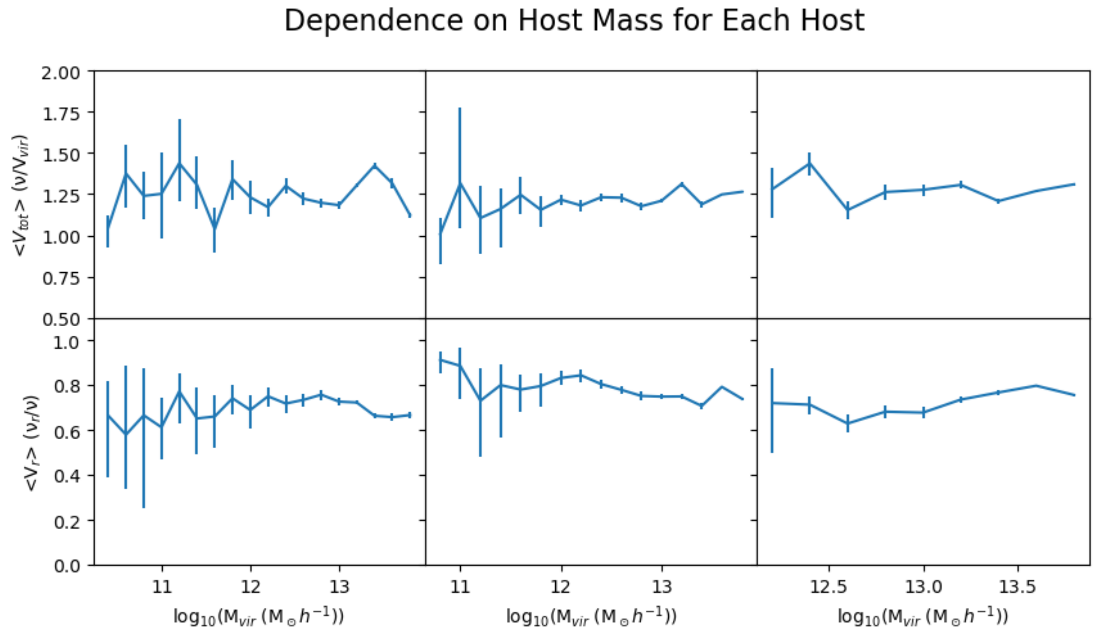

Figure 2.3: Above is the average V_{tot} plotted against the host mass at the time of the merger. The columns separate the data into the three host halos used in this work. To the right is the same but for average V_r. There is little dependence on host mass for both of these quantities.

2.2.3 Redshift

At high redshift, the Universe is highly uniform and isotropic. Due to the linear collapse of halos, as the Universe evolves, the contrast between over-dense and under-dense regions increases. This should increase the tidal field's strength outside the host's boundary and thus change its effect on subhalos' infalling properties. It is thus expected that as redshift decreases, the component of the velocity in the radial direction, V_r/V_{total}, should also decrease. Each interaction is expected to result in the subhalo being subjected to a larger tidal field, thus increasing the tangential velocity of its orbit. This should also have the effect of increasing the total velocity of infalling objects.

V_{tot} and V_r are plotted against infall redshift for host masses of $10^{12-14} M_{\odot} h^{-1}$ and mass ratio between 10^{-2} and 10^{-5}. Again, it is necessary to separate this into each of the three hosts, as the specific history of each may change these results. The results show a steady increase in V_{tot} at lower redshifts and a decrease in V_r. This supports the picture of increasing tidal interactions discussed above. Note that Wetzel (2011) find a similar decrease in V_r, but a consistent V_{tot} with decreasing redshift.

Similar to host mass, Figure 2.4 tracks the evolution of infall velocity across redshift. Errors are calculated similarly to 2.3. Although the expected relation is generally shown, with infall velocity increasing at low redshift, it is again clear that fitting an overall trend line is not feasible. There are periods for each host where the infalling parameters seem to be disconnected from surrounding data points. This again suggests that the history of the host plays a crucial role in subhalo infall parameters. Redshift alone cannot predict the complex conditions relevant to infall parameters.

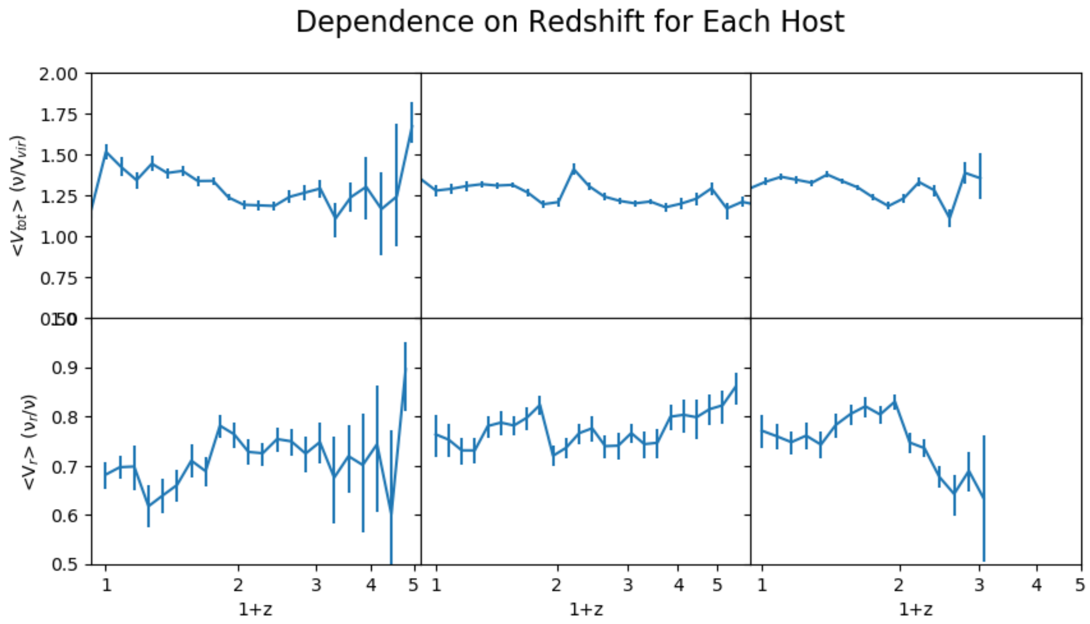

Figure 2.4: Above is the average V_{tot} plotted against the scale factor at the initial merger time. Below is the same, but for average V_r. The total velocity increases as the scale factor decreases, with a corresponding decrease in V_r.

2.2.4 Dynamical State

From the previous results, it is clear that the specific conditions of the host system may be required to accurately predict the parameters of merging subhalos at infall. One aspect of this should be the level to which the host is relaxed. As host systems evolve through merging events, they will experience periods in a relaxed state, where the motion and orbit of objects are allowed to settle. However, when a host system undergoes a major merger, there can be a drastic change in the matter distribution of the merging systems. The effect this may have on infalling subhalos is poorly understood. Major mergers heat the mass distribution, causing long-lasting changes to the potential and possibly affecting the motion of nearby subhalos.

Merging satellites also do not always merge as isolated objects. A similarly sized host halo is expected to in itself contain subhalos. This means that there will be discrete locations of higher density along with a change in the overall density. These can cause close interactions with other infalling objects, thereby changing the path of both.

The dynamical state of a cluster is generally quantified first through the substructure within the host system. Over time, the substructure within the host system is expected to become disrupted. This can be caused by interactions between subhalos, tidal stripping, or subhalos merging with the core galaxy of the host. Two similarly sized halos merge during major mergers, so a large portion of the halo's matter will be in the merging element. Thus, a common method of identifying the dynamical state of the system is simply the total mass found within the substructure, called the substructure fraction.

$$K = \sum_i M_{s,i} \tag{2.7}$$

Following Cui et al. (2018), this does not include the mass of the largest substructure, as the structure responsible would be the central halo of the system. $K < 0.05M_{\text{vir}}$ for a dynamically relaxed system. This f_s is defined as $f_s = K/M_{\text{vir}}$.

Next, the total energy of the constituent particles should indicate the level to which a cluster is relaxed. During major mergers, heat is expected to be imparted into the system. This would increase the total amount of kinetic energy. Thus, another method for determining the dynamical state is through the virial ratio η. This value measures how well the halo follows the virial theorem. It is calculated using the total potential energy, U, the total kinetic energy, T, and the energy associated with the surface pressure, E_s.

$$\eta = \frac{2T - E_s}{|U|} \tag{2.8}$$

E_s for collisionless particles is calculated following Shaw et al. (2006). As noted by Cui et al. (2018), a dynamically relaxed system will have $0.85 < \eta < 1.15$. Ideally, η approaches 1 for systems in complete virial equilibrium.

Lastly, during major mergers, the introduction of a large mass is expected to shift the position of the center of mass. As the central position of these halos is defined as the location of the highest density, the offset between the center of mass and this location can also indicate major mergers. This offset, Δ_r, is normalized to the virial radius of the host halo. We follow Cui et al. (2018) and use 0.04 as the limit for a dynamically relaxed system.

Combining these three factors, we follow Haggar et al. (2020) to assign a value for the dynamical state, χ_{DS}. $\chi_{\mathrm{DS}} > 1$ indicates a dynamically relaxed system. The system becomes less dynamically relaxed as $\chi_{\mathrm{DS}} \rightarrow 0$.

$$\chi_{\mathrm{DS}} = \sqrt{\frac{3}{\left(\frac{\Delta_r}{0.04}\right)^2 + \left(\frac{f_s}{0.1}\right)^2 + \left(\frac{|1-\eta|}{0.15}\right)^2}} \tag{2.9}$$

Using this, we can determine the dynamical state at the infall time for each subhalo and whether infall parameters are affected by unstable periods of a host's evolution. As this is commonly a binary, we instead plot the distribution of infall parameters for the lowest and highest quarter of the dynamical state. The two distributions are shown in Figure 2.5. Running a K-test comparing these distributions shows they are incompatible, with a p-value less than 0.001 for both. Although the general shape seems consistent between the two distributions, it is clear that objects with a lower dynamical state peak at a lower velocity. This suggests that during calm periods of a host's history, the infall velocity will approach closer to the virial velocity. This is consistent with the idea that objects that merge during dynamically unrelaxed periods (Q4) are more heated than those of relaxed periods. This is also supported by an increase in the number of radial orbits for objects that merge during relaxed periods. Thus, the dynamical state is a relevant parameter for predicting the velocity of infalling subhalos.

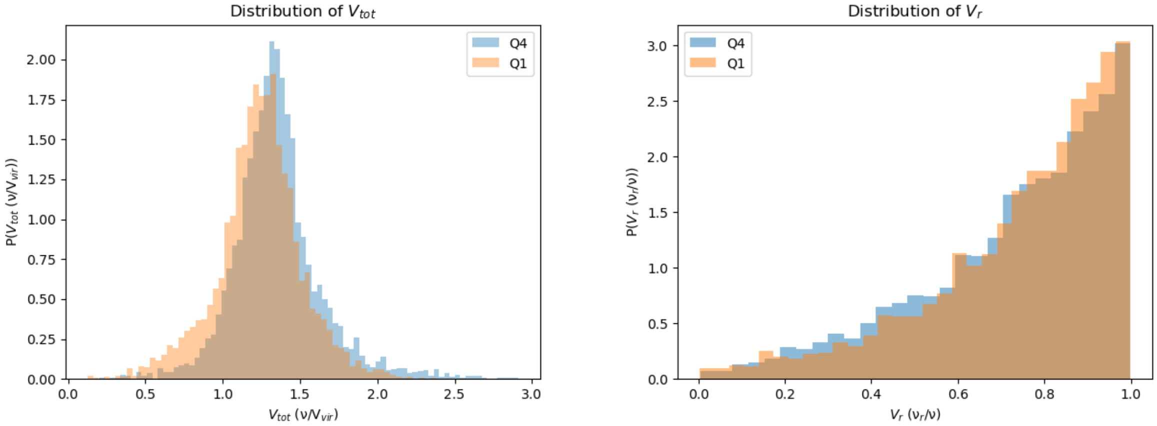

Figure 2.5: On the left is the distribution of V_{tot} for both the upper (blue) and lower 25% (orange) of subhalos ordered by the dynamical state of the host. To the right is the same, but for V_r. The upper 25% corresponds to the more dynamically relaxed population. There seems to be a slight decrease in V_{tot} for the less relaxed objects and a slight preference for less radial orbits.

2.2.5 Subhalos Merging as Groups

Another consideration for the status of merging subhalos is whether they merge after merging with a different host or if they merge directly from the field. Subhalos that have merged with a different host prior to the merger with the final host are expected to be fundamentally different from objects that merge in isolation, as their potential is dominated by the mass distribution of their previous host. We will call this population preprocessed, as this often indicates their star formation is affected prior to the merger with the final host. This can lead to these subhalos merging on orbits of their previous host, not just that of the cluster. Similarly, if they are particularly bound to their previous host, they may follow more radial orbits consistent with the higher mass of their previous host.

This can be easily found in the merger history, created from the entire simulation of each subhalo. Figure 2.6 shows the varying distributions. A KS test shows the distribution of V_r and V_{tot} is not consistent between the two populations, with a p-value of for both total and radial velocity less than 0.001. The population of V_{tot} seems to have a wider distribution. Since these objects merge as part of a larger structure, it is expected that their motion is not dominated by only the host halo, thus adding scatter to their total velocity. There does not appear to be any clear indication of a preferred direction of this scatter.

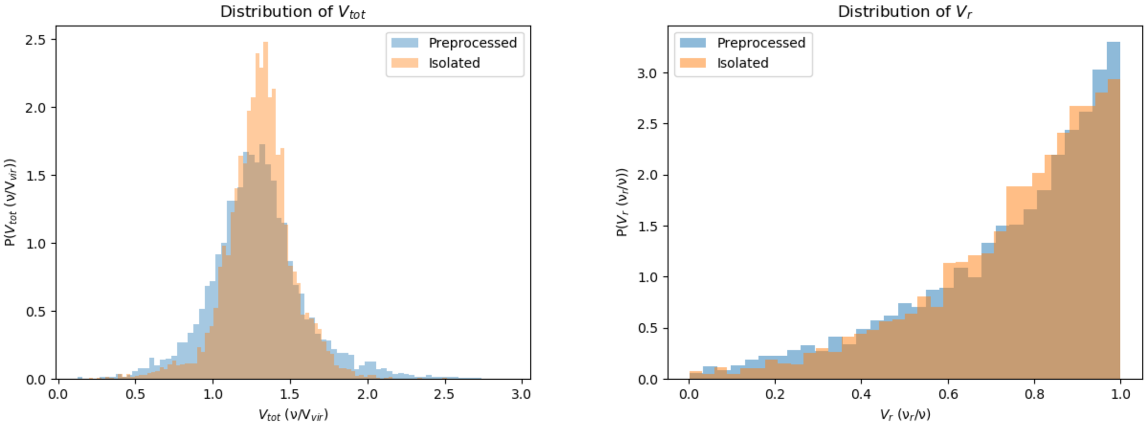

Figure 2.6: Same as Figure 2.5, but in orange is the population of subhalos that merge isolated, and in blue are subhalos that merge preprocessed. The population of preprocessed subhalos has a wider distribution for the total velocity.

2.2.6 Halo Boundary

Although it is commonly assumed for the system to be spherically symmetric, halos are not entirely spherical and may require a triaxial system to model accurately. Extensions to spherical collapse have led to the so-called ellipsoidal collapse model, in which the shape of a halo is instead modeled as an ellipsoid. The ellipsoidal boundary is obtained through the moment of inertia of the host, taking into account bound particles. The total angular momentum naturally gives the direction of the axes of the ellipsoid. From this, the moment inertia about these axes can be calculated. This defines an ellipsoid with an interior defined below.

$$\frac{x'^2}{a^2} + \frac{y'^2}{b^2} + \frac{z'^2}{a^2} = 1 \tag{2.10}$$

where x', y', and z' are the ellipsoid's largest, middle, and smallest axes, respectively. a, b, and c are the lengths of the semi-axes. Thus, I follow a similar approach to determine when an object merges under this boundary, as with the spherical case. First, I run through each snapshot to find one such that $\frac{x'^2}{a^2} + \frac{y'^2}{b^2} + \frac{z'^2}{a^2} < 1$. Then, a fit function is generated using a third-degree spline using the surrounding five snapshots for the subhalos properties and the axes of the host halo. I then find the redshift such that it crosses this boundary and determine the infall parameters from the fitted functions.

Lacking spherical symmetry, a system described by an ellipsoidal boundary will have differing conditions at the time of infall. Depending on the merger's location, the radius at which an object merges with its host will also vary, and more importantly, the potential will change. Another consequence of a system without spherical symmetry is that angular momentum is no longer conserved. This means that subhalos can gain tangential velocity from the host itself depending on the orbital path. This effect should also be more prominent along the shorter axes of the ellipsoid, as more mass should be concentrated along the largest axis. Thus, for highly triaxial systems, radial velocity distribution may also depend on the merger's location.

2.2.6.1 V_{tot} and V_r

Figure 2.7 shows the distribution of infall velocities comparing the spherical and ellipsoidal boundaries. A KS test run on both distributions indicates they are indeed different distributions, with a p-value of less than 0.001 for both V_r and V_{tot}. However, there appear to be very slight changes to their distributions. This suggests that any effect of the ellipsoidal shape of the halo does not change the overall distribution.

However, there may still be a dependence on the merger's location. To test this, we can look at the infall parameters as a function of its location. Using the spherical definition, I track where a subhalo merges with its host. Since this is expected to be dependent on the triaxial shape of the host, I bin by $\cos\theta$, where θ is the angle between the location a subhalo merges with its host and the largest axis of the host's moment of inertia. This is shown in Figure 2.8. There seems to be little dependence on the location of the merger. There is a slight increase along the largest axes of the ellipsoid, corresponding to a subsequent decrease in the radial component of the velocity. This suggests that objects that merge along the largest axes have less radial orbits, although this effect is small.

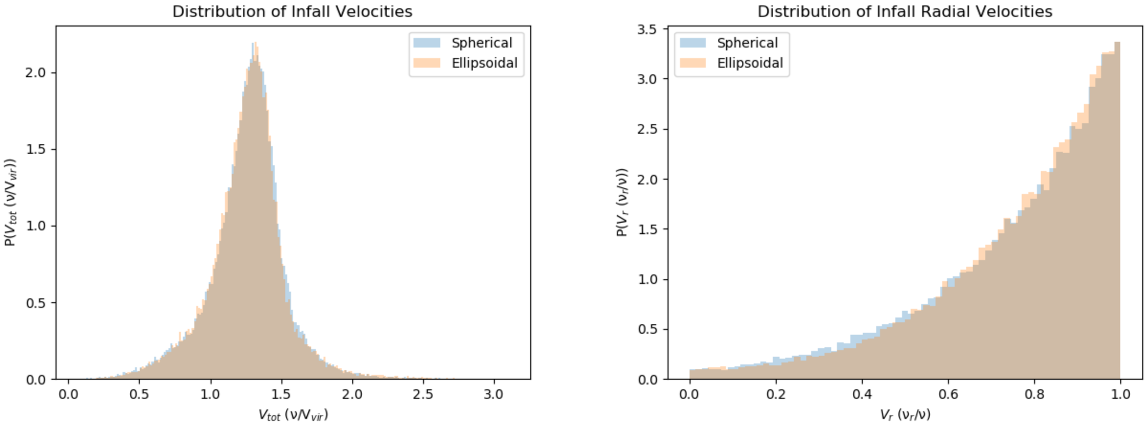

Figure 2.7: Same as Figure 2.5, but in orange are orbital properties at the time of merging for an ellipsoidal boundary, and blue are that for a spherical boundary.

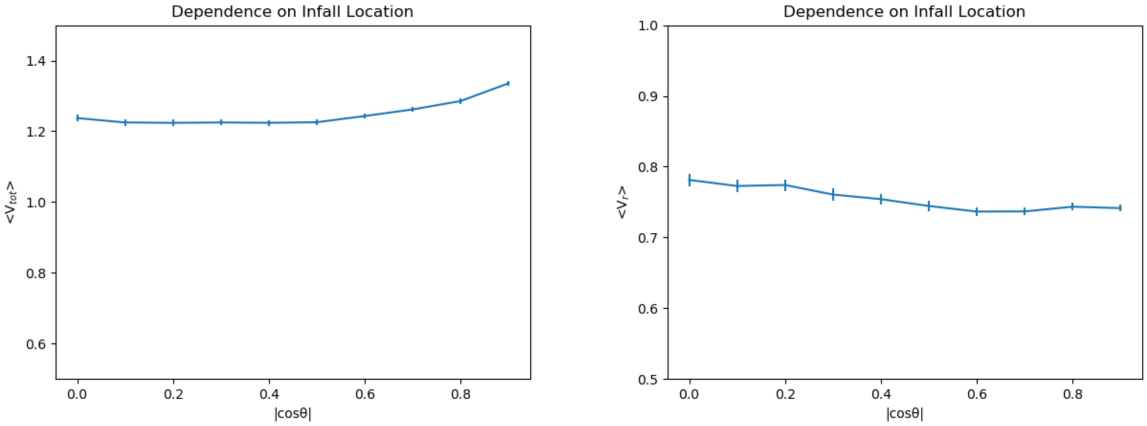

Figure 2.8: To the left is the average $V_{\rm tot}$ split into bins of $|\cos\theta|$. To the right is the same but for average V_r. There is a slight increase in $V_{\rm tot}$ for objects that merge in the region around the longest axes of the ellipsoid, with a corresponding decrease in the V_r. Errors are again determined through bootstrap re-sampling with a confidence level of 0.98.

2.2.6.2 Location of Merger

It is also worth noting where these objects merge with their host. Since the orbital properties are tied to the host system's potential and interactions with other subhalos, it is crucial to understand where objects merge with their host. If objects preferentially merge along an axis, it can indicate locations with a higher density of interactions and thus add additional heating to objects that merge along this location. This is seen from many studies of this effect, that find infalling subhalos merge along cosmic filaments (Tormen 1997; Knebe et al. 2004), and that the shape of the host system can align with the direction of recent mergers (Schindler 2000). Figure 2.9 plots the distribution of the location of infall in both an ellipsoidal and spherical definition. Here, θ is the angle between the location of infall and the largest axis of the ellipsoid that defines the host at the time of the merger. The merger's location is where the subhalo crosses the spherical or ellipsoidal boundary defined by the host system. Running a KS test for these shows they are consistent with each other, with a p-value of 0.43, which suggests the choice of boundary does not significantly influence the distribution of infall location.

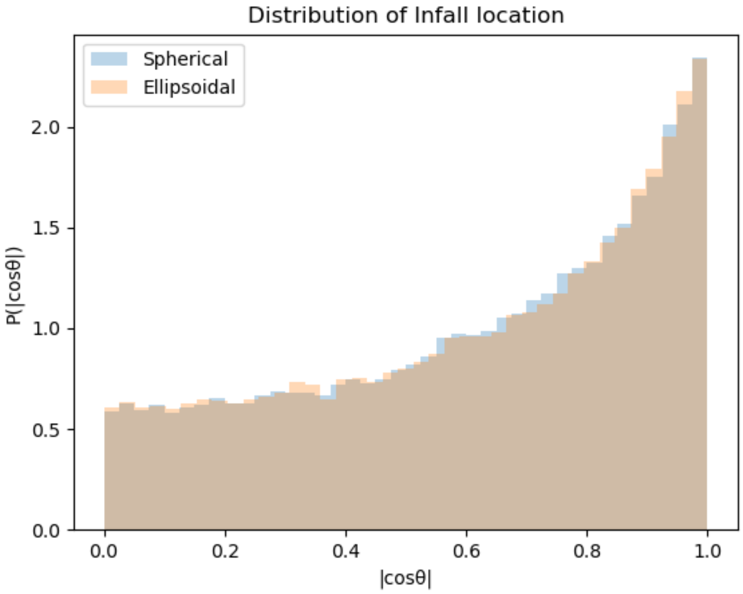

Figure 2.9: The distribution of infall locations with respect to the largest axes of the ellipsoid. In blue is the spherical boundary, and in orange is an ellipsoidal boundary. These distributions would be flat if orbits were isotropically distributed on the surface. Thus, there is a clear preference for orbits to merge along the largest axis of the ellipsoid.

2.3 Measured Pericentric Passage

The initial orbital evolution from infall to the pericentre is a complex process involving interactions between the subhalo and the host's matter distribution. Although the density profile of a halo can be modeled with a spherical or even triaxial potential, these do not capture the contributions from each particle or the interactions between nearby subhalos. In reality, the density is no longer smooth, static, or spherically symmetric, leading to an orbit that deviates from the ideal case. Although several studies have measured the correlation between the orbits of subhalos and their properties at infall (Tormen 1997; Khochfar & Burkert 2006), it is clear that many processes can act to scatter orbits from their original path.

In the simplest case, bulk changes to the potential can affect orbits in minor ways. Suppose the potential remains as a spherical NFW. In that case, changes in the host's mass, concentration, and radii during a subhalo's first orbit will still change the system's potential, thus deviating it from its initial path. These properties are expected to change during mergers and generally throughout the evolution of a halo. Similarly, in triaxial systems, the orientation of the axes of the potential can change. Even if host halos accrete matter slowly, their distribution is expected to change in response to their history.

This does not account for the effect of violent mergers common in the hierarchical model for structure formation. These events will cause significant, sudden changes to the system's potential. It can take several orbital periods before the system returns to a relaxed state. Thus, these violent events may also change the orbits of other infalling objects. These events may also introduce a secondary component to the potential for objects close to the infalling large satellite, as it is expected to remain as an individual structure for a period after the merger.

Objects also do not merge in isolation. Suppose objects merge in groups or even have an orbital path intersecting with that of another subhalo. In that case, their local potential is no longer well modeled by the host system alone. As the pericentre is understood to be the location of high tidal stripping, and quenching models use it as a benchmark for galaxy quenching, it is vital to understand whether these factors play an essential role in the location of the first pericentre. It is also important to determine if properties at infall of both the subhalo and host system are sufficient to model the first pericentre.

2.3.1 Predicted Infall Time Distribution

Before examining the distribution of pericentric passage, we must understand the expected results. Taking the orbital properties at infall and the halo properties of the host, I integrated the orbit forward, assuming the potential remains static. The infall parameters are introduced to the system assuming the Jiang et al. (2015) distribution infall distribution given by (2.20-2.23). This will be discussed further in 2.4. The potential used is a spherical NFW potential. We start with the infall parameters for each orbit and integrate the orbit forward a static potential. The radius is tracked after each step, with a cadence of $0.002T_{\rm circ}$. The radius and time of the pericenter are flagged as the moment of the first minima in the list radius value. Figure 2.10 shows the histogram for infall time and pericentric radii for the predicted catalog, compared to the simulations.

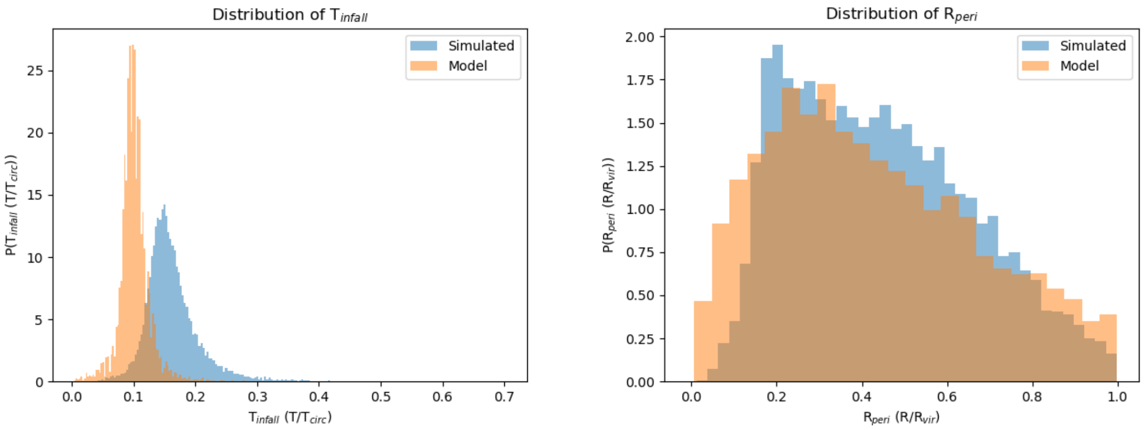

Figure 2.10: On the left is the infall time for both the simulated and model distribution of orbits. The model predicts a shorter infall time than the simulations. On the right is the same for pericentric radii. The distributions match more closely than the infall times, but the simulated distribution has fewer low radii orbits.

Figure 2.11 shows the dependence of infall time on its location in phase space. In this case, phase space is defined by circularity and total specific energy. There is a clear boundary in phase space for allowed orbits. This reflects the fact that for a given energy, the total velocity is set since the potential energy is constrained to that at the virial radius. However, an object must have a corresponding tangential velocity to have a certain circularity. Thus, an orbit will have a maximum allowed circularity at a fixed energy. Similarly, there is a restriction in circularity for objects with low energy. At the bottom of Figure 2.11, orbits will have nearly all their energy in potential energy, meaning they will have a very low velocity. Orbits in this region, thus, do not have enough kinetic energy to reach a circular orbit. The equation for the maximum circularity as a function of the infall energy, $c_{\text{max}}(E_0)$, is given below:

$$c_{\text{max}}(E_0) = \frac{R_{\text{vir}}\sqrt{2(E_0 - \Phi(R_{\text{vir}}))}}{L_{\text{circ}}(E_0)} \tag{2.11}$$

where $\Phi(r)$ is the potential at a radius r, and $L_{\text{circ}}(E_0)$ is the angular momentum of a circular orbit with energy E_0. The full derivation is given in A.2.

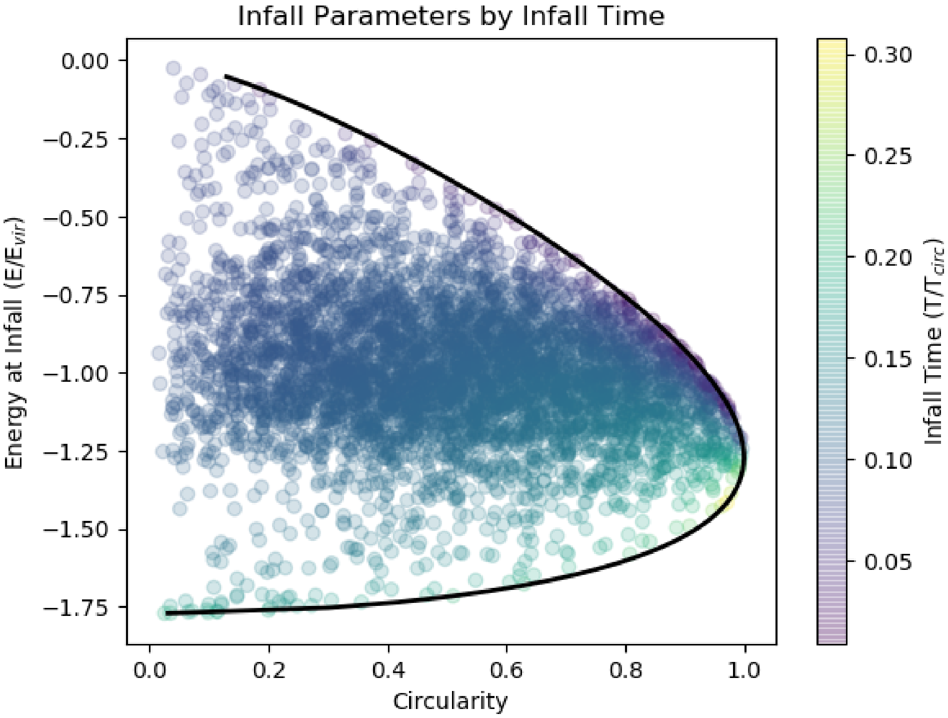

Figure 2.11: The distribution of infall time plotted in phase space. Each of the 5000 points results from a different orbit forward from the virial radius until the pericenter. The distribution of infall parameters is taken from Jiang et al. (2015).

Infall time is dependent on the energy at infall and the circularity. More negative energy suggests the object has little kinetic energy. This dependence reflects that objects that merge with low velocities take longer to increase in speed and reach pericentre. There is also a slight dependence on circularity in that orbits with a higher circularity reach pericentre sooner. Figure 2.12 shows these relationships for the simulations. Despite following a similar trend, these relations have a clear scatter. This is expected, as the conditions used for predictions are the ideal case. Similarly, the boundary is consistent with that found from 2.11. Since the boundary depends on the system's potential, Φ, the lower plots in Figure 2.12 split the infalling distribution into varying ranges of c_{NFW} values.

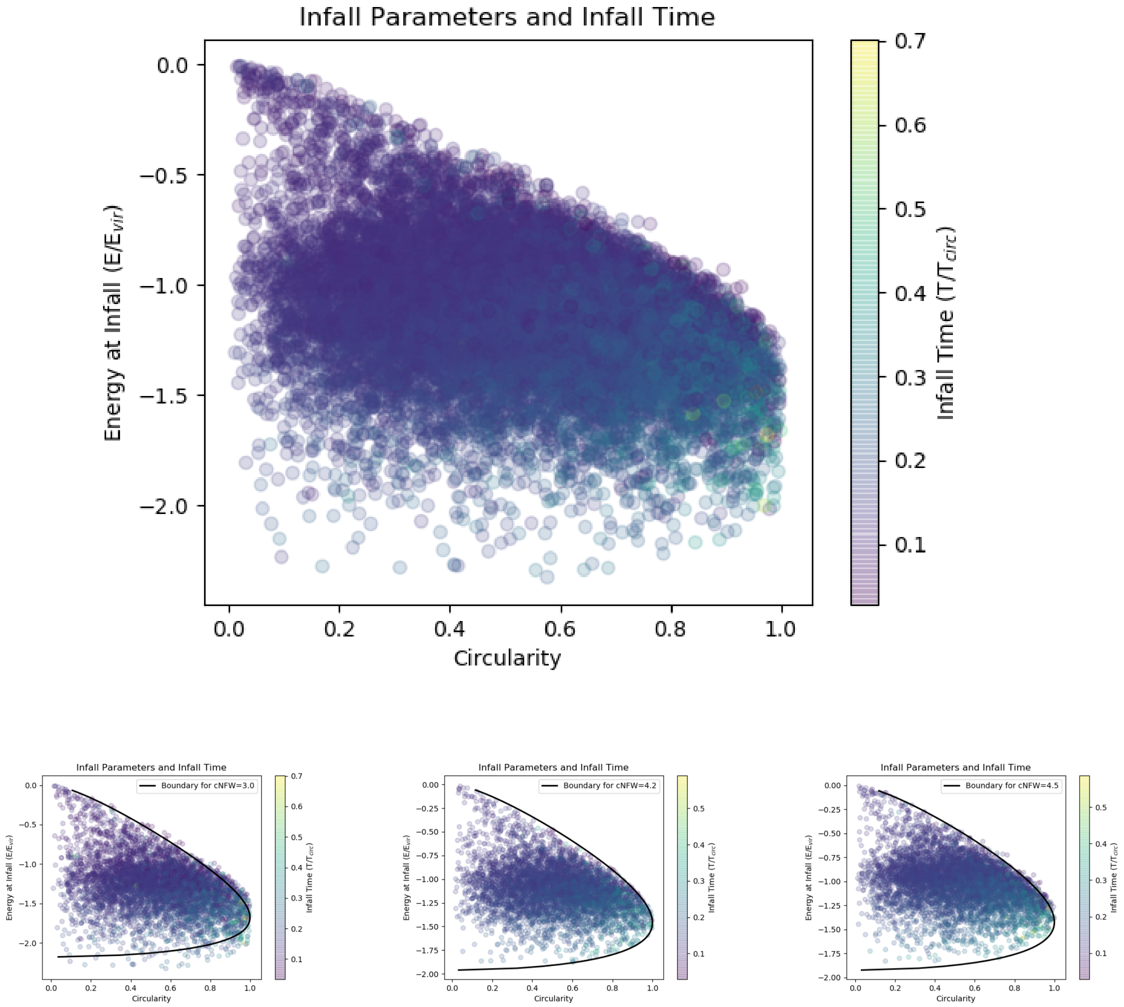

Figure 2.12: The same as figure 2.10, but for subhalo orbits taken directly from the simulations. Above is the entire population of subhalo orbits. Below is the same, but split into the populations that merge during their host's evolution with different concentration parameters. From left to right, the concentration parameter of the host is cNFW<3.9, 3.9<cNFW<4.5, 4.5<cNFW. The expected boundary is recovered after these separations.

2.3.2 Comparing Infall Times

I use the results from the orbital catalog to compare the expected and simulated infall time. In Figure 2.13, I plot the predicted infall time against that found by the simulation for each orbit in the catalog. If predictions are correct, all points should align with the line y=x, shown in black. The scatter about this line should indicate the level to which these orbits are heated during their first infall. Orbits below this line are expected to have been pushed to the pericentre sooner than expected. This population either falls faster into the host than expected or has a pericentre at a larger radius than predicted. Conversely, objects above this line take longer to reach their pericentre than expected. Thus, they are kicked to an orbit with a pericentre at a lower radius - having a longer distance to travel - or are slowed down by some mechanism.

The figure shows most orbits lie very close to the line y=x, with scatter around the point. For each orbit, I calculated $T_{\text{diff}} = T_{\text{predicted}} - T_{\text{infall}}$. These values are scaled to T_{circ}. The distribution of these values is shown in the right plot of Figure 2.13. It is found that 95 percent of the distribution lies between 0.05 and -0.14. The average value is -0.01. This indicates a preference for orbits to take slightly longer to reach the pericentre than expected.

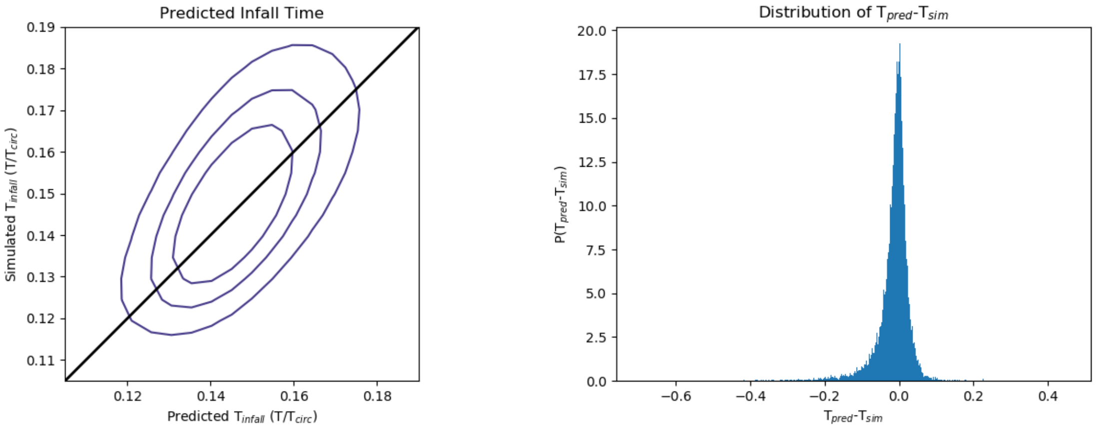

Figure 2.13: Taking the measured infall time of each subhalo from the simulations directly and the time predicted by integrating the orbit forward assuming a static, spherical NFW potential, we compare the predicted to the simulated results. Above: Simulated Infall time vs Expected infall. Note that the contours correspond to the fraction of points outside the boundary. These correspond to: [0.32,0.5,0.68]. To the right is the distribution of T_{diff}, which indicates a slight preference for simulated orbits to take longer to reach pericenter than predicted.

2.3.3 Comparing Pericentric Radii

For pericentric radii, we compare the predicted to simulated radii by generating Figure 2.14. As with Figure 2.13, the ideal case should have all points along the line y=x. Points above this line are pushed to orbits that reach pericentre at radii larger than expected. This should correspond to gaining angular momentum. Lower than this line, orbits are expected to have lost angular momentum and fall further into the host than predicted from their infall properties. Similarly, this would be explained by an increase in the host mass, thus increasing the force inward.

To compare these results $R_{\mathrm{diff}} = R_{\mathrm{predicted}} - R_{\mathrm{peri}}$ is calculated. It is found that 95 percent of the population lies between -0.15 and 0.34, with an average of 0.05. This indicates that pericentric radii are around the expected value but tend to be pushed to orbits with smaller pericentric radii. This may indicate an increase in the host mass, increasing the radial force exerted on the object.

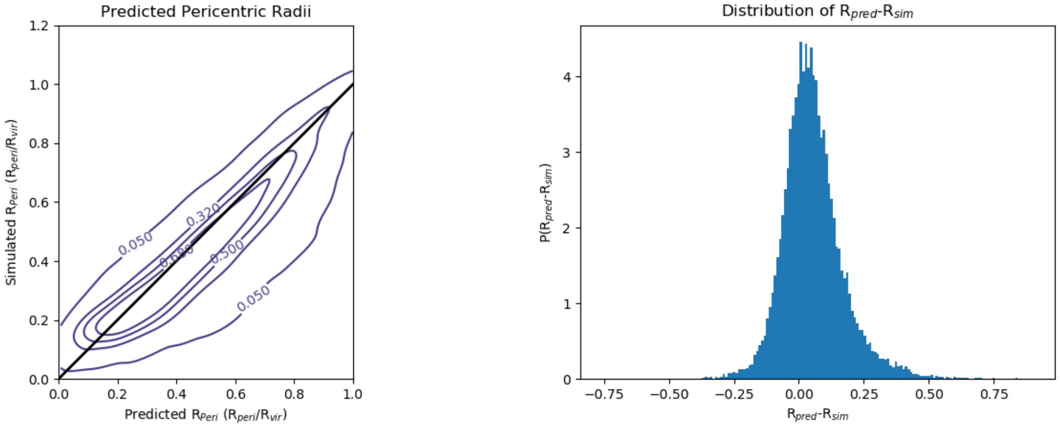

Figure 2.14: Left: Simulated Pericentric Radii vs Expected. Note that values in the contours display the fraction of points outside their bounds. The contours are: [0.05,0.32,0.5,0.68]. Right: Distribution of R_{diff}. These are generated in the same way as 2.13. Both plots show predictions overestimate pericentric radii.

2.3.4 Discussion

Although the results from above show a general agreement between pericentric passage predicted at infall and that simulated through the n-body simulation, some orbits do not follow their expected path. When does this happen, and why would this occur? This can be examined by determining the relationship between an object's pericentric radii and infall time when either is inaccurately measured. Figure 2.15 plots $\log_{10} R_{\mathrm{sim}}/R_{\mathrm{pred}}$ against $\log_{10} T_{\mathrm{sim}}/T_{\mathrm{pred}}$. As expected, there is a cluster centered close to the origin. This indicates where the simulated radii and infall time are well predicted.

However, a significant number of objects also lie far from the origin. To quantify this, I track the population of orbits that deviate from their predicted pericentric radius or infall time by 25 percent. This population of orbits will be called 'kicked'. This population corresponds to 9322 out of the 18074 orbits tracked. I define the kicked population as ones such that one of the following inequalities holds.

$$|T_{\mathrm{ratio}} - 1| > 0.25 \tag{2.12}$$

$$|R_{\mathrm{ratio}} - 1| > 0.25 \tag{2.13}$$

$$\tag{2.14}$$

where T_{ratio}=$T_{\mathrm{sim}}/T_{\mathrm{pred}}$ and R_{ratio}= $R_{\mathrm{sim}}/R_{\mathrm{pred}}$.

This definition naturally splits the population into several categories. Orbits that take longer to reach pericentre and have smaller than expected pericentric radii will be called the 'fallen' population. These orbits are simply kicked to ones that fall deeper into the host system. As their pericentric radii are now further into the system, they are expected to take longer to reach it, as their new orbit must travel further to reach the pericentre. This accounts for 40% of the kicked population.

Next, the population that reaches pericentre sooner than expected and at radii larger than expected will be called the 'boosted' population. These objects are simply pushed to orbits with a pericentre at larger radii and thus require less time to reach them. The fallen and boosted populations are kicked to a different orbit, but their motion follows the expected result. 15% of the kicked population is boosted.

There are also two other regions that should push the orbit to completely different orbits. The lower left quadrant corresponds to a population of orbits that fall further into the potential and take a shorter time to reach the pericentre. I will call this the ’pulled’ population. Thus, there must be a mechanism that pulls these orbits to the inner regions of the halo. The population of pulled orbits corresponds to 25% of the total number of kicked objects. The other population, accounting for 19%, reaches the pericentre further out than expected, taking longer than expected. This ’bounced’ population must have slowed down and have been kicked onto a much more circular orbit.

These values show that the largest group is the fall orbits, which take longer to reach and fall farther into the potential. The fallen population explains the observed results from Figures 2.13 and 2.14, which show a preference for objects to take longer to reach pericentre and to have smaller pericentric radii. These results, however, depend on the integration method used to determine the motion of the orbit. Since it relies heavily on the parameters of the host, which can vary drastically between snapshots, this may not be an accurate representation of the system at the time of the merger.

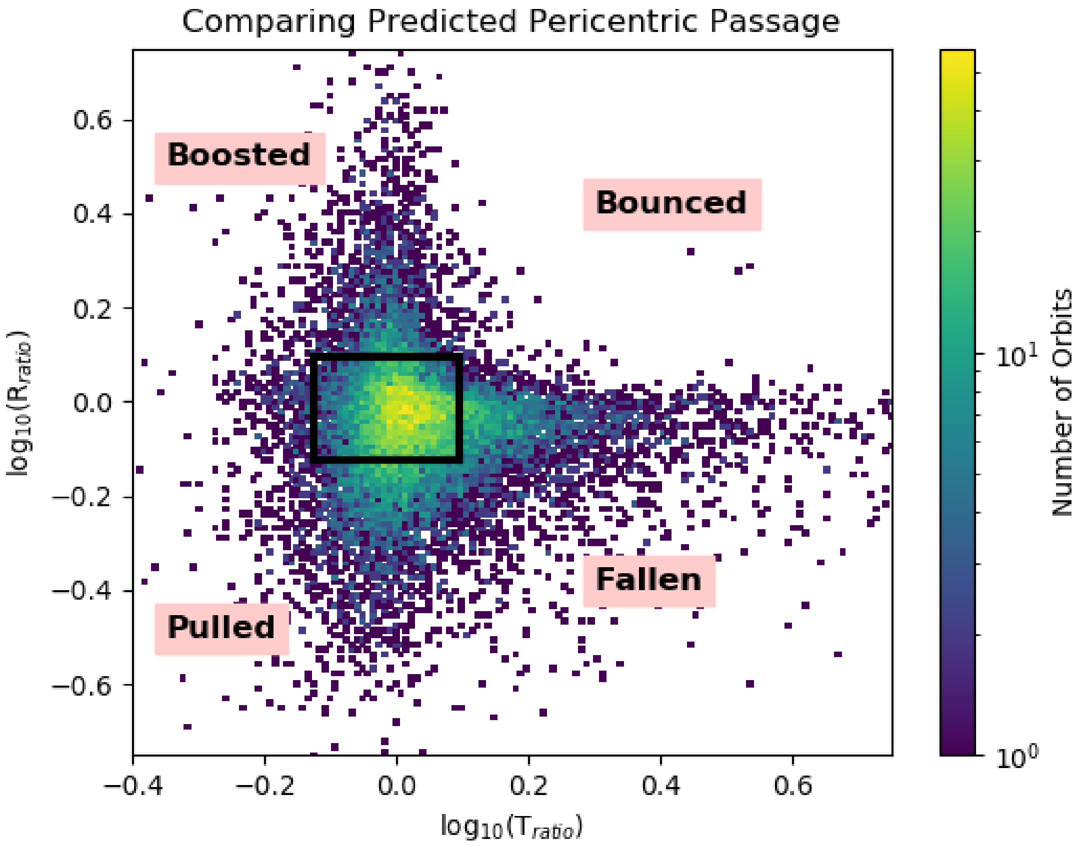

Figure 2.15: Plotted is the distribution of orbits in the R_{ratio}- T_{ratio} plane. Regions outside the black box are considered kicked. The quadrants are labeled by their distinction, as described in the text.

2.3.4.1 Kicked Fraction

To better understand when orbits are kicked out of their original orbit, we can first examine the nature of the infall. Figure 2.16 shows a kicked orbit's predicted and simulated orbital path. Since the simulated path takes longer to reach the pericenter and reaches a radius smaller than predicted, this subhalo is in the 'fallen' category. The orbit is shown to deviate significantly from the predicted path.

We can also compare the fraction of kicked orbits to the properties of the host. Since it is expected that interactions between other halos will cause this effect, I again use the dynamical state of the host 2.9. Figure 2.17 shows the evolution of the dynamical state and kicked fraction for a sample halo from $0 < z < 2$. It is clear that both the dynamical state and kicked fraction change during certain epochs of the host's evolution. Also, the kicked fraction increases during non-relaxed times (low dynamical state). This suggests that the mechanism that prevents accurate predictions of an orbit is tied to the evolution of the host and can last for extended periods.

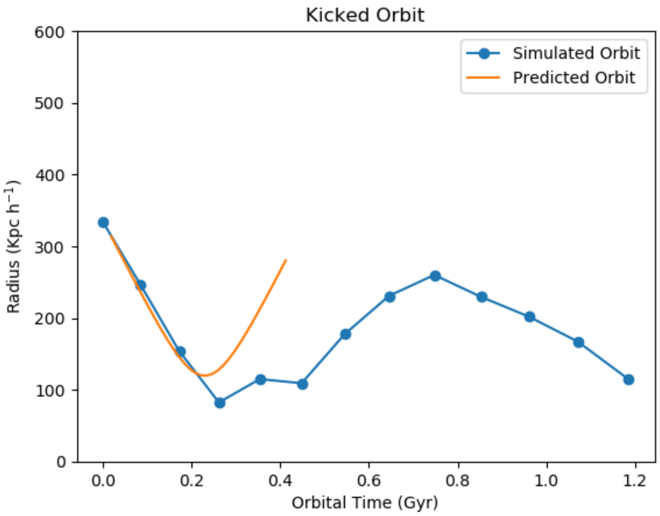

Figure 2.16: Shown here is a sample orbit of an object identified as being kicked. There is a clear change in the orbital trajectory. This particular orbit is of the fallen population and thus reaches the pericenter later and at a smaller radius than predicted.

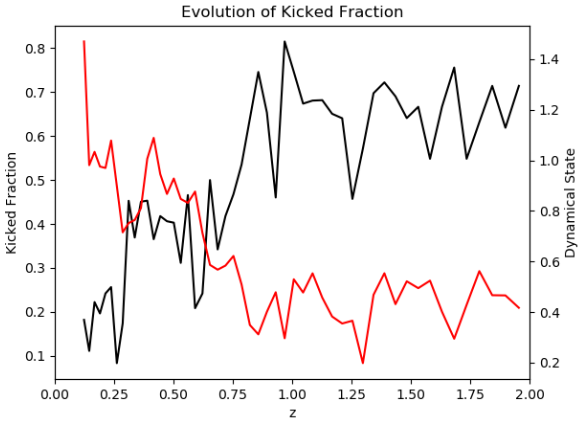

Figure 2.17: The kicked fraction, with respect to redshift for a single host. In black is the kicked fraction, and in red is the dynamical state. During times of low dynamical state, the kicked fraction is increased.

This trend occurs for all three hosts used in this work. To show this more clearly, a plot of the dynamical state vs. kicked fraction is shown in Figure 2.18. This shows a general trend of relaxed systems having a smaller percentage of the kicked population.

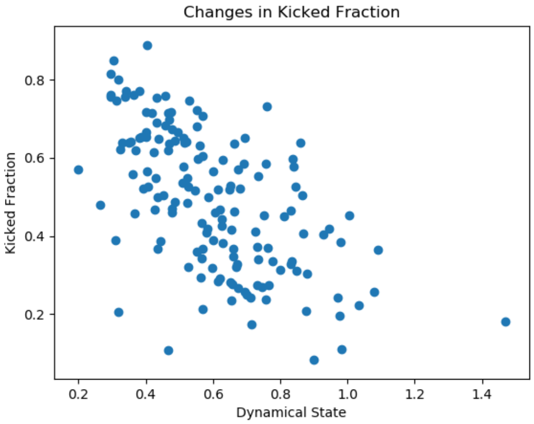

Figure 2.18: Taking the orbits of merging subhalos during each snapshot, I track the dynamical state at the time of the merger. Plotting the kicked fraction vs. the dynamical state of the host, there is a clear trend for a higher fraction of kicked orbits during times with low dynamical state.

2.3.5 Infall Location

As shown in 2.2, infall parameters are weakly related to the location of the merger. Particularly, the objects that merge along the largest axes of the ellipsoid infall with slightly less radial orbits. This should have the effect of increasing the pericentric radii of orbits that merge along this axis. Similarly, this should put these objects on more circular orbits, allowing them to reach pericentre sooner. Figure 2.19 below plots the average infall time and pericentric radii against their infall location. We find no significant dependencies on pericentric passage according to the location of their merger. Since properties at the time of infall are shown to influence pericentric passage, and from Figure 2.8, we see infall parameters have little dependence on the location of the merger, this is reasonable to expect.

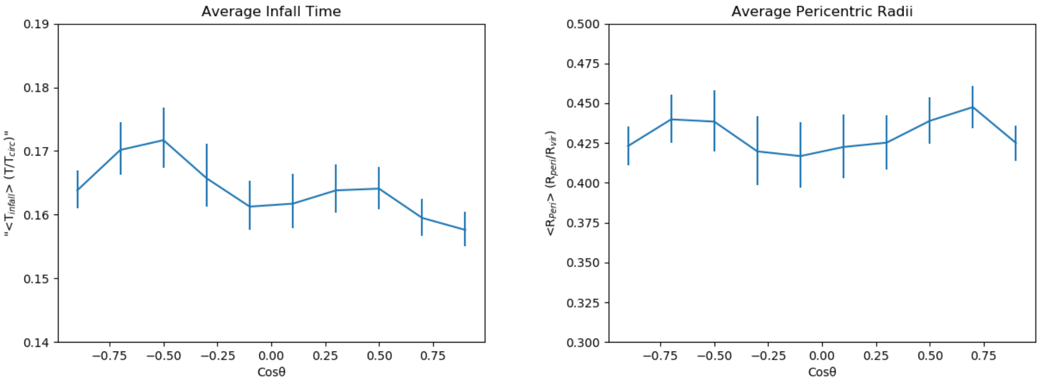

Figure 2.19: Average infall time and pericentric radii in bins of cos θ, where θ corresponds to the angular difference between the infall location, and the largest axis of the halo if modeled by an ellipsoid. There are no clear dependencies between these values.

2.4 Evolution of Orbital Population

Since the population of orbits within a cluster can provide information about the properties of the host system, it is important to understand how orbits change throughout the evolution of the host. During major mergers especially, it is reasonable to expect orbits to be heated in response to the sudden mass influx and through shock heating and close gravitational interactions with other subhalos.

By examining the three simulations used in this study, the bulk changes to the population of subhalos can be related to the MAH of the host. During sudden significant mass change, a major merger is expected to occur, causing a significant change in existing orbits. The interactions between pre-existing orbits and the influx of new material can cause this. To examine the change in existing orbits, the average energy, angular momentum, and velocity magnitude for all subhalos within a host system is plotted vs. redshift. To avoid objects identified as being merged but quickly lost in the merger tree, I only consider objects that survive until the final snapshot. This is shown in the top portion of Figure 2.21. The energy, angular momentum, and velocity are scaled to their characteristic values at z=0 (equations 1.22-1.24). Figure 2.21 shows a steady decrease in the average energy of the system and an overall increase in angular momentum and velocity. The steady decrease in energy is simply due to increased host mass, increasing the potential energy of all subhalo orbits. However, the increase in angular momentum and velocity indicates a steady heating of the system as it evolves.

However, this change in orbital parameters may be due to the introduction of new subhalos, which increase the average infall velocity and angular momentum. This can be seen clearly through equations 1.22-1.24, where the characteristic value for each increases as mass increases. This is not the desired effect, as the goal is to examine how orbital properties for individual orbits change according to the MAH. To address this, the bottom plots in Figure 2.21 only contain information about halos that merge before z=2 and still survive to the final snapshot. Even with these cuts, the same change in orbital properties is observed. This indicates that both angular momentum and velocity change in response to the MAH of the host.

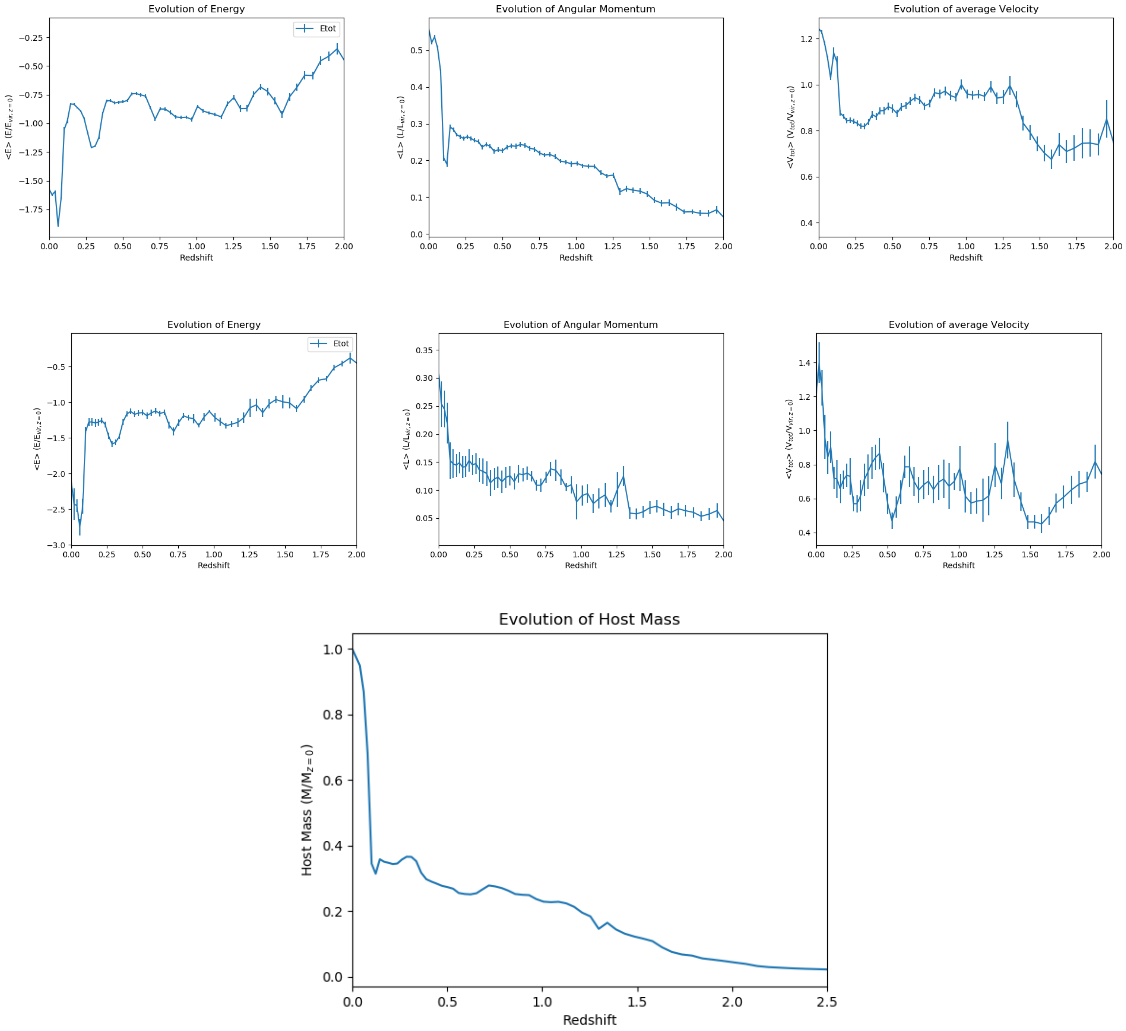

Figure 2.21: The changes in average orbital parameters for a sample host system. The leftmost column shows the evolution of average energy. The middle column is the average angular momentum, and the rightmost column is the average velocity. Above are all surviving subhalos at z=0, while the bottom row includes only the subhalos that merge in the interval $z > 2$. These figures show that these parameters change in response to the MAH. At the bottom, I also include the mass of the host across this time.

Although detailed information about the host and its subhalos, such as that available in simulations, are sufficient to track changes to the population of orbits, it would be ideal to have a more accurate method. If a model can be created using only bulk properties of the host, such as its MAH, then toy models can use this to generate mock catalogs of orbits for clusters without the need for simulations. In this section, I examine the evolution of orbital properties of subhalos within the host system. I also discuss the validity of a relatively simple orbital evolution model and whether the MAH is sufficient to model the changes in subhalo orbits.

2.4.1 Orbital Population

A data set of subhalo orbital properties across the evolution of the host must be generated to verify the model's validity for orbital evolution. At each output of the simulation, I track the position and velocity of each subhalo of the host with respect to the frame of the host center. Tracking only the output ensures that orbital properties are determined solely from the distribution of particles rather than interpolating between snapshots. Each subhalo is tracked starting from the first time it is identified as a subhalo of their host halo. At the same time, the R_{vir}, M_{vir}, and the NFW concentration parameter of the host are found. The specific energy can be calculated from the subhalo position and velocity. Similarly, the specific angular momentum is also calculated in the same step. These are then each scaled by the host system's characteristic energy and angular momentum at the z=0 snapshot. Energy and angular momentum are used to characterize each orbit.

$$E_{\mathrm{tot}} = \frac{v_{\mathrm{sat}}^2}{2} - \phi_{\mathrm{NFW}}(r_{\mathrm{sat}}, M_{\mathrm{vir}}, R_{\mathrm{vir}}, c) \tag{2.15}$$

$$L = \vec{r} \times \vec{v} \tag{2.16}$$

For each subhalo, these are saved for each snapshot the subhalo is found. I can then track the evolution of these parameters and test whether they can be accurately modeled. Across all three host halos, we have a total of ∼14000 surviving subhalos.

2.4.2 Evolution Between Snapshots

To accurately model the evolution of orbital parameters according to the MAH, it is necessary to understand how these parameters change between simulation outputs. As noted before, there are two factors that need to be accounted for: the scatter due to changes in orbital parameters and the changes in the mass of the system, leading to a change in the potential energy of a subhalo. This can be determined by examining how these parameters change between snapshots. From Figure 2.22, which plots the initial energy against the final energy between subsequent snapshots, orbital parameters appear to cluster around the line y=x, with a slight scatter. As expected, there are also times when the entire population seems to shift in value. This reflects a change in the mass of the system.

To model how these parameters change between snapshots, the changes in orbital parameters are fit to equations 2.17 and 2.18. In this case, g is the scattering term, modeled as a Gaussian distribution centered around 0, defined by σ, which is the standard deviation determined from the line fit to the data. To fit this, I minimize χ^2. E_n and E_{n+1} correspond to the energy at a given snapshot and the following snapshot. The same convention is used for L. The slope (m) and intercept (b) values are determined from the linear fit.

$$E_{n+1} = mE_n + b + g_E \tag{2.17}$$

$$L_{n+1} = mL_n + b + g_L \tag{2.18}$$

$$g(\sigma) = \frac{1}{\sigma\sqrt{2\pi}} \exp\left(-\frac{1}{2}\left(\frac{x}{\sigma}\right)^2\right) \tag{2.19}$$

The scatter term is chosen to be a Gaussian both due to the simplicity of using only one fit parameter and because it is shown to capture the nature of the scatter terms. Figure 2.22 shows the energy and angular momentum changes between two subsequent snapshots. The line corresponds to the line fit to the data. The residuals are also plotted, with the fit Gaussian overplotted. Although a KS test does not show these are consistent (p-value of less than 0.002), it appears to match the residuals reasonably.

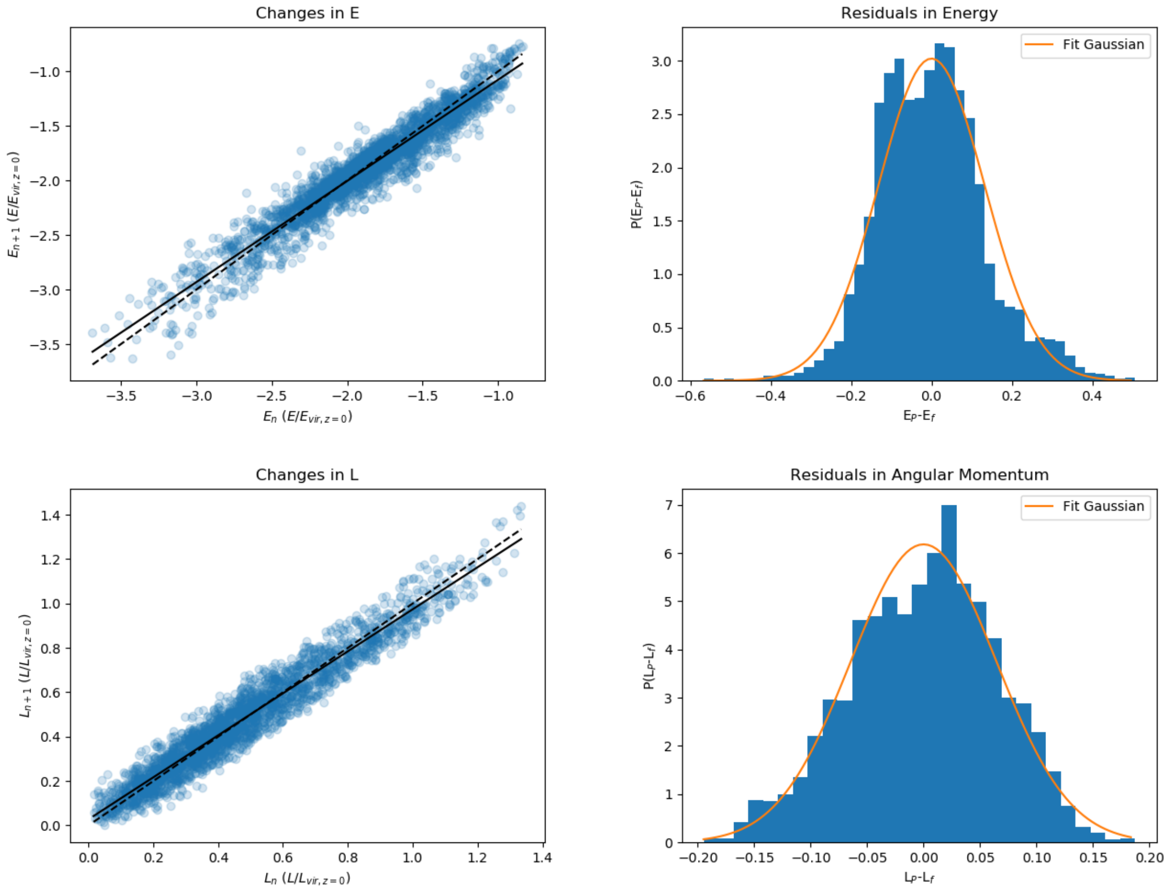

Figure 2.22: Above: an example of analyzing two subsequent snapshots from a single host. On the left is each constituent subhalo's initial vs. final energy. The solid black line corresponds to the fit line for the system, while the dashed black line shows the line y=x. On the right are the residuals to the fit line. Show in orange is the fit Gaussian distribution. Below is the same, but for angular momentum. In both cases, the initial and final values lie around the expected line, with a scatter that matches closely to a Gaussian distribution.

In an ideal case, g(n)=0, m=1, and b=0. In this case, the evolution of energy and angular momentum are conserved between each snapshot. This corresponds to a static and spherically symmetric host halo. Since this is an unrealistic model for halo evolution, each of these parameters is expected to deviate from this ideal case. These cases will be discussed in section 2.4.3.

2.4.3 Final Model

Finally, these considerations can be incorporated into a model to test whether this view can track the changes in orbital properties for host systems. Since this model requires information between each snapshot, this will need to be done individually for each host halo. This semi-analytic model aims to take the MAH of a host, accurately inject orbits, and evolve the energy and angular momentum of each. Thus, it should first accurately describe the parameters at the time of infall.

We follow Jiang et al. (2015) and fit the distribution of infall velocity (scaled by the virial velocity) to a Voigt profile:

$$P_\nu(x;\sigma,\gamma,\mu) = \int_{-\infty}^{+\infty} P_G(x';\sigma,\mu) P_L(x-x';\gamma)dx' \tag{2.20}$$

$$\text{where } P_L(x;\gamma) \equiv \frac{\gamma}{\pi(x^2+\gamma^2)} \tag{2.21}$$

$$\text{and } P_G(x;\sigma,mu) \equiv \frac{1}{\sqrt{2\pi}\sigma} \exp\left(\frac{-(x-\mu)^2}{2\sigma^2}\right) \tag{2.22}$$

We also use their fit for the infalling radial velocity, scaled by the total velocity, by an exponential:

$$P(\nu_r/\nu) = A\left(\exp\left(\frac{B\nu_r}{\nu}\right) - 1\right) \tag{2.23}$$

To match the simulations used in this work, I fit new parameters for the three simulations by maximizing the likelihood $\mathcal{L} = \Pi_i P_\nu(x_i;\sigma,\gamma,\mu)$, where i runs over all infall orbits. Table 2.1 shows the fit values. Host mass and mass ratio ranges without sufficient data

(<100) are not included. Similarly, mass ratios below 10^{-5} are not used, as the distribution of infall velocities cannot be fit in this form. The final distribution is shown in Figure 2.23, which also shows the distribution from orbits from the simulations. Although a KS test does not show these distributions are consistent with each other, their final distribution is reasonably similar for this work. I use the parameters from Jiang et al. (see table 2 from Jiang et al. (2015)) for the distribution of radial velocity, as it matches my distribution, shown in 2.23. A KS test confirms this, with a p-value of 0.6.

M_{host} ($M_{\odot}h^{-1}$)	M_{sat}/M_{host}	γ	σ	μ
10^{12}	$10^{-5} - 10^{-4}$	0.005640 ± 0.000060	0.285587 ± 0.000252	1.207235 ± 0.000060
10^{12}	$10^{-4} - 0.005$	0.004718 ± 0.000006	0.262540 ± 0.000024	1.263036 ± 0.000005
10^{13}	$10^{-6} - 10^{-5}$	0.029766 ± 0.000490	0.201715 ± 0.000782	1.267787 ± 0.000139
10^{13}	$10^{-5} - 10^{-4}$	0.028047 ± 0.000312	0.202807 ± 0.000230	1.291578 ± 0.000069
10^{13}	$10^{-4} - 0.005$	0.029121 ± 0.000017	0.198714 ± 0.000029	1.285265 ± 0.000004
10^{14}	$10^{-6} - 10^{-5}$	0.045032 ± 0.000027	0.077459 ± 0.000010	1.296986 ± 0.000026
10^{14}	$10^{-5} - 10^{-4}$	0.013942 ± 0.000009	0.110674 ± 0.000016	1.301062 ± 0.000037

Table 2.1: Parameters of the fitted infall orbital parameters equations 2.20-2.23 in bins of host halo mass and mass ratio at the time of infall. These are the maximum likelihood fits generated from all infalling subhalos across all hosts in each bin.

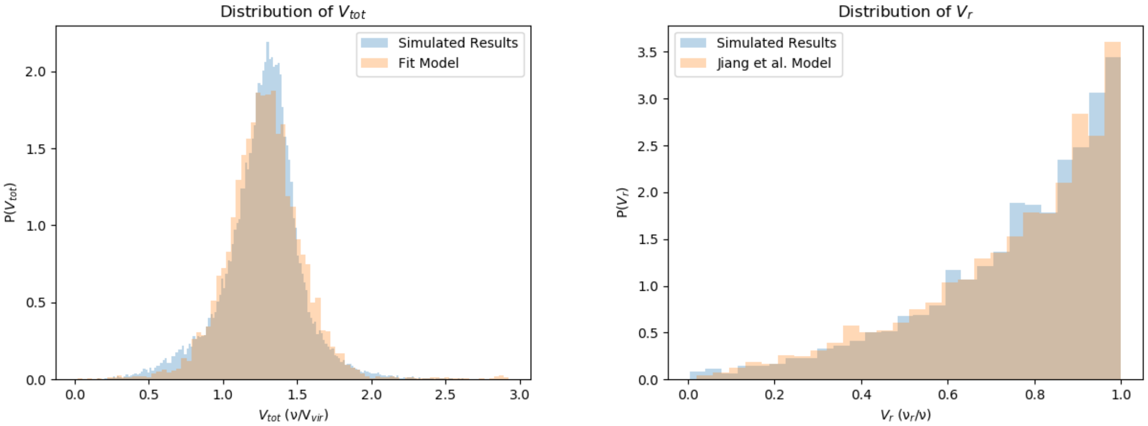

Figure 2.23: Comparisons between the distribution of infall parameters taken directly from the simulations (blue) and when drawn from the fitted distributions (orange). These were generated by drawing from the distribution for every infalling subhalo, with cuts described in the text. The left is for the total velocity, and the right is for the radial component of the velocity. The fitted parameters for the infall velocities are that of 2.1, and the radial parameters are taken from Jiang et al. (2015).

Deciding when to introduce a new orbit can be difficult to properly incorporate since the mass and number of infalling satellites are tied heavily to its MAH. Thus, instead of generating a fictitious MAH for each host, an orbit is added into the system for each infalling subhalo in the simulation. This should give a representative distribution of infalling orbits.

Finally, the evolution of each orbit between subsequent snapshots must be modeled appropriately. Following equations 2.17 and 2.18, and the determined values for m, b, and g, E_n is transformed to E_{n+1}. There is also a set limit on E and L at all snapshots. The maximum energy is taken to be 0. If this model pushes an orbit to have positive energy, these objects will be considered ejected from the system. Similarly, the minimum value for these can be taken to be that of a stationary (in the frame of the host) object at the virial radius. We will use the NFW potential of the host system at the time of the merger to determine this. Similarly, the maximum angular momentum is that of a circular orbit at the virial radius, and its minimum is 0.

$$E_{\rm max} = U = -\frac{GM_{\rm vir}}{R_{\rm vir}} \tag{2.24}$$

Following these prescriptions for each subhalo, we obtain the following results. First, Figure 2.25 shows the final distributions of energy and angular momentum. Across all host systems, these appear to be consistent. From this result alone, it is unclear whether the model accurately captures the evolution of orbits, as the population may have recently accreted a large number of subhalos. The match in the final distribution may instead indicate the distribution of infall parameters that match the simulation - which it is expected to do.

Thus, in Figure 2.24, the initial vs. final energy and angular momentum for the surviving population are plotted. The colors in these plots indicate the infall redshift. Similarly, Figure 2.25 shows a histogram of the final energy vs. infall redshift. It is evident that objects that merge at $0.1 < z < 1$ deviate significantly between the model and simulation. However, at higher redshifts $z > 1.2$, the distribution seems to match more closely. The intermediate period encompasses a time when many subhalos merge with the host but quickly dissipate. Although the model correctly introduces orbits, it does not accurately remove them from the population - on short time frames. The subhalos that merge at higher redshifts seem to follow the expected trend.

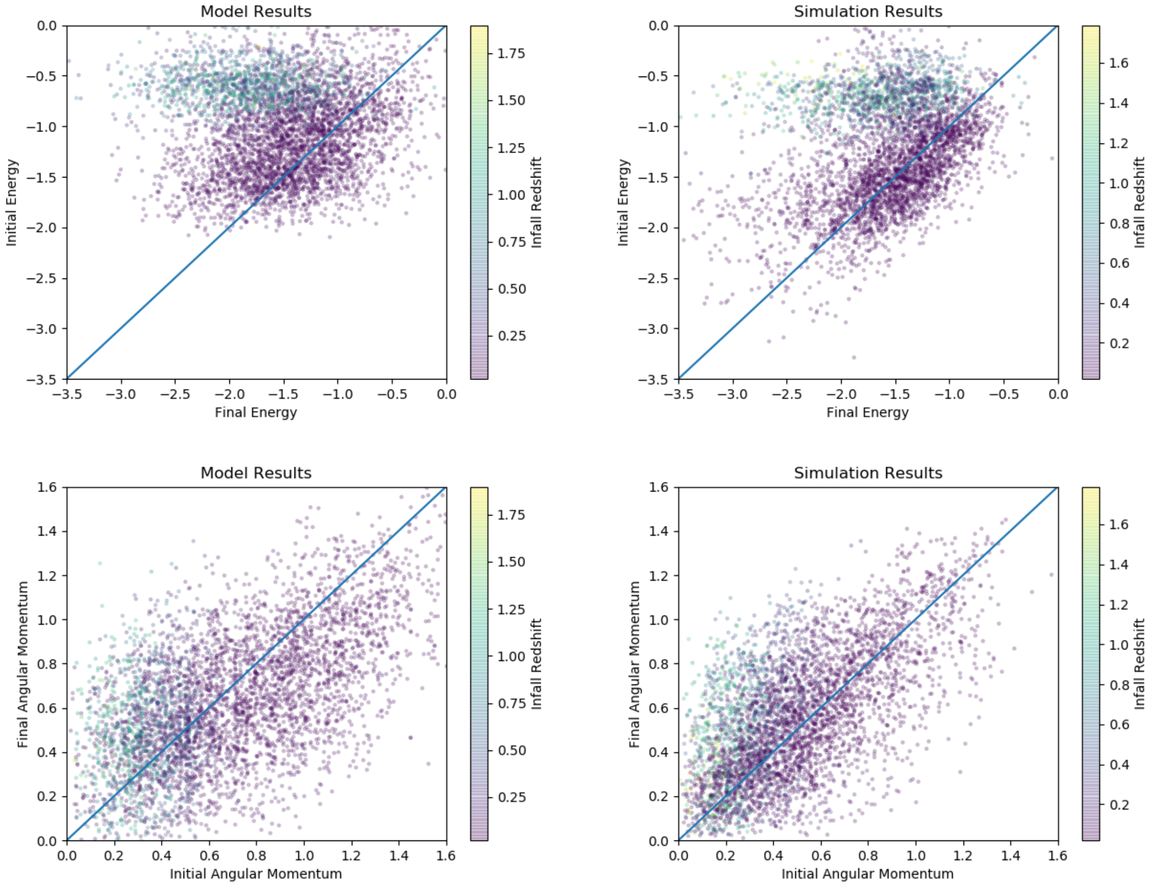

Figure 2.24: Top row shows each subhalo's initial vs. final energies that survive until the final snapshot. The color indicates the infall redshift. The bottom is the same but for angular momentum. The left column shows the model results and the right is from the simulations. The blue line shows y=x, indicating the expected result if orbital parameters are conserved.

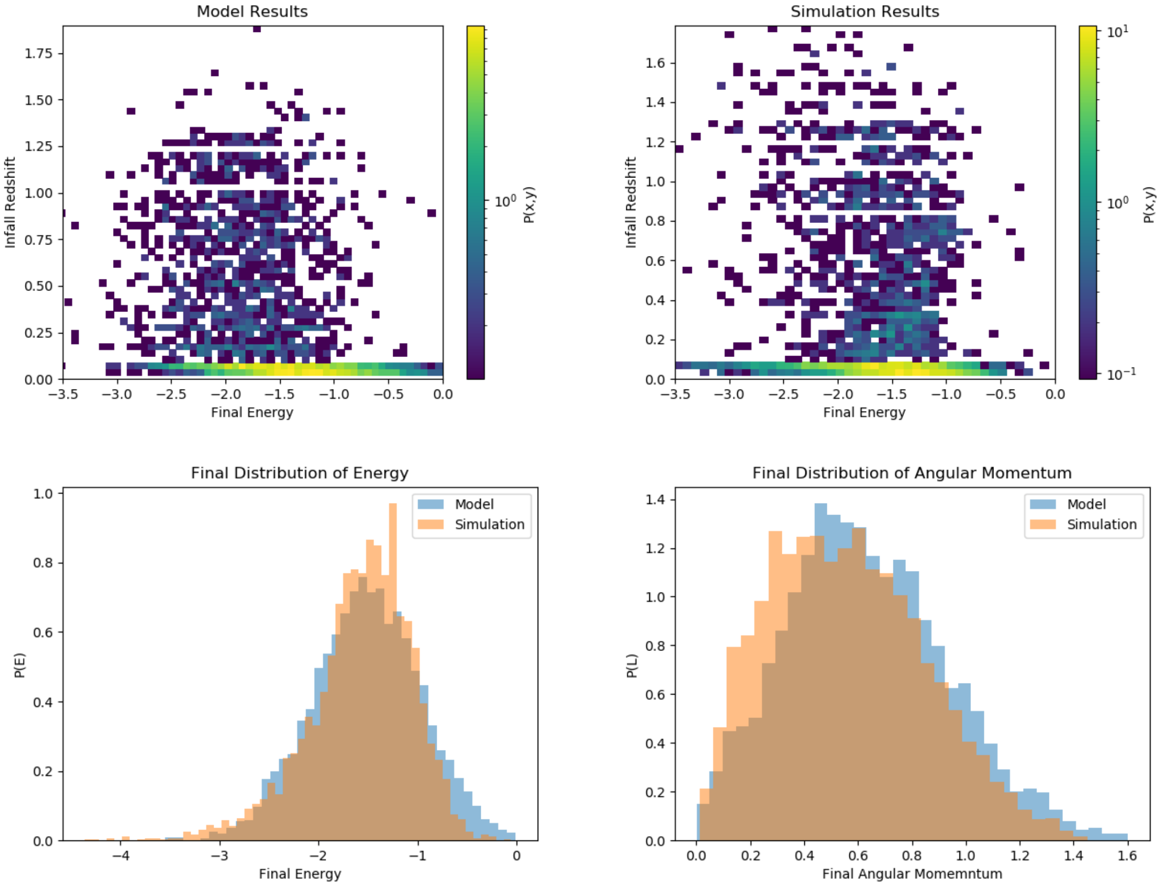

Figure 2.25: The top row displays a 2D histogram of final energy vs. Infall redshift. On the left is the model, and on the right is the simulation results. The bottom row shows the final histogram for energy (left) and angular momentum (right) for both the model (blue) and the simulation (blue).

2.4.3.1 Determining the Intercept

In the case of a non-zero intercept in the linear fit between initial and final E or L, it is important to examine each individually. Starting with energy, the intercept has a very clear physical meaning. It corresponds to changes in the mass of the system. If the mass of the host changes between snapshots, the potential energy of orbiting objects is expected to change, even if little is changing about the orbital properties. This artificial change in potential energy thus shifts the position of all objects. Thus, the intercept value should scale with the changes in mass between snapshots. Figure 2.26 shows that the intercept value decreases as the change in mass increases. Note that this effect can also introduce a slope to the fit, as discussed below.

For angular momentum, these are expected to be relatively robust against mass changes. A baseline change in L is expected only if each orbit is heated similarly. Although this may be possible, this can also come from changes to the position or velocity of the host system. This would change the values of each orbit's relative position and velocity, thus affecting all of them. Figure 2.26 plots the intercept against the dynamical state. It is again clear that there is an increase in the intercept at periods of low dynamical state. This supports the view that changes in the intercept result from mergers.

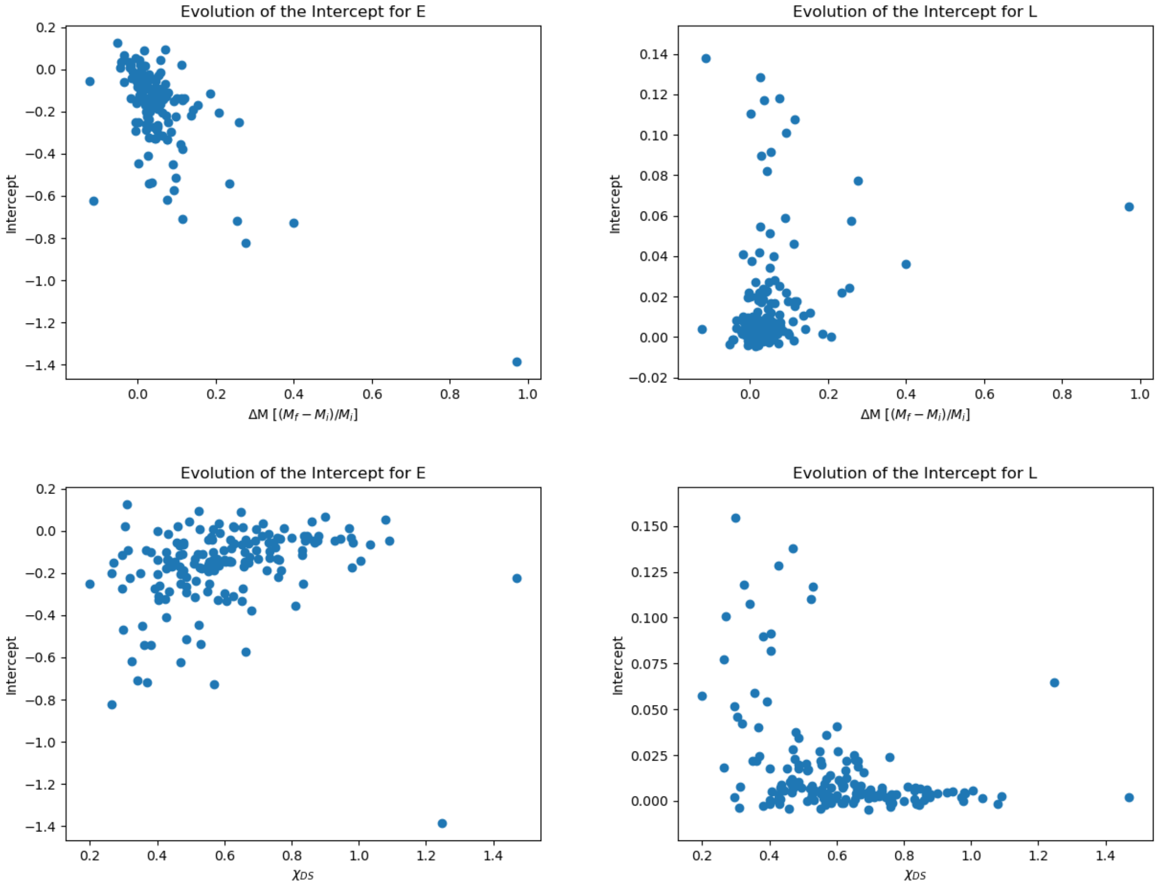

Figure 2.26: Above shows the fit value for intercept plotted against the relative change in mass. Below plots the intercept against the dynamical state. The left column is for energy, and the right column is for angular momentum.

2.4.3.2 Determining the Slope

The slope, m, in these equations, probes a unique aspect of the system between snapshots. In these equations, it corresponds to a difference in the change in orbital properties depending on the value of these orbital properties. The case of non-zero intercept and scatter term, $m \neq 1$ indicates the evolution of E or L solely depends on its magnitude. This can have some physical interpretation. For energy, objects more loosely bound to the system are expected to be on the system's outskirts and are more susceptible to the effects of infalling objects. Depending on an orbit's location, it may be influenced by a specific event. Also, changes in the potential do affect each orbit differently. For example, in the simplest Keplerian example $\Phi(r) \propto M/r$, doubling the mass of the host will simply double the potential energy of each orbit. This would cause the intercept to be non-zero and introduce a different slope. This is because the objects with a large potential energy will gain more than those with a smaller. In this picture, the slope deviations should correspond to mass deviations between snapshots. Similarly, objects with significant angular momentum are expected to have more circular orbits and a larger radius. This would again suggest that, on average, they would occupy different regions within the halo.

It is important to note that the slope for energy and angular momentum both tend to values below 1. This suggests that orbits with a high magnitude of E or L are preferentially pushed to lower magnitudes than those with lower magnitudes. Figure 2.27 shows the fit slope value plotted against the change in mass between subsequent snapshots. In both cases, there is little correlation between these variables. This suggests that the mechanics that change the slope require more information about the host to model accurately. If this is the case, I cannot simply model this by a change in the mass of the system. One consideration is that the events that cause the slope to deviate from 1 may have long-lasting effects on the host system. This would mean that taking only information from the previous snapshot is insufficient to model this properly. One method to address this is to plot the slope against the dynamical state of the host. This should capture any relation to dynamically unrelaxed states of the host. Figure 2.27 clearly shows that for a low dynamical state, there is a significant deviation from the expected slope.

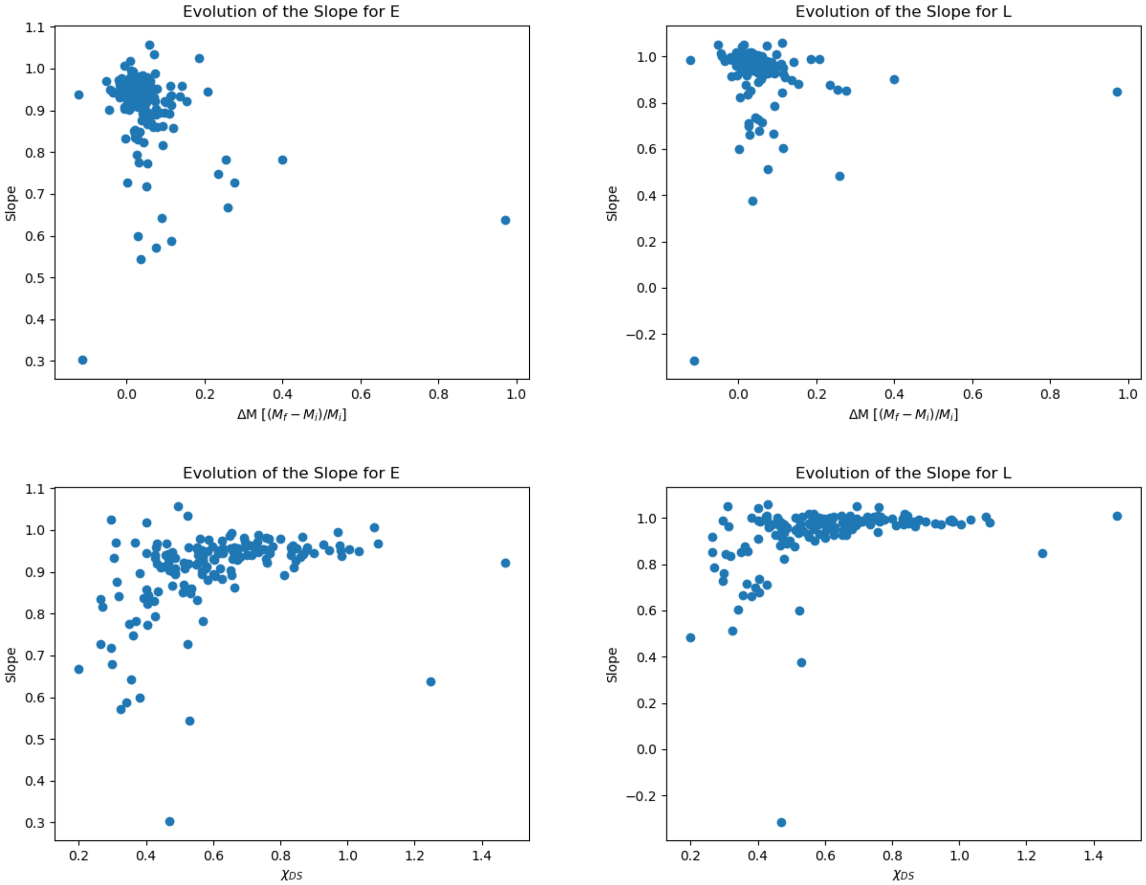

Figure 2.27: Same as Figure 2.26, but for the fit slope.

2.4.3.3 Determining the Scatter

The interpretation of increased scatter is the simplest of the three fitting parameters. It indicates an increased random deviation to the expected final orbital parameter. This would describe the tendency for orbits to be unpredictably kicked away from their original orbit. Thus, it is expected that an increase in orbital scatter, both in E and L will occur during times of low dynamical state. This is shown clearly in the Figure 2.28. For both E and L, we see an apparent increase in the scatter as the dynamical state parameter decreases.

It is tempting to instead model this by the change in mass between snapshots. Large mass changes should also indicate periods of turbulent growth, which is the property of also tracked with dynamical state. However, as seen in Figure 2.28, there seems to be little correlation between these values. One reason this fails to capture the desired effect is that mergers act over long periods of time. Thus, there is not enough information gained by examining the changes in host mass. Plotting the relationship between several snapshots in the past also does not give meaningful results. See the appendix for these plots and a few other parameters that fail to capture these effects.

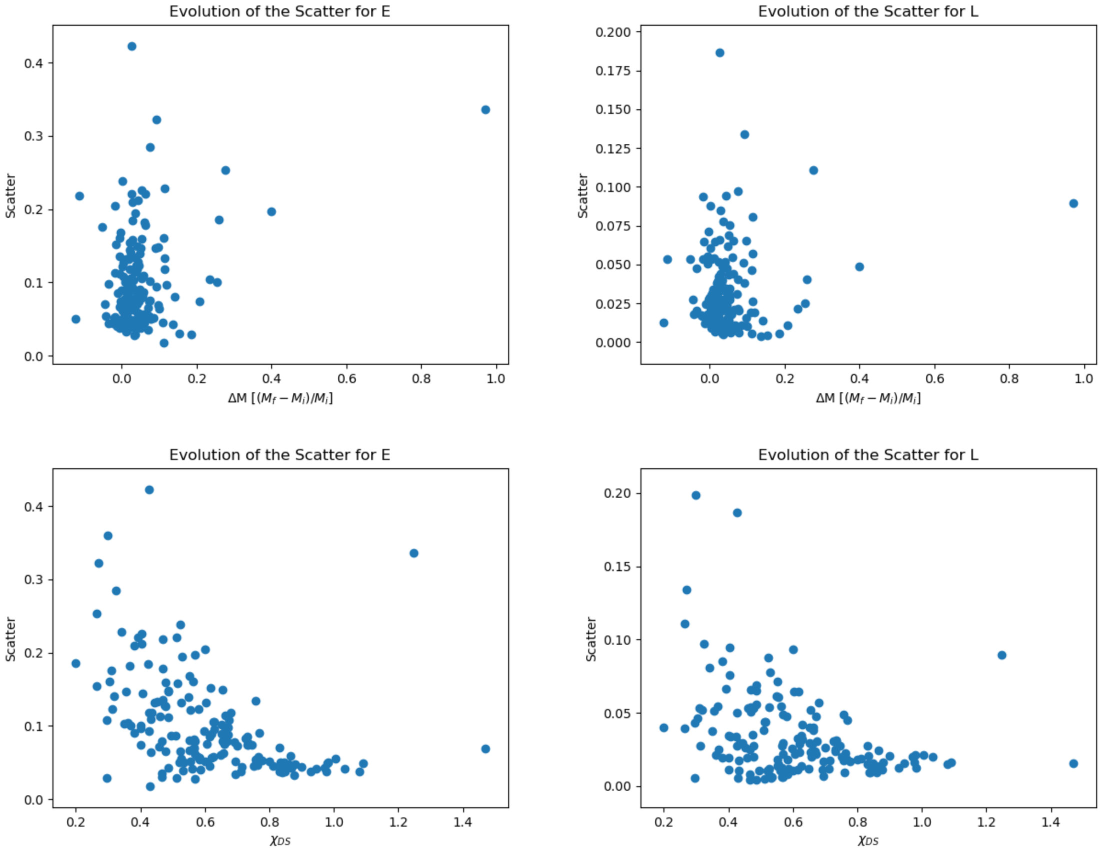

Figure 2.28: Same as Figure 2.26, but for the fit scatter.

Chapter 3

Summary and Conclusions

Through the analysis of three high-resolution zoom-in simulations of galaxy clusters, I examined the nature of subhalo orbits. In 2.2, I examined the properties at the time of initial infall. Although the mass ratio has a weak relationship with infall parameters, individual halos, redshift, and host mass do not show any clear trend in total or radial velocity. This suggests that the specific state of the host has a large effect on the predicted infall parameters. It is found that infall parameters depend slightly on the location of the merger. If the host is modeled with an ellipsoid, orbits that merge along its largest axis merge with a slightly larger, less radial velocity.

In 2.3, I examine whether these parameters can predict pericentric passage in timing and radii. The triaxial nature of the host, interactions with other subhalos, and the dynamical state of the host are expected to cause orbital parameters to change. I find that most orbits fall within 25% of their expected pericentric passage. The fraction of merging systems that do not fall within this criteria increases during periods in which the host is not relaxed. This can be as high as 70%, but hovers around 30% during dynamically relaxed epochs of the host's evolution. This indicates that dynamic instability greatly impacts subhalo orbits, particularly the predictions for pericentre at the initial merger time.

Lastly, in 2.4, I examine the evolution of the population of orbital properties of subhalos. I find that periods of low dynamical state act to change the system as a whole drastically. This is seen by increased orbital scatter during these times. Although the evolution between subsequent snapshots appears to follow a linear relation, with the scattering term, I cannot accurately generate a model for this evolution. The reason for this is argued to be that to model the process that causes this disruption requires intimate knowledge of the properties of the host, such as their dynamical state.

These results all point towards a similar picture: Subhalo orbits are tied heavily to the state of their host. For individual hosts, infall parameters do not follow their expected trends, and these parameters may change during specific periods of the evolution of the host. Orbits will also often become kicked during their first orbit, which is tied to the dynamical state of the host. Also, modeling the evolution of orbits is only accurate for short periods with detailed information about the host. Thus, a detailed SAM of subhalo orbits is not feasible based solely on the MAH of the host. These properties require specific information about the state of the host, which is inaccessible from the MAH alone. The heating and sudden change in the potential of the hose caused by major mergers and close interactions between subhalos are key aspects not well modeled through the MAH alone.

For quenching models, predicting pericenter should include the contribution of other subhalos and the complex nature of major mergers. These should also be relevant when predicting the evolution of subhalo orbits. Since dynamical state should probe these aspects of the host system, a model for these processes should aim to use a probe of the dynamical state instead of the MAH alone. Moving forward, this analysis should be conducted on a larger population of host systems to probe the ranges of dynamical states more accurately. With more analysis, it may be feasible to generate a method to model the evolution of orbital properties between subsequent snapshots properly. This method should use all available information, such as the entire MAH before the merger.

References

Abazajian, K. N., Adelman-McCarthy, J. K., Agüeros, M. A., et al. 2009, ApJS, 182, 543

Abdullah, M. H., Wilson, G., & Klypin, A. 2018, The Astrophysical Journal, 861, 22

Alves, J., Forveille, T., Pentericci, L., & Shore, S. 2020, Astronomy amp; Astrophysics, 641

Baldry, I. K., Balogh, M. L., Bower, R. G., et al. 2006, Monthly Notices of the Royal Astronomical Society, 373, 469–483

Baldry, I. K., Glazebrook, K., Brinkmann, J., et al. 2004, The Astrophysical Journal, 600, 681–694

Balogh, M. L., Navarro, J. F., & Morris, S. L. 2000, ApJ, 540, 113

Bartlett, J. G. 1997, in Astronomical Society of the Pacific Conference Series, Vol. 126, From Quantum Fluctuations to Cosmological Structures, ed. D. Valls-Gabaud, M. A. Hendry, P. Molaro, & K. Chamcham, 365

Begeman, K. G. 1989, A&A, 223, 47

Benson, A. J. 2005, MNRAS, 358, 551

Binney, J. & Tremaine, S. 2008, Galactic Dynamics (Princeton University)

Bovy, J. in prep., Dynamics and Astrophysics of Galaxies (Princeton University Press)

Buote, D. A. & Humphrey, P. J. 2012, in Astrophysics and Space Science Library, Vol. 378, Astrophysics and Space Science Library, ed. D.-W. Kim & S. Pellegrini, 235

Cui, W., Knebe, A., Yepes, G., et al. 2018, Monthly Notices of the Royal Astronomical Society, 480, 2898

Daod, N. A. & Zeki, M. K. 2019, The Astrophysical Journal, 870, 107

Davidzon, I., Ilbert, O., Laigle, C., et al. 2017, A&A, 605, A70

Davis, M., Efstathiou, G., Frenk, C. S., & White, S. D. 1985, The Astrophysical Journal, 292, 371

Deason, A. J., Fattahi, A., Frenk, C. S., et al. 2020, MNRAS, 496, 3929

Diaferio, A. 1999, Monthly Notices of the Royal Astronomical Society, 309, 610–622

Diaferio, A. & Geller, M. J. 1997, The Astrophysical Journal, 481, 633–643

Einasto, J. 1965, Trudy Astrofizicheskogo Instituta Alma-Ata, 5, 87

Genel, S., Bouché, N., Naab, T., Sternberg, A., & Genzel, R. 2010, ApJ, 719, 229

Gill, S. P. D., Knebe, A., Gibson, B. K., & Dopita, M. A. 2004, MNRAS, 351, 410

Haggar, R., Gray, M. E., Pearce, F. R., et al. 2020, MNRAS, 492, 6074

Hahn, O. & Abel, T. 2011, Monthly Notices of the Royal Astronomical Society, 415, 2101

Henriques, B. M., Yates, R. M., Fu, J., et al. 2019, Monthly Notices of the Royal Astronomical Society, 491, 5795–5814

Hubble, E. P. 1926, The Astrophysical Journal, 64, 321

Jiang, L., Cole, S., Sawala, T., & Frenk, C. S. 2015, Monthly Notices of the Royal Astronomical Society, 448, 1674

Kauffmann, G., Heckman, T. M., White, S. D., et al. 2003, Monthly Notices of the Royal Astronomical Society, 341, 54–69

Kauffmann, G., White, S. D., Heckman, T. M., et al. 2004, Monthly Notices of the Royal Astronomical Society, 353, 713–731

Kauffmann, G., White, S. D. M., Heckman, T. M., et al. 2004, MNRAS, 353, 713

Khochfar, S. & Burkert, A. 2006, A&A, 445, 403

Kim, J. & Park, C. 2006, The Astrophysical Journal, 639, 600

Knebe, A., Gill, S. P. D., Gibson, B. K., et al. 2004, ApJ, 603, 7

Knollmann, S. R. & Knebe, A. 2009, ApJS, 182, 608

Lacey, C. & Cole, S. 1993, Monthly Notices of the Royal Astronomical Society, 262, 627–649

Lacey, C. G., Baugh, C. M., Frenk, C. S., et al. 2016, Monthly Notices of the Royal Astronomical Society, 462, 3854–3911

Laigle, C., McCracken, H. J., Ilbert, O., et al. 2016, ApJS, 224, 24

Lewis, A., Challinor, A., & Lasenby, A. 2000, ApJ, 538, 473

Lotz, J. M., Davis, M., Faber, S. M., et al. 2008, ApJ, 672, 177

Lotz, M., Remus, R.-S., Dolag, K., Biviano, A., & Burkert, A. 2019, MNRAS, 488, 5370

Madau, P. & Dickinson, M. 2014a, ARA&A, 52, 415

Madau, P. & Dickinson, M. 2014b, ARA&A, 52, 415

Navarro, J. F., Frenk, C. S., & White, S. D. 1997, The Astrophysical Journal, 490, 493–508

Ogiya, G., van den Bosch, F. C., & Burkert, A. 2022, MNRAS, 510, 2724

Oman, K. A., Hudson, M. J., & Behroozi, P. S. 2013, Monthly Notices of the Royal Astronomical Society, 431, 2307

Oñorbe, J., Garrison-Kimmel, S., Maller, A. H., et al. 2013, Monthly Notices of the Royal Astronomical Society, 437, 1894

Peng, Y.-j., Lilly, S. J., Kovač, K., et al. 2010, ApJ, 721, 193

Peng, Y.-j., Lilly, S. J., Renzini, A., & Carollo, M. 2012, The Astrophysical Journal, 757, 4

Pizzardo, M., Geller, M. J., Kenyon, S. J., Damjanov, I., & Diaferio, A. 2023, Astronomy and Astrophysics, 675

Planck Collaboration, Ade, P. A. R., Aghanim, N., et al. 2016, A&A, 594, A20

Powell, R. 2006, The Hertzsprung Russell Diagram

Press, W. H. & Schechter, P. 1974, The Astrophysical Journal, 187, 425

Russell, H. N. 1919, Proceedings of the National Academy of Sciences, 5, 391–416

Schindler, S. 2000, in IAU Joint Discussion, Vol. 24, IAU Joint Discussion, 10

Sellwood, J. & Masters, K. L. 2022, Annual Review of Astronomy and Astrophysics, 60, 73–120

Shaw, L. D., Weller, J., Ostriker, J. P., & Bode, P. 2006, ApJ, 646, 815

Smith, R., Calderón-Castillo, P., Shin, J., Raouf, M., & Ko, J. 2022, The Astronomical Journal, 164, 95

Somerville, R. S., Hopkins, P. F., Cox, T. J., Robertson, B. E., & Hernquist, L. 2008, MNRAS, 391, 481

Springel, V. 2005, Monthly Notices of the Royal Astronomical Society, 364, 1105

Stücker, J., Ogiya, G., Angulo, R. E., Aguirre-Santaella, A., & Sánchez-Conde, M. A. 2023, MNRAS, 521, 4432

Taylor, J. E. 2011, Advances in Astronomy, 2011, 1–17

Taylor, J. E., Shin, J., Ouellette, N. N.-Q., & Courteau, S. 2019, Monthly Notices of the Royal Astronomical Society, 488, 1111

Tormen, G. 1997, MNRAS, 290, 411

van den Bosch, F. C. 2017, MNRAS, 468, 885

van den Bosch, F. C., Ogiya, G., Hahn, O., & Burkert, A. 2018, MNRAS, 474, 3043

Vitvitska, M., Klypin, A. A., Kravtsov, A. V., et al. 2002, ApJ, 581, 799

Wang, H. Y., Jing, Y. P., Mao, S., & Kang, X. 2005, Monthly Notices of the Royal Astronomical Society, 364, 424

Wetzel, A. R. 2011, MNRAS, 412, 49

White, S. D. & Rees, M. J. 1978, Monthly Notices of the Royal Astronomical Society, 183, 341–358

Woosley, S. E. & Weaver, T. A. 1995, ApJS, 101, 181

Zel'dovich, Y. B. 1970, A&A, 5, 84

APPENDICES

Appendix A

Supplemental Derivations and Plots

A.1 Triaxial Potential

Assuming an ellipsoidal mass density leads to a more complicated potential. This comes from the extension of the spherical collapse model, where initial perturbations in the density field are no longer assumed to be spherical, but ellipsoidal. In this more realistic case, the NFW density is no longer a function of radial position but by a new quantity m^2:

$$\begin{aligned} \rho(m^2) &= \frac{\rho_0 R_s^3}{\sqrt{m^2}(R_s + \sqrt{m^2})^2} \\ \text{where } m^2 = r'^2 &= a'^2 \left(\frac{x^2}{a'^2} + \frac{y^2}{b'^2} + \frac{z^2}{c^2} \right) \\ \text{and } M^2 &= a'^2 \left(\frac{x^2}{a'^2 + \tau} + \frac{y^2}{b'^2 + \tau} + \frac{z^2}{c^2 + \tau} \right) . \end{aligned}$$

a'^2, b'^2, and c'^2 are the lengths of the ellipsoid's largest, middle, and smallest axis that describes the profile's shape. The potential has no general analytic form, but it can be numerically integrated. This is done with a quantity $f(m) = \int_0^{m^2} dm^2 \rho(m^2)$, which describes the mass interior to a surface of constant density defined by m^2.

Solving for $f(m)$ is shown below.

$$\begin{aligned}
f(m) &= \int_0^{m^2} dm'^2 \rho(m'^2) \\
&= \int_0^{m^2} dm'^2 \frac{\rho_0 R_s^3}{\sqrt{m'^2}(R_s + \sqrt{m'^2})^2} \\
&= \frac{2\rho_0 R_s^3 m}{R_s(m + R_s)} \\
&= \frac{2\rho_0 R_s^2 m}{m + R_s}. \\
\text{Note that } f(\infty) &= \lim_{m \to \infty} \frac{2\rho_0 R_s^2}{1 + R_s/m} \\
&= 2\rho_0 R_s^2
\end{aligned}$$

The potential from this can then be solved using f(M) instead of f(m):

$$\begin{aligned}
\phi(x,y,z) &= -\pi G \frac{b'c'}{a'} \int_0^\infty d\tau \frac{f(\infty) - f(M)}{\sqrt{(\tau + a'^2)(\tau + b'^2)(\tau + c'^2)}} \\
&= -\pi G \frac{b'c'}{a'} \int_0^\infty d\tau \frac{2\rho_0 R_s^2 - \frac{2\rho_0 R_s^2 M}{M + R_s}}{\sqrt{(\tau + a'^2)(\tau + b'^2)(\tau + c'^2)}} \\
&= -\pi G \frac{2b'c'\rho_0 R_s^2}{a'} \int_0^\infty d\tau \frac{1 - \frac{M}{M + R_s}}{\sqrt{(\tau + a'^2)(\tau + b'^2)(\tau + c'^2)}}
\end{aligned}$$

Numerically solving this is much easier with a change of variables. Following Buote & Humphrey (2012), such a change is chosen to be:

$$\begin{aligned}
s &= \frac{1}{\sqrt{1 + \tau}} \\
ds &= -\frac{1}{2} s^3 d\tau \\
\rightarrow \tau &= s^{-2} - 1
\end{aligned}$$

Changing the bounds accordingly, the integral describing the potential becomes:

$$\phi(x,y,z) = -\pi G \frac{4b'c'\rho_0 R_s^2}{a'} \int_0^1 ds \frac{1-\frac{m}{m+R_s}}{s^3\sqrt{(s^{-2}-1+a'^2)(s^{-2}-1+b'^2)(s^{-2}-1+c'^2)}}$$

A triaxial NFW potential can alternatively describe the potential. To do this, the spherical NFW-potential is modified in the same way as the spherical, $r \rightarrow \sqrt{x'^2 + y`^2/b^2 + z`^2/c^2}$. This is computationally more simple, as the analytical form of the potential is readily available. However, the corresponding mass distribution is not physically motivated.

A.2 Maximum Circularity

Figure 2.11 shows a clear boundary in phase space corresponding to these bound orbits. At the virial radius, bound orbits have a total specific energy between 0 and $\Phi(R_{\mathrm{vir}})$. Thus, given an initial specific energy E_0 in this range, the specific kinetic energy is given as:

$$K = E_0 - \Phi(R_{\mathrm{vir}})\,.$$

Similarly, the velocity is given as:

$$\frac{\sqrt{V_{\mathrm{tan}}^2 + V_{\mathrm{rad}}^2}}{2} = E_0 - \Phi(R_{\mathrm{vir}}) \tag{A.1}$$

$$V_{\mathrm{tan}} = \sqrt{4(E_0 - \Phi(R_{\mathrm{vir}}))^2 - V_{\mathrm{rad}}^2} \tag{A.2}$$

$$V_{\mathrm{tan}} = \sqrt{4K^2 - V_{\mathrm{rad}}^2} \tag{A.3}$$

The equation for circularity is given as:

$$c = \frac{L_0}{L_{\mathrm{circ}}}\,, \tag{A.4}$$

Where L_{circ} is given as the angular momentum of a circular orbit with the same energy, and L_0 is the initial angular momentum. This can also apply to an orbit's specific angular momentum.

Note that L_{circ} only depends on the orbit's initial energy. This means the maximum angular momentum of a bound orbit dictates the maximum circularity. Thus, in the context of initial energy, the following equation is obtained:

$$c_{\mathrm{max}}(E_0) = \frac{R_{\mathrm{vir}} V_0 \sin\theta}{L_{\mathrm{circ}}(E_0)} = \frac{R_{\mathrm{vir}} V_{\mathrm{tan,max}}}{L_{\mathrm{circ}}(E_0)} \tag{A.5}$$

From equation A.3, $V_{\mathrm{tan,max}}$ occurs when $V_{\mathrm{rad}} = 0$, meaning the orbit is circular. In this case, $V_{\mathrm{tan}} = V_{\mathrm{tot}}$, and $V_{\mathrm{tot}} = \sqrt{2(E_0 - \Phi(R_{\mathrm{vir}}))}$. Thus, c_{max} is a function of only the initial energy and parameters of the host system:

$$c_{\mathrm{max}}(E_0) = \frac{R_{\mathrm{vir}}\sqrt{2(E_0 - \Phi(R_{\mathrm{vir}}))}}{L_{\mathrm{circ}}(E_0)} \tag{A.6}$$

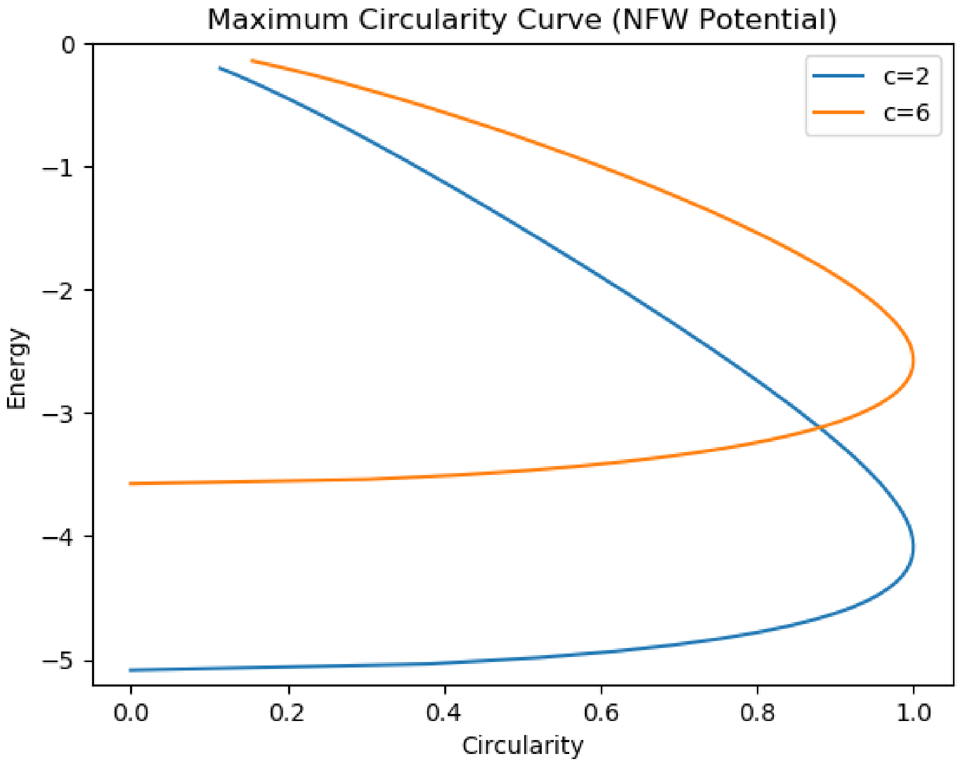

Figure A.1: Boundary for Energy vs. Circularity Diagram. Energy is scaled to the virial energy of the host system. This was generated using equation A.5 for two different NFW potentials, with $c_{\rm NFW} = 2$ and 6. This shows the dependence of the shape on the potential of the system.

A.3 Kicked Fraction for All Hosts

Here are the same plots as in Figure 2.17for all three host halos. Across all of them, the kicked fraction increases during low dynamical state.

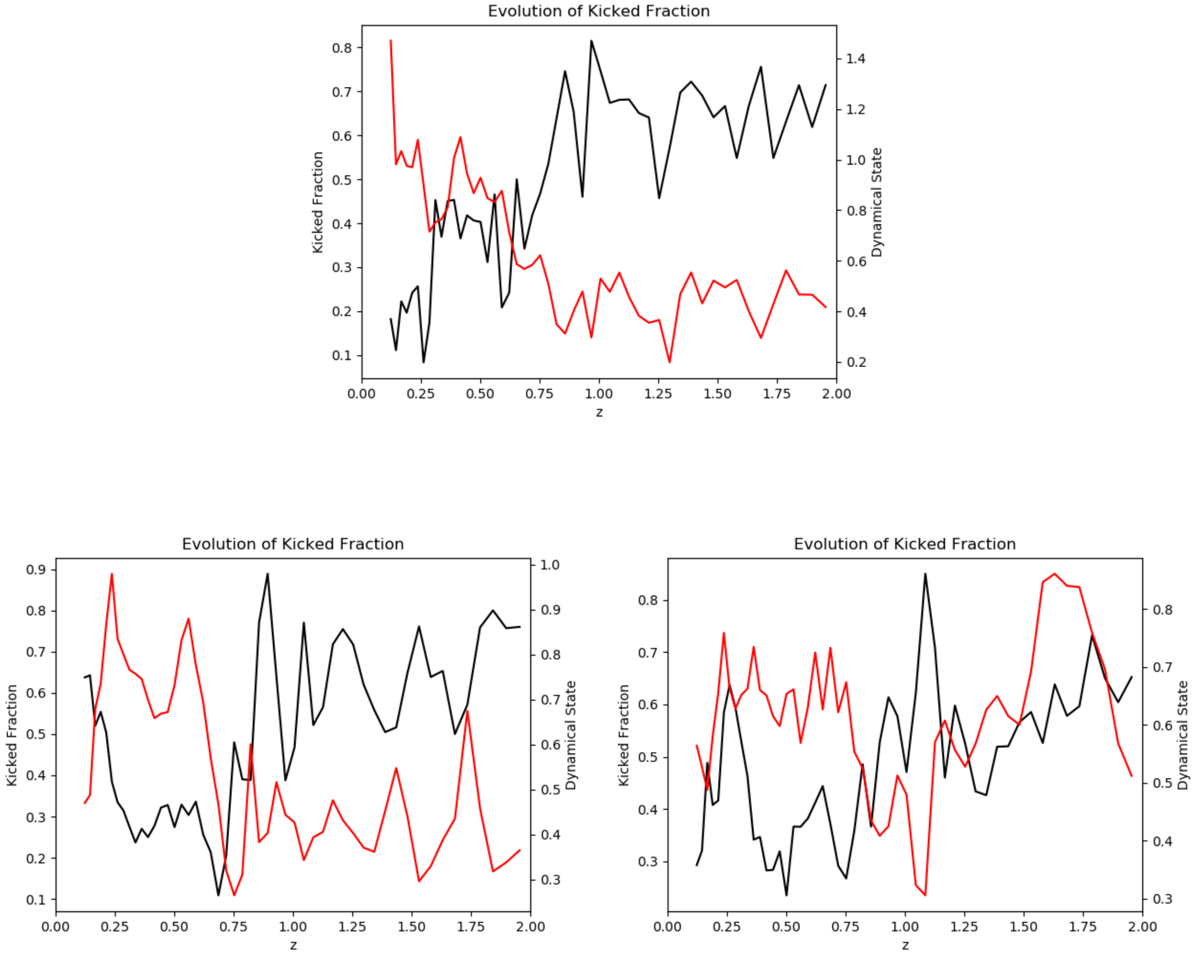

Figure A.2: The evolution of the kicked fraction and dynamical state vs. redshift for all three host halos are shown above.

A.4 Model Results for All Hosts

Below are the model results for all three hosts. They all follow similar results as presented in 2.4.

A.4.1 Host 1

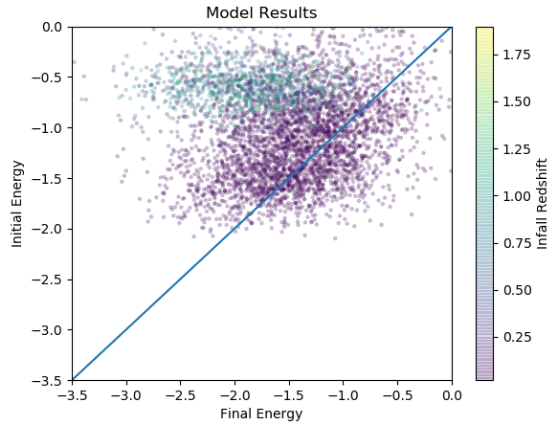
Model Results

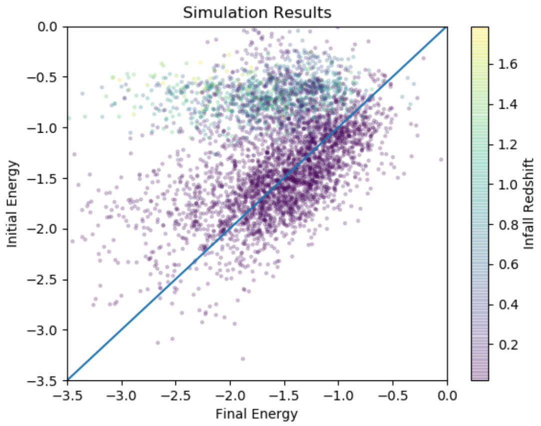
Simulation Results

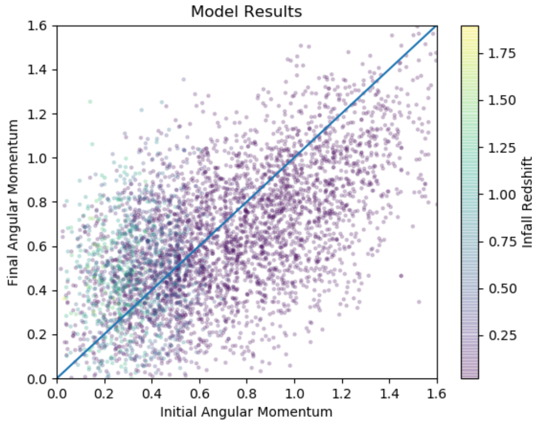
Model Results

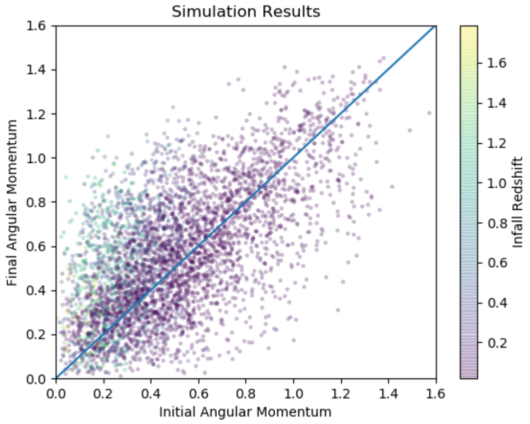
Simulation Results

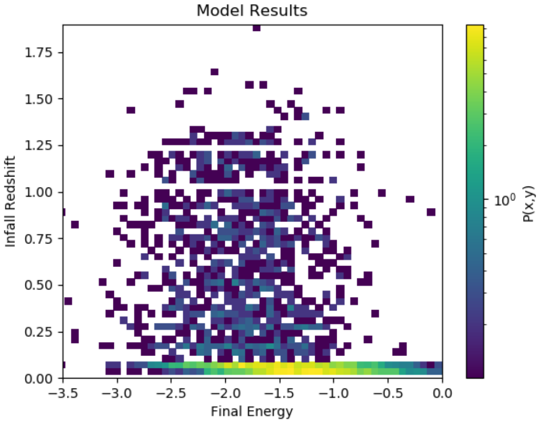
Model Results
Infall Redshift
0.00
0.25
0.50
0.75
1.00
1.25
1.50
1.75
−3.5
−3.0
−2.5
−2.0
−1.5
−1.0
−0.5
0.0
Final Energy
10^0
P(x,y)

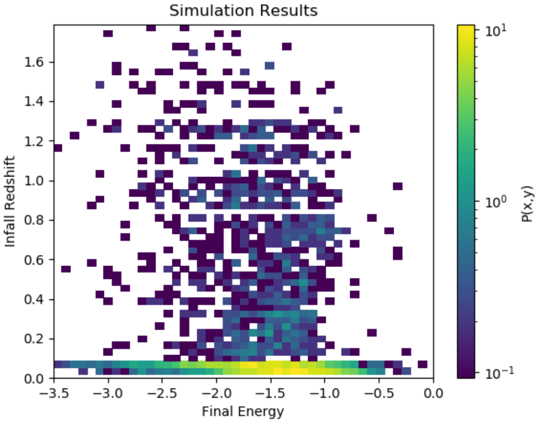
Simulation Results
Infall Redshift
0.0
0.2
0.4
0.6
0.8
1.0
1.2
1.4
1.6
−3.5
−3.0
−2.5
−2.0
−1.5
−1.0
−0.5
0.0
Final Energy
10^1
10^0
10^{-1}
P(x,y)

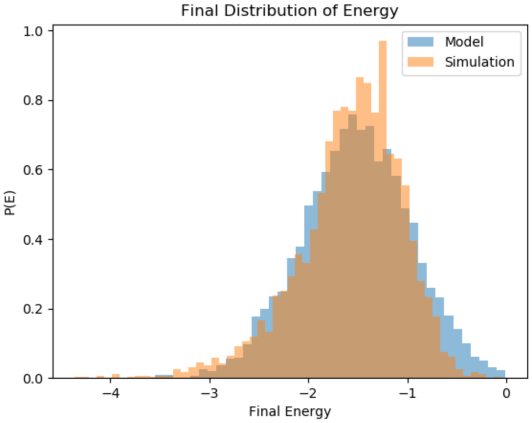
Final Distribution of Energy
Model
Simulation
P(E)
0.0
0.2
0.4
0.6
0.8
1.0
−4
−3
−2
−1
0
Final Energy

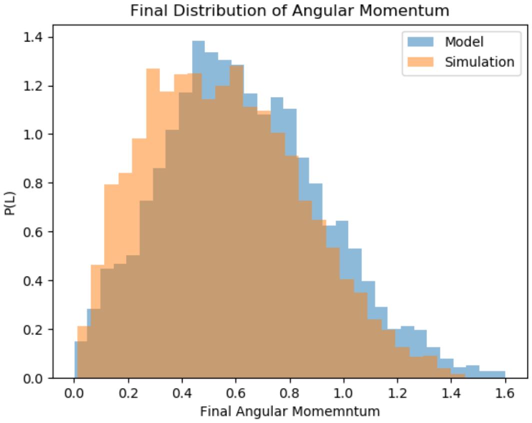
Final Distribution of Angular Momentum
Model
Simulation
P(L)
0.0
0.2
0.4
0.6
0.8
1.0
1.2
1.4
0.0
0.2
0.4
0.6
0.8
1.0
1.2
1.4
1.6
Final Angular Momemntum

A.4.2 Host 2

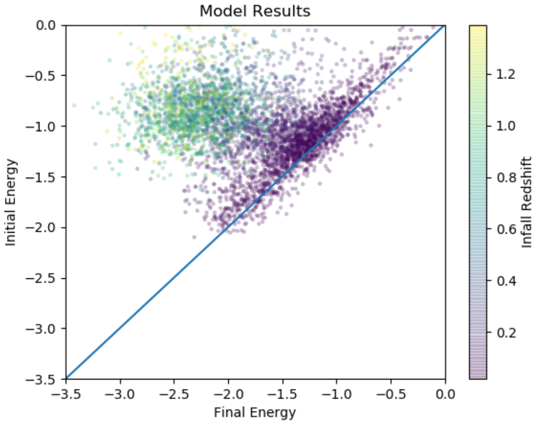
Model Results

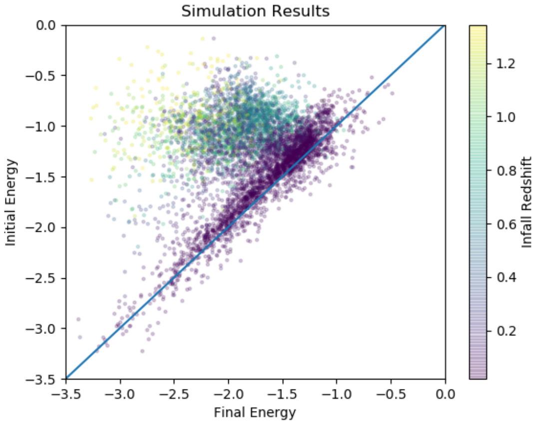
Simulation Results

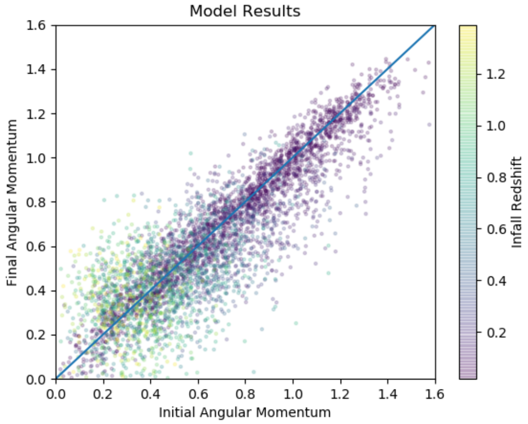
Model Results

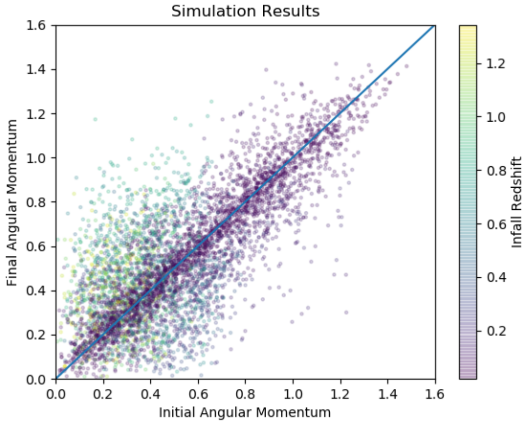
Simulation Results

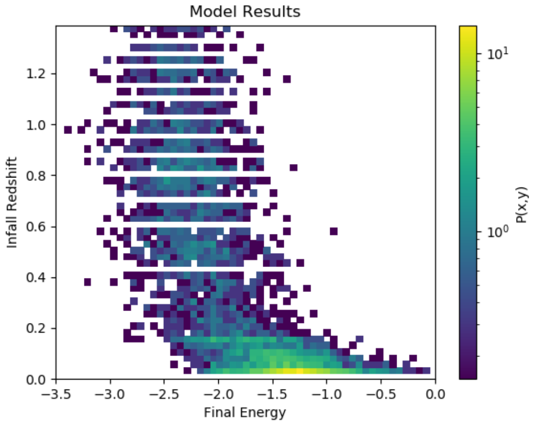
Model Results
Infall Redshift
0.0
0.2
0.4
0.6
0.8
1.0
1.2
−3.5
−3.0
−2.5
−2.0
−1.5
−1.0
−0.5
0.0
Final Energy
10^1
10^0
P(x,y)

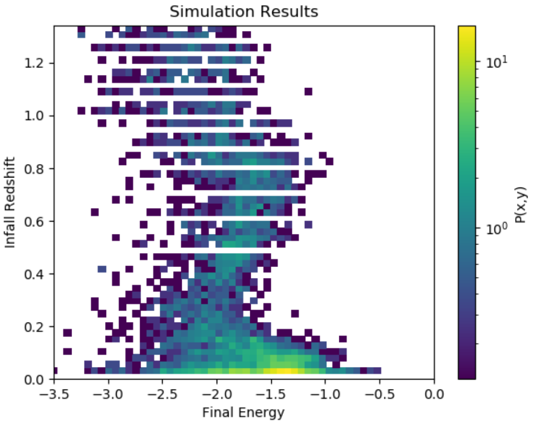
Simulation Results
Infall Redshift
0.0
0.2
0.4
0.6
0.8
1.0
1.2
−3.5
−3.0
−2.5
−2.0
−1.5
−1.0
−0.5
0.0
Final Energy
10^1
10^0
P(x,y)

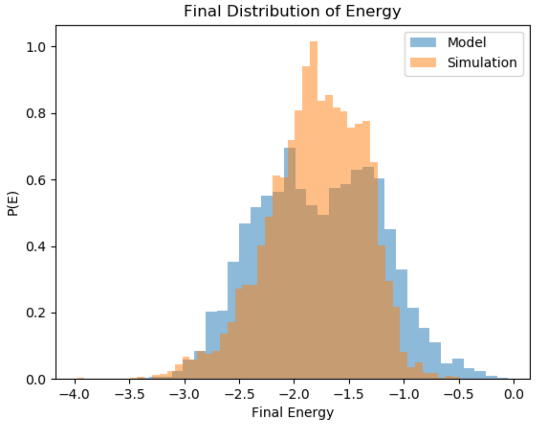
Final Distribution of Energy
Model
Simulation
P(E)
0.0
0.2
0.4
0.6
0.8
1.0
−4.0
−3.5
−3.0
−2.5
−2.0
−1.5
−1.0
−0.5
0.0
Final Energy

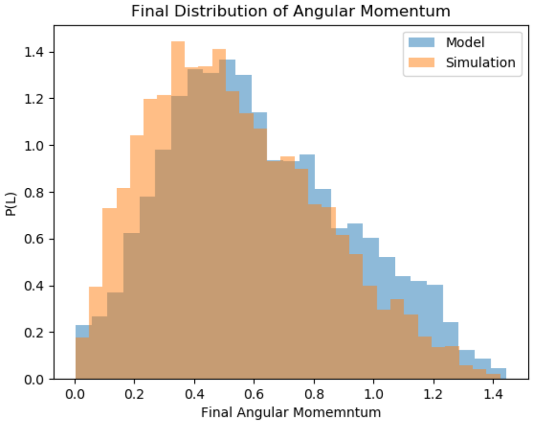
Final Distribution of Angular Momentum
Model
Simulation
P(L)
0.0
0.2
0.4
0.6
0.8
1.0
1.2
1.4
0.0
0.2
0.4
0.6
0.8
1.0
1.2
1.4
Final Angular Momemntum

A.4.3 Host 3

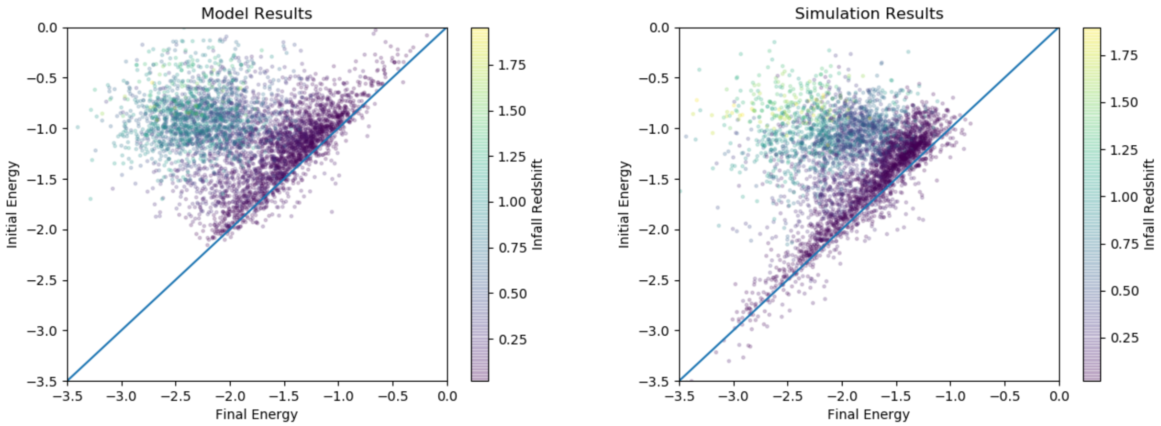
Model Results
Initial Energy
Final Energy
Infall Redshift
0.0
−0.5
−1.0
−1.5
−2.0
−2.5
−3.0
−3.5
1.75
1.50
1.25
1.00
0.75
0.50
0.25
Simulation Results
Initial Energy
Final Energy
Infall Redshift

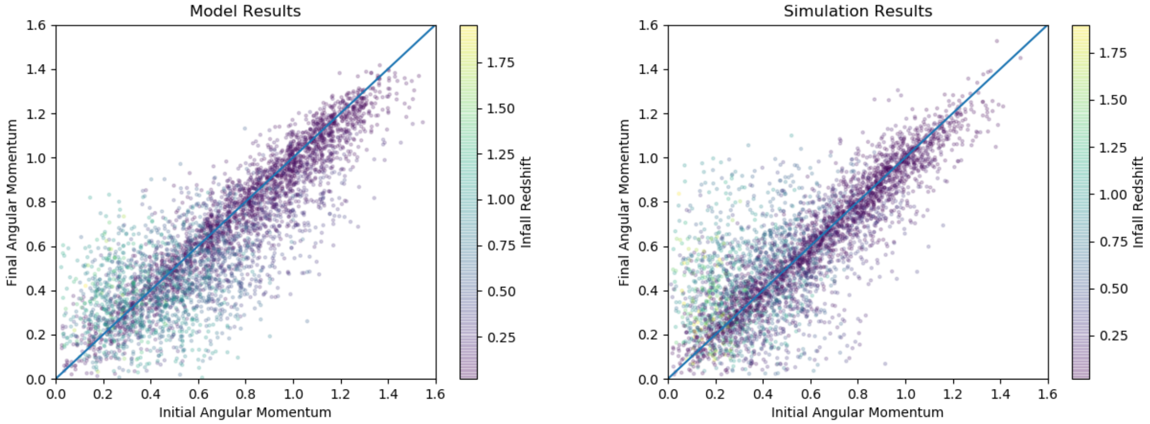
Model Results
Final Angular Momentum
Initial Angular Momentum
Infall Redshift
0.0
0.2
0.4
0.6
0.8
1.0
1.2
1.4
1.6
1.75
1.50
1.25
1.00
0.75
0.50
0.25
Simulation Results
Final Angular Momentum
Initial Angular Momentum
Infall Redshift

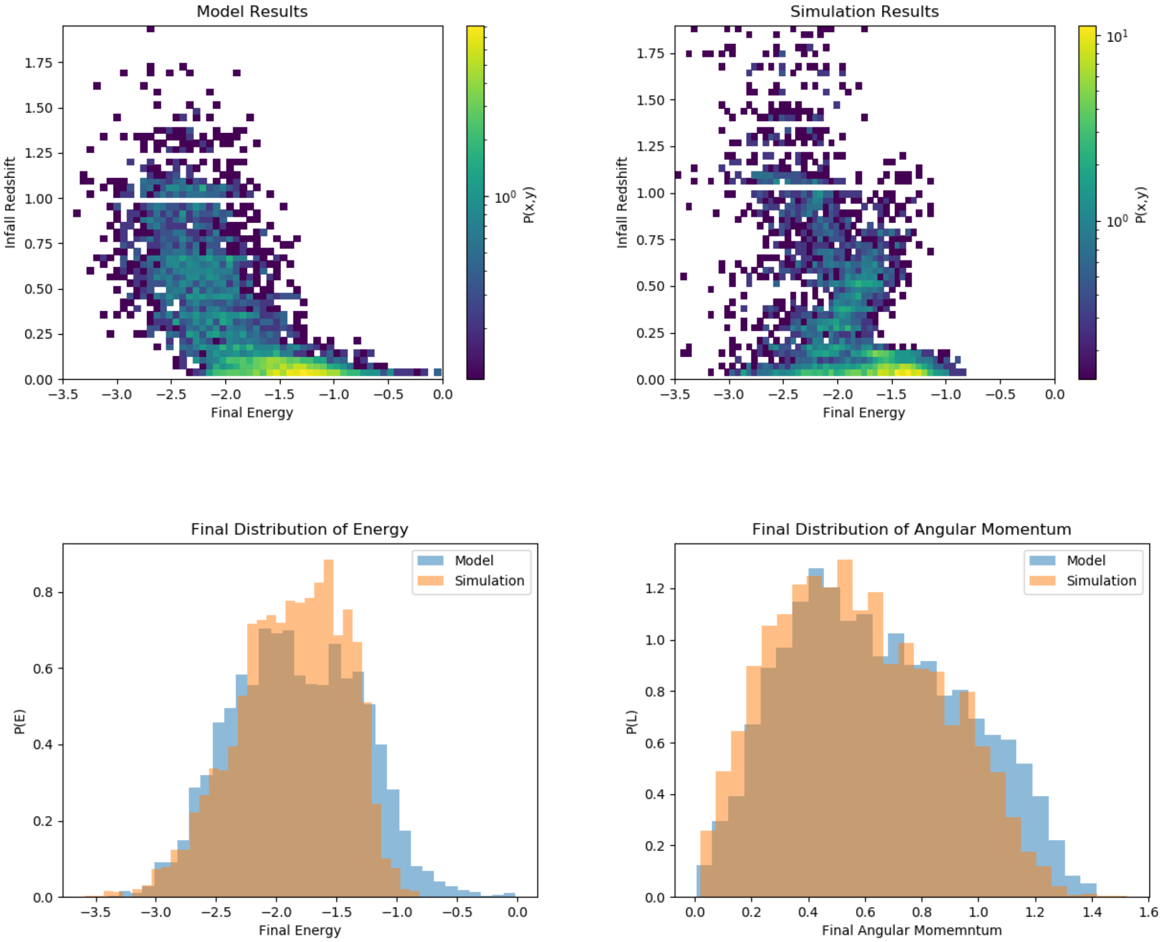

Figure A.3: Same as for Figures 2.25 and 2.24 for all hosts.